UNIVERSIDADE FEDERAL DO RIO GRANDE DO SUL
INSTITUTO DE PESQUISAS HIDRÁULICAS
PROGRAMA DE PÓS-GRADUAÇÃO EM RECURSOS HÍDRICOS E SANEAMENTO AMBIENTAL

Matheus Henrique Tavares

Estimativas da temperatura superficial da água por sensores remotos: acurácia e aplicabilidade com modelos de temperatura

Porto Alegre
2019

Matheus Henrique Tavares

Estimativas da temperatura superficial da água por sensores remotos: acurácia e aplicabilidade com modelos de temperatura

Dissertação apresentada ao Programa de Pós-Graduação em Recursos Hídricos e Saneamento Ambiental da Universidade Federal do Rio Grande do Sul, como requesito parcial à obtenção do grau de Mestre.

Orientador: David da Motta Marques
Coorientador: Carlos Ruberto Fragoso Jr.

Porto Alegre

2019

CIP - Catalogação na Publicação

Tavares, Matheus Henrique
Estimativas da temperatura superficial da água por sensores remotos: acurácia e aplicabilidade com modelos de temperatura / Matheus Henrique Tavares. -- 2019.
102 f.
Orientador: David Manuel Lelinho da Motta Marques.

Coorientador: Carlos Ruberto Fragoso Jr..

Dissertação (Mestrado) -- Universidade Federal do Rio Grande do Sul, Instituto de Pesquisas Hidráulicas, Programa de Pós-Graduação em Recursos Hídricos e Saneamento Ambiental, Porto Alegre, BR-RS, 2019.

1. temperatura superficial da água. 2. sensoriamento remoto. 3. modelagem da temperatura de rios. 4. Landsat. 5. MODIS. I. Motta Marques, David Manuel Lelinho da, orient. II. Fragoso Jr., Carlos Ruberto, coorient. III. Título.

Elaborada pelo Sistema de Geração Automática de Ficha Catalográfica da UFRGS com os dados fornecidos pelo(a) autor(a).

Matheus Henrique Tavares

Estimativas da temperatura superficial da água por sensores remotos: acurácia e aplicabilidade com modelos de temperatura

Dissertação apresentada ao Programa de Pós-Graduação em Recursos Hídricos e Saneamento Ambiental da Universidade Federal do Rio Grande do Sul, como requesito parcial à obtenção do grau de Mestre.

Trabalho aprovado. Porto Alegre, 8 de março de 2019:

Prof. Dr. David da Motta Marques– UFRGS
Orientador

Prof. Dr. Carlos Ruberto Fragoso Jr.– UFAL
Co-orientador

Prof. Dr. Anderson Luís Ruhoff – UFRGS
Examinador

Prof. Dra. Marie-Paule Bonnet – IRD
Examinadora

Prof. Dr. Humberto Ribeiro da Rocha – USP
Examinador

Agradecimentos

Primeiramente gostaria de agradecer à CAPES pelo financiamento deste estudo por meio da bolsa de estudos e auxílios, e À UFRGS e ao IPH pela ótima infraestrutura e incentivo à pesquisa dos alunos, e também pelo auxílio pelo PROEX.

Agradeço ao professor David pelo incrível entusiasmo pela pesquisa científica, por sempre querer transmitir o seu conhecimento (nos mais diversos assuntos), e por ser um verdadeiro "pai" como orientador. Ao professor Ruberto pela co-orientação, pela disponibilidade e auxílio em todas as etapas do mestrado, e pela recepção durante os períodos em Maceió. Agradeço também a outros professores do IPH que foram importantíssimos tanto na minha formação quanto para o desenvolvimento deste trabalho: Anderson Ruhoff, Rodrigo Paiva, Fernando Fan, Lucia, Beatriz, Juan Martín, Nilza, Walter e Masato. Além destes, agradeço também aos professores Marie Bonnet e Humberto Rocha pela avaliação e contribuições na banca.

Agradeço a meus pais, por estarem sempre presentes, pelo suporte e pelo incentivo desde sempre aos estudos. Ao meu irmão Marcos, por ser essa pessoa incrível e também sempre se fazer presente na minha vida (e por ter revisado meu texto). À Marianna, minha melhor amiga, pelo suporte e companhia de longa data, em todos os momentos (e por também ter revisado meu texto). Ao Lupe, por também ser essa pessoa incrível e trazer muita luz à Curitiba. À Isa e ao Allan, pelos almoços de domingo e risadas. Agradeço também aos demais amigos curitibanos: Beth, Gui, Gus, Luís, Brian, Kelvin, Vane, Kat, Lary, Felipe, Klismam, Orides e Pedro.

De Porto Alegre (e de Maceió), tenho que agradecer a dois grandes companheiros nesses dois anos de mestrado: Cléber e Hugo. Ao Hugo, que tem sido um grande parceiro, tanto na pesquisa quanto na vida. E ao Binho por ser um excelente amigo, pelas risadas, e principalmente pela façanha de ter me aturado quase todos os dias durante esses dois anos. Agradeço muito a companhia desses dois nordestinos. Agradeço também aos amigos de

POA que contribuíram com muitas conversas e risadas: Bruna, Felipe, Bárbara, Marília, Kaju, Huguinho, Thiago, João, Dani, Benício, Sly, Gui, Heron, Léo, Fran Vanelli, Fran Zanandrea, Ju, Erik, Itza, Gláucia, Rafa, Aline e Ayan. E de Maceió, também não poderia deixar de agradecer aos pais do Hugo, Augusto e Célia, e à mãe do Cléber, Alania, pela hospitalidade, e também aos amigos que fiz por lá: Jessica, Jackie, David, Angelo, Lu, Amanda, Mari, Válter, Deca, Eduardo e Jhon.

Por último, gostaria de agradecer a vários artistas que me ajudaram de muitas formas no processo de desenvolvimento deste trabalho, mas principalmente à Victoria Legrand e Alex Scally pela música inspiradora.

Resumo

Esta dissertação avaliou a acurácia de estimativas da temperatura superficial da água (TSA) de rios e lagos utilizando dois sensores remotos, e a aplicabilidade de modelos de temperatura da água de rios em conjunto com estes dados. O trabalho foi dividido em dois capítulos principais, o primeiro focando em lagos e o segundo em rios. No Capítulo 2 foi estudada a acurácia da estimativa da temperatura superficial da Lagoa Mangueira utilizando os sensores Landsat 7 ETM+, este com aplicação de diferentes métodos, e MODIS, utilizando seus produtos MOD11 e MOD28. Verificou-se que o MOD11 e a aplicação da equação de transferência radiativa (RTE) com as imagens Landsat se mostraram as melhores opções, com REQM próximos a 1°C. Também foi verificado que esta equação é bastante sensível aos parâmetros de entrada, mas que os parâmetros de correção obtidos pelo AtmCorr são consistentes, apesar da perda de desempenho quando há alta quantidade de vapor d'água na atmosfera. Além disso, foi analisada a sensibilidade da acurácia a duas variáveis, a emissividade e os parâmetros atmosféricos, e verificados os impactos dos efeitos de superfície nas estimativas da TSA, em especial o efeito de pele fria, que resulta em uma subestimatação média da temperatura, observado na maior parte dos trabalhos neste tema. No Capítulo 3 foi analisada a consistência de séries contínuas da temperatura de um rio geradas por dois modelos de temperatura de rios, o *air2stream* e um modelo estocástico, calibrados com dados derivados dos sensores Landsat 7 ETM+ e MODIS, este após o uso de uma técnica de *downscale*. Verificou-se que é possível gerar séries contínuas e consistentes da temperatura de rios utilizando o modelo *air2stream* calibrado com estes dados. Contudo, esta aplicação está atrelada à acurácia da estimativa da TSA pelo Landsat 7 ETM+, que é inferior à estimativa em lagos, principalmente devido ao tamanho dos pixels e o efeito do entorno do rio na radiância captada pelo sensor devido à reflexão da água. Nesta estimativa, novamente a aplicação da RTE com AtmCorr se mostrou a melhor opção, com REQM próximo a 1,4°C. O desempenho da técnica de fusão de imagens foi bastante fraco, e os critérios de seleção desenvolvidos se mostraram cruciais para uma incorporação apenas dos dados mais acurados. Em virtude deste baixo desempenho, o uso das imagens MODIS junto com as Landsat mostrou pouca resposta pelo modelo, apesar de indicar que mais dados podem melhorar sua performance. Ainda assim, o modelo mostrou um boa performance utilizando apenas os dados do Landsat na sua calibração, e esta abordagem tem grande potencial para ser aplicada em rios sem dados medidos de temperatura, como em análise de tendências das séries temporais da temperatura e na modelagem de rios tributários para aplicação em modelos ecológicos de lagos.

Palavras-chaves: Temperatura superficial da água; sensoriamento remoto; lagos; rios; Landsat; MODIS; modelagem da temperatura de rios; infravermelho termal; downscaling.

Abstract

This dissertation assessed the accuracy of estimates of rivers and lakes water surface temperature (WST) using two remote sensors, and the applicability of river water temperature models with these data. This work was divided in two chapters, the first focusing on lakes and the second on ivers. In Chapter 2 the accuracy of the surface temperature estimates was assessed in Lake Mangueira, using Landsat 7 ETM+, by applying different methods, and MODIS, using its products MOD11 and MOD28. Both MOD11 and the application of the radiative transfer equation (RTE) with Landsat images showed the best results, with RMSE close to 1°C. It was also verified that this equation is very sensitive to its input parameters, but the correction parameters provided by AtmCorr are consistent, despite the loss of performance when there is the water vapour in the atmosphere is high. Furthermore, the its sensibility to two variables, the emissivity and the atmospheric parameters, and the impacts of the surface effects on the accuracy of the estimates were evaluated, in particular the cool-skin effect, which results in a mean underestimation of the temperature, and was observed in most studies in this subject. In Chapter 3 the consistency of continuous series of river temperatures generated by two river temperature models, *air2stream* and a stochastic model, and calibrated with data derived by Landsat 7 ETM+ and MODIS, in this case after the application of a downscaling technique, were analysed. It was observed that it is possible to generate continuous and consistent series of river temperature with *air2stream* calibrated with these data. However, this application is dependant on the accuracy of the WST estimates using Landsat, which is inferior in rivers when compared to lakes, mainly due to the pixel size and the effect of the surrounding surfaces on the radiance measured by the sensor due to the reflection by the water surface. In this case, again the the application of the RTE with AtmCorr showed the best results, with RMSE close to 1.4°C. The image fusion technique underperformed, and the data selection criteria were crucial for the incorporation of the accurate data only. Due to this weak performance, the use of MODIS images along with Landsat showed little response by the model, although there is indication that more data can improve its performance. Still, the model showed a good performance when calibrated with Landsat-derived data, and this approach has great potential for studies in rivers with no measured water temperature data, such as trend analysis of temperature and in modelling tributary rivers temperatures as input data for lake ecological modelling.

Key-words: Water surface temperature; remote sensing; lakes; rivers; Landsat; MODIS; river temperature modelling; thermal infrared; downscaling.

Lista de ilustrações

Lista de tabelas

Lista de abreviaturas e siglas

AtmCorr	*Atmospheric Correction Parameter Calculator* – plataforma online da NASA
CAPES	Coordenação de Aperfeiçoamento de Pessoal de Nível Superior
CNPq	Conselho Nacional de Desenvolvimento Cientifico e Tecnológico
ETM+	*Enhanced Thematic Mapper Plus*
LSWT	*Lake surface water temperature* – temperatura superficial da água do lago
LST	*Land surface temperature* – temperatura superficial continental
MODIS	*MODerate-Resolution Imaging Spectroradiometer*
NIR	*Near infrared* – infravermelho próximo
REQM	Raíz do erro quadrático médio
SADFAT	*Spatiotemporal Adaptative Data Fusion Algorithm for Temperature mapping*
SST	*Sea surface temperature* – temperatura superficial oceânica
ST	*Surface temperature* – temperatura da superfície
SWT	*Surface water temperature* – temperatura superficial da água
TIR	*Thermal infrared* – infravermelho termal
TM	*Thematic Mapper*
TSA	Temperatura superficial da água

Lista de símbolos

ε	Emissividade
λ	Comprimento de onda
L^{down}	Radiância emitida/refletida para baixo pela atmosfera (*downwelling radiance*)
L^{up}	Radiância emitida/refletida para cima pela atmosfera (*upwelling radiance*)
L_{sensor}	Radiância medida pelo sensor (*top of atmosphere radiance*)
L_{corr}	Radiância medida pelo sensor e corrigida dos efeitos atmosféricos
ψ_n	Funções atmosféricas do algoritmo de canal único
Q	Vazão
σ	Desvio-padrão
τ	Transmissividade da atmosfera
T_a	Temperatura do ar
T_w	Temperatura da água
T_{sensor}	Temperatura de brilho medida pelo sensor
w	Conteúdo de vapor d'água colunar na atmosfera

Sumário

Capítulo 1

Introdução

A temperatura regula muitos processos físicos, químicos e biológicos em rios e lagos, como a solubilidade de gases, as taxas de reação, e distribuição de espécies, sendo um parâmetro importante de qualidade da água, muitas vezes usado como um "prognóstico" da saúde destes ecossistemas (Allan e Castillo, 2007; Woodward et al., 2016). Com a mudança climática alterando a climatologia em várias escalas, os padrões de temperaturas máximas, médias e mínimas, de degelo e de mistura destes corpos d'água têm sido afetados (Schneider e Hook, 2010; van Vliet et al., 2013; O'Reilly et al., 2015; Woolway e Merchant, 2018; Sharma et al., 2019). Contudo, o impacto destas mudanças não é uniforme, mas varia de acordo com várias características climatológicas (locais ou regionais), morfológicas e geográficas (O'Reilly et al., 2015; Sharma et al., 2019), e para analisar estes efeitos se faz necessário o estudo individual de cada corpo d'água. Por isso, recentes estudos tentaram reconstruir séries longas de temperatura destes corpos d'água, para a possibilidade de analisar não só o efeito desta mudança, mas de outros impactos antropogênicos (Schneider e Hook, 2010; Matulla et al., 2018). Além disso, como mostrado no trabalho de Gray et al. (2018), longas séries (30 anos ou mais de dados) são necessárias para se obter valores de tendências da temperatura da água que sejam significantes estatisticamente, o que salienta a necessidade de séries consistentes de temperatura de lagos e rios.

Apesar de sua grande importância, dados de temperatura da água são escassos (Webb et al., 2008). No Brasil, por exemplo, dentro do pequeno número de estações que fazem este tipo de monitoramento em rios, a maioria é manual, com baixa frequência de medições e com pouco monitoramento contínuo efetivamente registrado. Em lagos, o monitoramento é feito quase que exclusivamente em grandes lagos artificiais (reservatórios) por empresas públicas e privadas, para monitorar a qualidade da água para abastecimento

humano, ou por instituições de pesquisa, como é o caso da Lagoa Mangueira, monitorada pelo Grupo de Pesquisa em Limnologia e Tecnologia da UFRGS (*e.g.* Fragoso Jr et al., 2011; Cavalcanti et al., 2016; Bohnenberger et al., 2018). Devido a esta limitação, uma aplicação crescente na literatura é o uso de sensoriamento remoto para estimativas da temperatura superficial de corpos d'água, de modo a fornecer dados para estes corpos d'água sem medições de campo, ou para complementar o monitoramento em corpos d'água em que estas medições são realizadas, dada a alta resolução espacial e/ou temporal dos sensores remotos (*e.g.* Torgersen et al., 2001; Kay et al., 2005; Handcock et al., 2006; Crosman e Horel, 2009; Fricke e Baschek, 2013; Allan et al., 2016; Prats et al., 2018). Enquanto no segundo caso a validação de produtos de sensoriamento remoto pode ser feita no objeto de estudo, com os dados *in situ*, no primeiro isto depende de validações de diferentes sensores em outros locais com dados. Além disso, há uma variedade de sensores que podem ser utilizados para este fim, com diferentes resoluções espaciais, temporais e radiométricas, e por isto são importantes estudos que realizam a validação destes sensores em diferentes corpos d'água com diferentes características geográficas e morfológicas, como realizado nos trabalhos de Schneider e Mauser (1996), Reinart e Reinhold (2008), Crosman e Horel (2009), Lamaro et al. (2013) e Liu et al. (2015).

Além da importância para estudos de rios *per se*, a temperatura de rios tributários também pode influenciar nos perfis de temperatura de lagos e reservatórios, de forma local ou até mais abrangente no corpo d'água (Fenocchi et al., 2017), e, por isso, na modelagem ecológica destes corpos d'água, esses dados de temperatura são entrada junto com a vazão dos rios para os modelos, como no modelo IPH-ECO (Fragoso Jr et al., 2009), por exemplo. Como muitos dos processos ocorrendo em lagos e reservatórios dependem da temperatura, nos casos em que os tributários são importantes a correta modelagem da temperatura e destes processos depende da entrada destes dados de forma acurada (Fenocchi et al., 2017; Vinnå et al., 2017). Contudo, por causa desta escassez de dados e por estes modelos necessitarem da temperatura dos rios no ponto de deságue no lago (ou próximo, considerando que a sua temperatura varie pouco neste intervalo), o que é ainda mais raro, muitas vezes se é considerado uma temperatura constante para todos os rios tributários ao lago (*e.g.* Munar, 2017). Nestes casos, uma opção é o uso de modelos de temperatura para se gerar séries contínuas de temperatura de rios, na resolução temporal (geralmente horária ou diária) desejada, a partir de outros dados mais facilmente disponíveis, como de temperatura do ar (Webb et al., 2008). Além disso, o trabalho de Piccolroaz et al. (2018), analisando o impacto de aumentos previstos na temperatura do ar na temperatura superficial de um lago utilizando um modelo de temperatura de lagos, bastante similar aos modelos de rios, mostra o potencial destes modelos em se avaliar os possíveis impactos da mudança climática em corpos hídricos. Entretanto, estes modelos ainda precisam ser calibrados com dados de temperatura da água, o que limita a sua aplicação. Então, outras formas de calibração e validação dos modelos devem ser utilizadas, de forma a suprir a falta

de dados medidos de temperatura da água. Nesse sentido, o uso de dados de sensoriamento remoto é uma opção ainda a ser explorada, pois apesar de seu potencial, foi utilizada em poucos estudos na literatura (Handcock et al., 2012; Dugdale et al., 2017).

Sendo assim, neste trabalho fizemos: *(i)* uma validação de dois sensores a bordo de satélites na estimação da temperatura da água em um lago brasileiro; e *(ii)* a validação do uso de modelos de temperatura calibrados com dados de sensoriamento remoto para a geração de séries contínuas de temperatura da água de rios. Neste capítulo, será dada uma breve fundamentação teórica sobre modelos de temperatura da água e o sensoriamento remoto da temperatura, os objetivos deste trabalho, e a organização dos capítulos desta dissertação.

1.1 Modelos de temperatura de rios

O interesse na temperatura dos rios vem crescendo principalmente devido à necessidade de se entender os impactos antropogênicos (principalmente do desflorestamento, de emissários industriais e da redução de vazão) e da mudança climática nos rios (Webb et al., 2008). O conhecimento dos processos e do padrão de comportamento da temperatura da água é necessário para prever o impacto destes efeitos antropogênicos e de cenários de aquecimento global, além de ser importante para um bom manejo dos recursos hídricos (Caissie, 2006; Orr et al., 2015). Muitos processos regulam a temperatura de um rio, como a fonte da água, a contribuição da água subterrânea, a sua vazão, a cobertura de mata ciliar e a morfologia do rio, por exemplo (Ward, 1985; Sullivan e Adams, 1991 *apud* Poole e Berman, 2001). A incidência de radiação solar é, obviamente, um fator essencial no aumento da temperatura do rio (Edinger et al., 1968), e esta é influenciada principalmente pela sua morfologia (canais mais largos e rasos recebem mais energia do que estreitos e profundos) e pela cobertura, tanto de nuvens quanto vegetação sobre o rio, dependendo ainda do tipo e da densidade de vegetação ciliar e da orientação do canal em relação ao sol (Garner et al., 2017; Dugdale et al., 2018). Ambientes lóticos tendem a entrar em equilíbrio com a condição climática, no que é chamado de "temperatura de equilíbrio"; esta é determinada principalmente pela temperatura do ar, além do vento e condições atmosféricas como a pressão de vapor (Edinger et al., 1968). Como esta temperatura de equilíbrio está em constante mudança (junto com as condições meteorológicas), a temperatura do rio está sempre tendendo à temperatura de equilíbrio, mas com um retardo de tempo, atingindo este equilíbrio em apenas duas ocasiões no dia (devido ao aumento e diminuição da temperatura mais bruscos, pela manhã e pela noite) (Edinger et al., 1968; Gu et al., 1998; Caissie et al., 2005). Águas subterrâneas possuem temperatura mais constante e menor em relação às superficiais, e por isso rios que recebem maior contribuição desta fonte geralmente exibem um temperatura mais constante (Ward, 1985). Uma maior vazão significa menor influência das condições atmosféricas e de águas subterrâneas em sua

temperatura, o que "amortece" a temperatura dos rios a curto prazo; a temperatura de rios menores, por exemplo, é mais suscetível a variações atmosféricas, mas um aumento de volume pode blindá-los de flutuações de curto prazo (Mosley, 1982 *apud* Ward, 1985). Além disso, a latitude também tem fundamental importância: na Nova Zelândia, por exemplo, um estudo amostrando 254 rios mostrou que a latitude e a altitude correspondiam por 73% da variação da temperatura média anual da água (Mosley, 1982 *apud* Ward, 1985).

O conhecimento de como estes diversos fatores influenciam a temperatura dos rios vem sendo desenvolvido a partir de medições da temperatura de rios e comparação com cada variável. Contudo, como este comportamento é de certa forma individual para cada corpo d'água, nos casos em que não há dados *in situ* suficientes para esta análise, uma opção é gerar uma série de temperatura da água utilizando outros dados disponíveis. Esta é uma tarefa complexa, considerando que ela é o resultado desta grande variedade de fatores, mas a curto prazo, as condições climáticas locais e a morfologia do corpo d'água são as que mais influenciam na variação da temperatura de rios (Caissie, 2006). Por isso, na modelagem de séries de temperatura de rios numa escala de tempo diária, dois dados serão geralmente mais importantes: a temperatura do ar, sua principal forçante (Caissie et al., 2001; Webb et al., 2008), e a vazão do rio (Stefan e Preud'homme, 1993; Gu et al., 1998; Toffolon e Piccolroaz, 2015). Muitos modelos para estimar a temperatura de rios foram propostos, dividindo-se em três grandes grupos: regressões lineares (*e.g.* Crisp e Howson, 1982), modelos estocásticos (*e.g.* Kothandaraman, 1971; Cluis, 1972), e modelos determinísticos (*e.g.* Sinokrot e Stefan, 1993).

Regressões são bastante úteis devido à sua simplicidade, utilizando uma função linear simples (Crisp e Howson, 1982) ou uma função logística (Mohseni et al., 1998), por exemplo, e relacionando a temperatura da água apenas à temperatura do ar. Modelos estocásticos são mais complexos que as regressões, mas também dependem da calibração para a região de estudo (são "empíricos"), e podem ser aplicados numa escala de tempo diária, também necessitando, geralmente, apenas dados de temperatura do ar (Caissie et al., 2001; Caissie, 2006). Modelos determinísticos são bem mais complexos, baseando-se nas equações físicas de transferência de energia, podendo ser baseados também no conceito de temperatura de equilíbrio, e têm a vantagem de poderem ser aplicados em variadas escalas espaciais e até em locais onde não há dados de temperatura da água disponíveis (Mohseni e Stefan, 1999; Caissie et al., 2005). Sua aplicação, contudo, ainda é limitada, pois necessitam de um grande número de dados para calibração, principalmente meteorológicos (Caissie, 2006; Dugdale et al., 2017).

Piccolroaz et al. (2016) compararam diversos modelos, como regressões lineares, o modelo estocástico usado por Caissie et al. (2001), o modelo *air2stream*, desenvolvido por Toffolon e Piccolroaz (2015), e o modelo *air2water*, desenvolvido por Piccolroaz et al. (2013), para rios que são saída de lagos, para gerar séries de temperatura da água para

38 rios suíços com diferentes características hidrológicas, e concluíram que o modelo de Toffolon e Piccolroaz (2015), utilizando o formato com 7 ou 8 parâmetros, têm resultados mais acurados e consistente (com exceção dos rios que são saída de lagos, em que o modelo de lagos é mais acurado), com séries com valor de REMQ de 0,84°C para o período de validação, na média para todos os rios.

Apesar de mostrar melhores resultados, o modelo *air2stream* é um tanto complexo e demanda um certo custo computacional, e para o trabalho não ficar limitado a apenas um modelo, é interessante compará-lo com modelos mais simples e verificar como é a performance de cada um sob a condição de poucos dados para a calibração. Então, com base no estudo de Piccolroaz et al. (2016), foram selecionados os modelos para esta comparação: modelos estocásticos, como usados por Caissie et al. (1998), utilizando duas formas para o cálculo da componente de longo prazo, além do modelo "semiempírico" *air2stream* de Toffolon e Piccolroaz (2015).

1.1.1 Modelo estocástico

No modelo estocástico, a temperatura da água do rio é dividida em duas componentes (Caissie et al., 1998):

$$T_w(t) = \mathrm{LT}_w(t) + \mathrm{ST}_w(t) \tag{1.1}$$

em que $\mathrm{LT}(t)$ é a componente de variação anual, ou a componente de longo prazo, e $\mathrm{ST}(t)$ é a anomalia ou resíduo desta componente, ou a componente de curto prazo.

A componente de variação anual é calculada tanto para a temperatura da água quanto para a do ar, e duas formas podem ser empregadas: uma série de Fourier (Kothandaraman, 1971) ou uma função senoidal (Cluis, 1972). A série de Fourier é dada por:

$$\mathrm{LT}(t) = A_o + \sum_{n=1}^{\infty} \left\{ A_n \cos\left[(t-j-1)\frac{2n\pi}{N}\right] + B_n \mathrm{sen}\left[(t-j-1)\frac{2n\pi}{N}\right] \right\} \tag{1.2}$$

em que A_o é o valor médio da temperatura no período analisado, n é o número de harmônicos utilizados, t é o tempo (em dias, neste caso), j é o primeiro dia de observações no período analisado ($j = 90$, por exemplo, se o período começa no dia 31 de março), N é o total de dias no período analisado, e os A_n e os B_n são calculados por:

$$A_n = \frac{2}{N} \sum_{t=1}^{N} f(t) \cos\left(\frac{2\pi n t}{N}\right) \tag{1.3}$$

e

$$B_n = \frac{2}{N} \sum_{t=1}^{N} f(t) \mathrm{sen}\left(\frac{2\pi n t}{N}\right) \tag{1.4}$$

para os n harmônicos utilizados, em que $f(t)$ é o valor da temperatura (da água ou do ar) no dia t.

A função senoidal é dada por:

$$\mathrm{LT}(t) = a + b\mathrm{sen}\left[\frac{2\pi}{N}(t + t_o)\right] \tag{1.5}$$

em que a, b e t_o são coeficientes que devem ser estimados, por exemplo, pelo método dos mínimos quadrados (Cluis, 1972).

Depois de calculados os valores das componentes anuais de temperatura LT do ar e da água para o período analisado, os dados de temperatura são subtraídos da sua respectiva componente, restando o resíduo de cada série. Para modelar a componente de curto prazo do modelo, no trabalho de Caissie et al. (1998) foram utilizados 3 métodos: uma regressão múltipla (Kothandaraman, 1971), um processo de Markov de segunda ordem (Cluis, 1972), e o método de Box-Jenkins (Box e Jenkins, 1976). Dada a similaridade dos resultados encontrados por Caissie et al. (1998), e pela facilidade da implementação da regressão múltipla, este método foi o escolhido para ser utilizado neste trabalho.

O método da regressão múltipla consiste em calcular a regressão linear entre a série de temperatura da água e as séries de temperatura do ar sem retardo, com retardo de 1 dia, e com retardo de 2 dias, usando a seguinte equação:

$$R_w(t) = \beta_1 R_a(t) + \beta_2 R_a(t-1) + \beta_3 R_a(t-2) \tag{1.6}$$

em que $R_w(t)$ e $R_a(t)$ são os resíduos das séries de temperatura da água e do ar no tempo t, respectivamente, e β_n são os três coeficientes da regressão. Com os valores dos coeficientes β_1, β_2 e β_3 calculados para o período de calibração, para os demais anos do período de validação eles são utilizados com os valores dos resíduos $R_a(t)$ de cada ano para calcular a componente ST_w, e somá-la à componente anual LT_w para cada dia (equação 1.1), obtendo uma série de temperatura da água para todo o período analisado.

1.1.2 Modelo determinístico

O modelo *air2stream* de Toffolon e Piccolroaz (2015) é um modelo de base física para gerar a partir da temperatura do ar e da vazão uma série de dados de temperatura da água de um rio. Foi desenvolvido recentemente a partir do modelo *air2water* (Piccolroaz et al., 2013), que modela a temperatura superficial de lagos a partir da temperatura do ar, e vem mostrando boa eficiência (Piccolroaz et al., 2016) e atraindo aplicações (Fenocchi et al., 2017; Cai et al., 2018; Piotrowski e Napiorkowski, 2018), apesar de sua recente publicação. Ele usa uma equação de balanço de calor concentrada, aplicada a trechos de rio, e considera que o balanço das trocas de calor entre a superfície da água e a atmosfera é uma função da temperatura do ar (Mohseni e Stefan, 1999; Caissie et al., 2005). Este modelo faz algumas simplificações, aproximando a derivada do fluxo de calor por uma série de Taylor de primeira ordem e substituindo os fluxos de calor que saem e entram no volume de controle (o trecho de rio) por um valor médio e um termo de variação sazonal,

por exemplo, para chegar em uma equação diferencial ordinária com 8 parâmetros que precisam ser calibrados, isto é, adicionando uma parcela empírica ao modelo físico, já que os parâmetros variam de trecho de rio para trecho de rio. A equação deste modelo é:

$$\frac{dT_w}{dt} = \frac{1}{\delta}\left\{a_1 + a_2 T_a - a_3 T_w + \theta\left[a_5 + a_6 \cos\left(2\pi\left(\frac{t}{t_y} - a_7\right)\right) - a_8 T_w\right]\right\} \tag{1.7}$$

em que T_w é a temperatura da água, $\theta = \frac{Q}{\bar{Q}}$, Q é a vazão do rio no passo de tempo e $\bar{Q}$ é a vazão média do rio no período analisado, δ é igual a θ^{a_4}, T_a é a temperatura do ar, t é o passo de tempo atual, t_y é o total de passos de tempo num ano (número de dias no ano, se o passo de tempo for diário), e os a_n, $n = 1, 2, 3, .., 8$, são os 8 parâmetros calibráveis do modelo.

A cada iteração do modelo, esta equação diferencial é integrada numericamente no tempo para a escala definida, e a calibração é feita usando um algoritmo de otimização para minimizar uma função-objetivo, que mede uma diferença entre as temperaturas do rio observadas e simuladas. Os autores ressaltam que este processo de calibração tem a vantagem de representar outros efeitos locais que não são levados em conta diretamente na equação do balanço de calor, como o sombreamento da vegetação.

O modelo necessita de 3 dados de entrada para sua calibração e validação: temperatura do ar, vazão do rio e temperatura da água do rio diárias. Com todos estes dados, a rotina, que foi disponibilizada pelos autores, é então rodada para o período desejado, sendo necessária apenas a definição do número de parâmetros, dos 8 possíveis, a serem utilizados, o esquema de integração numérica, o algoritmo de otimização, e a função-objetivo.

1.1.3 Uso de sensoriamento remoto com os modelos

A principal limitação para a aplicação destes modelos é que é necessário fazer calibração e verificação dos mesmos para o objeto de estudo, necessitando de dados *in situ* de temperatura da água. Para muitos rios, a escassez de dados inviabiliza a aplicação deste método, e numa tentativa de suprir esta falta de dados, neste trabalho foram usados dados de sensoriamento remoto para estimar a temperatura da água (Webb et al., 2008; Handcock et al., 2012). Este tipo de medição, apesar de ter algumas limitações, é crescente e já bem estabelecida, pois possibilita avaliar a variação da temperatura no espaço e ao longo de um grande intervalo de tempo, a depender da disponibilidade da dados de sensores de satélites (Kay et al., 2005; Handcock et al., 2006).

Na hidrologia, o uso de dados de sensoriamento remoto, principalmente altimétricos e de uso do solo, para validação de diversos modelos é bem estabelecido (*e.g.* Schott et al., 2001; Paiva et al., 2013; Allan et al., 2016; Li et al., 2017; Munar et al., 2018), contudo o uso de sensoriamento remoto para calibração de modelos é mais restrito (Dugdale et al., 2017). Em se tratando de uso de temperatura da água derivada de produtos de

sensoriamento remoto, tem-se conhecimento apenas os trabalhos de Sima et al. (2013), usando a temperatura superficial do lago Urmia, no Irã, estimada pelo MODIS, para estimativa da sua evaporação utilizando um modelo empírico, e de Pahlevan et al. (2011), que utilizou um mapa de temperatura de superfície do lago Ontário, na divisa entre Canadá e EUA, derivado do Landsat 7 ETM+, para calibrar um modelo hidrodinâmico 3D, modelando uma pluma termal formada por uma descarga no lago, além dos trabalhos de Boyd e Kasper (2003) e de Cristea e Burges (2009), que utilizaram temperaturas derivadas de imagens de sensores a bordo de aeronaves para calibrar modelos de temperatura. Nesse sentido, validar a calibração de modelos de temperatura da água utilizando apenas dados de sensores a bordo de satélites é importante para fornecer um subsídio a esta técnica que, apesar de ter sido recomendada por Handcock et al. (2012), ainda não apresenta aplicações na literatura.

1.2 Sensoriamento remoto da temperatura

O sensoriamento remoto da temperatura superficial (ST) é uma prática já bem estabelecida na literatura, com diversos sensores, com diferentes resoluções, desenvolvidos e sendo aplicados para este fim, como o AVHRR, as missões Landsat, os sensores MODIS e ASTER, a bordo dos satélites Terra e Aqua, e as recentes missões Sentinel (Price, 1984; Schneider e Mauser, 1996; Gao et al., 2006; Li et al., 2013). Com a popularização do sensoriamento remoto da temperatura e o barateamento de drones, recentemente muitos trabalhos vêm sendo feitos utilizando essas tecnologias em estudos hidrológicos, principalmente de rios e córregos, utilizando sensores acoplados a drones, na literatura conhecidos como *"airborne thermal infrared remote sensing"* (*e.g.* Fricke e Baschek, 2015; Vatland et al., 2015), ou com o uso de câmeras termais (*e.g.* Wawrzyniak et al., 2013; Marruedo Arricibita et al., 2018). Contudo, o foco deste trabalho são os sensores a bordo de satélites, e por isto sensoriamento remoto fará referência apenas a estes sensores, com exceção dos casos em que seja especificado.

1.2.1 Resoluções dos sensores

Antes de introduzir os princípios físicos e aplicações do sensoriamento remoto, é importante definir como os sensores são descritos. Quatro resoluções definem as características das imagens providas por um sensor (Purkis e Klemas, 2011):

- *Resolução espacial:* é uma medida do detalhamento da superfície imageada pelo sensor. Determina a menor área superficial que pode ser representada por um pixel da imagem. Sua unidade é a representação do tamanho do lado de um pixel da imagem, por isto, quanto menor o valor da distância, maior a resolução. Um exemplo é a resolução do sensor MODIS, que varia de 250 a 1000 m.

- *Resolução temporal:* é uma medida da frequência de visitação do sensor a uma mesma área, ou seja, não é uma medida das imagens em si, mas da série de imagens geradas pelo sensor. Para os satélites, ela depende principalmente das características das órbitas e da resolução espacial das imagens. Sua unidade é a distância temporal entre duas imagens, como 16 dias para o Landsat 5 TM, por exemplo.

- *Resolução espectral:* discriminação das bandas espectrais, suas larguras, e a sensibilidade do sensor em cada uma delas (Jensen, 2009).

- *Resolução radiométrica:* é uma medida do sensor quanto a sensibilidade à radiância incidente. Ela pode ser definida em função do número de bits utilizados pelo sensor para guardar a informação medida: o Landsat ETM+, por exemplo, possui uma resolução radiométrica de 8 bits, discriminando, então, 256 ($2^8 = 256$) níveis de radiação diferentes, enquanto que o MODIS possui 12 bits, discriminando 4096 ($2^{12} = 4096$) níveis diferentes. Para os sensores termais, isso é medido pela diferença de temperatura equivalente ao ruído (do inglês *"noise equivalent temperature difference"*) – NEΔT. As bandas termais do MODIS, por exemplo, têm NEΔT de 0,05°C a 27°C (Barnes et al., 1998), enquanto que a banda termal do Landsat 7 ETM+ tem NEΔT de 0,22°C a 7°C (Barsi et al., 2003b).

1.2.2 Princípios físicos do sensoriamento remoto

Há três faixas de comprimentos de onda, dentre as janelas atmosféricas, tradicionalmente utilizados para estimativas da temperatura superficial: o MWIR (infravermelho de onda média), tipicamente na faixa de 3 a 5 µm, o TIR (infravermelho termal), geralmente na faixa de 10 a 12 µm, e as micro-ondas, na faixa de 1 mm a 1 m, mas geralmente utilizadas na faixa da banda Ka, entre 7,5 e 10 mm. As bandas do MWIR são utilizadas apenas para sensoriamento da temperatura oceânica, no sensor MODIS, e só podem ser utilizados durante a noite por serem muito sensíveis aos efeitos de reflexão e espalhamento da radiação solar na água (Kilpatrick et al., 2015). No caso das micro-ondas, como a energia emitida pela superfície é muito menor nesta faixa espectral, a resolução radiométrica destes sensores precisa ser muito maior do que na faixa do infravermelho para estimar a temperatura de superfície, o que, em prática, significa sensores com uma resolução espacial muito grosseira (da ordem de quilômetros), ou então no uso de sensores ativos, isto é, que emitem radiação neste comprimento de onda, o que aumenta a sua resolução espacial, mas limita a distribuição espacial e temporal com que são geradas as informações (Jensen, 2009). Portanto, o sensoriamento da temperatura é tipicamente realizado utilizando sensores na faixa do TIR.

O sensoriamento remoto da temperatura na faixa do TIR se baseia no fato de que todo corpo emite energia na forma de radiação eletromagnética, e esta energia é

proporcional à sua temperatura e à sua emissividade. Portanto, o sensoriamento remoto nesta faixa do espectro se baseia na energia emitida pelos corpos, e não na radiação solar incidente que é refletida pela superfície, como é medido nas faixas de menor comprimento de onda, como o visível e o NIR (infravermelho próximo). Por isso, a temperatura medida no TIR é chamada de temperatura radiométrica, que é diferente da temperatura medida pelo fluxo de calor, a temperatura termodinâmica ou cinética. Para superfícies isotérmicas e homogêneas, em equilíbrio térmico, essas temperaturas são iguais; como estes casos quase nunca são encontrados, estas temperaturas quase sempre são diferentes (Li et al., 2013), usualmente na faixa de décimos ou centésimos de diferença (Handcock et al., 2012).

As relações entre radiação emitida e temperatura de uma superfície são formuladas matematicamente pelas leis de Planck, lei do deslocamento de Wien (derivada da lei de Planck), lei de Stefan-Boltzmann e pela lei de Kirchhoff (Jensen, 2009). Estas leis são enunciadas para um corpo negro, que é um corpo teórico (idealizado) que, em equilíbrio térmico com o ambiente, emite radiação eletromagnética na maior taxa (energia por tempo) possível. A partir desta definição, define-se também a emissividade, que é a razão entre a emissão de radiação eletromagnética de um corpo e um corpo negro; em outras palavras, um corpo negro possui emissividade 1, e todas superfícies reais possuem emissividade entre 0 e 1, a depender de sua temperatura e da faixa espectral observada (Purkis e Klemas, 2011). A lei de Planck, base do sensoriamento remoto termal, relaciona a temperatura de um objeto com a radiância espectral por ele emitida nos diferentes comprimentos de onda. Para um corpo negro, ela é dada por (Schott, 2007):

$$B_\lambda(\lambda, T) = \frac{c_1}{\lambda^5 \exp\left(\frac{c_2}{\lambda T}\right) - 1} \tag{1.8}$$

em que B é a radiância espectral emitida pelo corpo, no comprimento de onda λ e a uma temperatura T, e c_1 e c_2 são as constantes de Planck, e valem $c_1 = 1,191 \times 10^8$ W μm^4/m^2 sr e $c_2 = 1,439 \times 10^4$ Kμm, respectivamente.

A lei de Stefan-Boltzmann, derivada da lei de Planck, determina que a energia total irradiada por um corpo negro é proporcional à quarta potência da sua temperatura absoluta. Também derivada a partir da lei de Planck, a lei do deslocamento de Wien determina o comprimento de onda em que ocorre o pico de emissão de radiação eletromagnética por um corpo. Ela é dada por (Jensen, 2009):

$$\lambda_{\max} = \frac{a}{T} \tag{1.9}$$

em que a é uma constante e vale 2898 μm/K. A partir desta equação, podemos ver que o comportamento de corpos à temperatura ambiente (~300 K) e o Sol (~5800 K) são distintos. Como observado na Figura 1.1, para o Sol (que tem comportamento próximo a um corpo negro) o pico de emissão ocorre entre 400 e 700 nm, que é a lux visível. Já para a Terra (que também se aproxima a um corpo negro) e objetos a esta temperatura,

o pico de emissão ocorre entre 8 e 14 µm, ou seja, na faixa do TIR. Por isso, há uma alta quantidade de energia emitida pelos corpos à temperatura ambiente nessa faixa do espectro, o que permite a sua medição com uma boa resolução espacial (para o Landsat TM, por exemplo, a resolução para menores comprimentos de onda, como visível e NIR, é de 30 m, enquanto que a da banda termal é de 120 m).

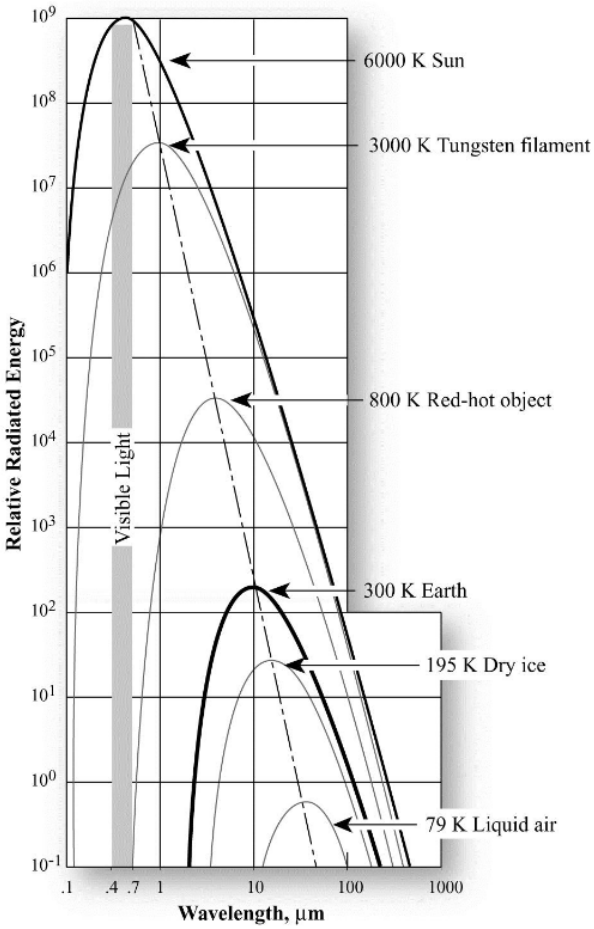

Figura 1.1 – Curvas de emissão de radiação eletromagnética de corpo negro a várias temperaturas. (Fonte: Jensen, 2009)

A lei de Kirchhoff enuncia que, para um objeto em equilíbrio termodinâmico, sua emissividade é igual a sua absortividade. Isso significa que, para objetos com alta emissividade na faixa do infravermelho termal, grande parte da radiação emitida pelo Sol e que chega à superfície é absorvida, e o restante é refletida para o ambiente. Isto também contribui que o sensoriamento da temperatura seja realizado na faixa do TIR, considerando apenas a energia emitida pela superfície e captada pelo sensor, a partir da inversão da lei de Planck, e conhecendo a emissividade da superfície, obtendo-se o que é chamado de *temperatura de brilho* da superfície.

1.2.3 Sensores utilizados

Como mencionado anteriormente, alguns sensores a bordo de satélites foram desenvolvidos com pelo menos uma banda termal, com a possibilidade de se fazer a estimativa da temperatura da superfície. Na Tabela 1.1 estão listados os sensores termais a bordo de satélite desenvolvidos até o momento. Contudo, este trabalho se limitará a tratar de dois sensores: o MODIS, a bordo dos satélites Terra (imageamento matutino) e Aqua (imageamento noturno), e o Landsat 7 ETM+. Estes dois foram escolhidos principalmente devido a sua longa série de imagens, com o Landsat 7 sendo lançado em 1999, e o Terra iniciando o imageamento em 2000, ao grande número de trabalhos na área que utilizam estes dois sensores (*e.g.* Handcock et al., 2006; Reinart e Reinhold, 2008; Crosman e Horel, 2009; Liu et al., 2015; Allan et al., 2016; Yang et al., 2018), e a complementação, em termos de monitoramento: ambos imageiam uma mesma área (por volta das 10h da manhã, horário local) com um intervalo de diferença de até 30 minutos. O Landsat 7 ETM+ possui resolução espacial de 30 m, com exceção de sua banda termal, que é de 60 m, e resolução temporal de 16 dia, enquanto as imagens do MODIS são diárias e sua banda termal possui resolução espacial de 1000 m. Além disso, apesar do MODIS contar com muito mais bandas do que o Landsat 7 (36 contra 7), as bandas do Landsat possuem faixas do espectro similar às do MODIS (Gao et al., 2006). Portanto, as medições de ambos os sensores não são apenas comparáveis entre si, mas também podem servir como uma forma de complementar o monitoramento realizado por cada sensor. Outra questão importante é que o MODIS possui produtos próprios prontos para download e uso direto, como produtos de NDVI (MOD13), evapotranspiração (MOD16) e temperatura superficial (MOD11 e MOD28), enquanto que para o Landsat, com exceção do Landsat 8, apenas as imagens da radiância estão disponíveis, e o usuário deve utilizar as imagens para gerar estas valores (como a temperatura). Com isto em mente, os temas apresentados nas seções a seguir terão como foco sempre nestes dois sensores, a não ser quando especificado.

Tabela 1.1 – Sensores termais a bordo de satélites.

Sensor/ Satélite	**Período em atividade**	**Resolução espacial**	**Resolução temporal**	**NEΔT (°C) a 300 K***
ATSR-1/ERS-1	Jul/1991–Jun/1996	1000 m	3–168 dias**	0,06–0,13
ATSR-2/ERS-2	Abr/1995–Set/2011	1000 m	35 dias	0,02–0,05
AVHRR/3 (NOA-15 a NOA-19)***	Mai/1998–atual	1090 m	1 dia	0,12
Landsat 4 TM	Jul/1982–Jun/2001	120 m	16 dias	0,17–0,30
Landsat 5 TM	Mar/1984–Nov/2011	120 m	16 dias	0,17–0,30
Landsat 7 ETM+	Abr/1999–atual	60 m	16 dias	0,22 ($B6_2$)
MODIS/Terra	Dez/1999–atual	1000 m	0,5 dia	0,05

Tabela 1.1 – Sensores termais a bordo de satélites.

ASTER/Terra	Dez/1999–atual	90 m	16 dias	0,30
AATSR/Envisat	Mar/2002–Abr/2012	1000 m	35 dias	<0,05
MODIS/Aqua	Mai/2002–atual	1000 m	0,5 dia	0,05
VIIRS/Suomi NPP	Out/2011–atual	750 m	1 dia	0,03
Landsat 8 TIRS	Fev/2013–atual	100 m	16 dias	0,05–0,06
Sentinel-3	Fev/2016–atual	1000 m	0.5–2 dias****	<0,05

*a resolução radiométrica pode variar entre as diferentes bandas e diferentes missões dos sensores

**sensores com diferentes "fases orbitais" em seus períodos de funcionamento, mas a partir de 1995 a resolução ficou fixa em 35 dias

***sensor a bordo de múltiplos satélites

****a depender da posição em relação à orbita dos dois satélites

1.2.4 Correção das imagens termais

Para estudos hidrológicos e do sistema terrestre em escala regional, a temperatura superficial continental (LST, sigla para *land surface temperature*) deve ser estimada com uma acurácia de 1°C ou melhor (Wan e Dozier, 1996; Li et al., 2013). Contudo, é difícil se alcançar esta acurácia desejada, porque a estimativa da temperatura depende de correção de dois efeitos: da emissividade da superfície e dos efeitos atmosféricos (Ottlé e Stoll, 1993; Schott, 2007). A metodologia para correção destes efeitos e então estimar a temperatura superficial corretamente deve seguir o fluxograma da Figura 1.2. Diferentes maneiras foram propostas pra lidar com estas correções de formas distintas, para os diferentes sensores, em vários estudos na literatura, como revisado por Li et al. (2013).

Como descrito em Li et al. (2013), a estimativa da LST e da emissividade ao mesmo tempo é impossível utilizando sensoriamento remoto. Contudo, ela é a grande "ponderadora" da emissão de radiação pela superfície; estudos mostraram que erros na emissividade estão associados em erros na estimativa da temperatura superficial da água (TSA) de 0,2–0,7°C (Friedman, 1969; Jiménez-Muñoz e Sobrino, 2006; Hulley et al., 2011). Por isso, duas opções surgem: o uso de valores fixos de emissividade, ou modelos que usem informações de outras bandas para a estimativa desta, como propostos por Sobrino et al. (2004) e Sobrino et al. (2008) para diversos tipos de usos do solo, por exemplo. No caso da água, esta se aproxima a um corpo negro nos comprimentos de onda de 10–12 µm, como mostrado na Figura 1.3, mas sua emissividade varia com a temperatura, a salinidade, a turbidez e a quantidade de ácido húmico (Wenyao et al., 1987 *apud* Dugdale, 2016; Handcock et al., 2012), por exemplo, e dada esta magnitude de fatores, há grande dificuldade de se estimar um valor de emissividade para cada corpo d'água, pois além da demanda de trabalho de campo e de laboratório para sua aferição, pode variar no

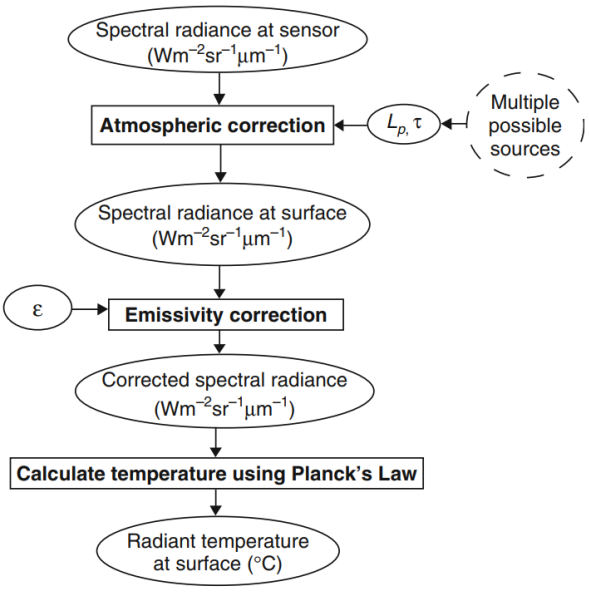

Figura 1.2 – Fluxograma de metodologia para a estimativa da temperatura de superfície a partir de uma imagem TIR. (Fonte: Handcock et al., 2012)

tempo e no espaço. Por isso, em estudos de TSA o que se faz é assumir um valor fixo de emissividade. Uma série de valores foram utilizados na literatura (*e.g.* 0,9925 em Schneider e Mauser, 1996 e 0,98 em Wloczyk et al., 2006), mas dois valores são predominantes: 0,9885 (Lamaro et al., 2013; Simon et al., 2014; Prats et al., 2018), a média do valor médio da emissividade da água medidos pelas bandas 31 e 32 do MODIS (Snyder et al., 1998), e 0,99 (Okwen et al., 2011; Despini e Teggi, 2013; Fricke e Baschek, 2015), um valor aproximado do derivado por Masuda et al. (1988) para a água destilada para uma série de comprimentos de onda e ângulos de visada do sensor. A definição da escolha da emissividade está descrita melhor no Capítulo 2. Além disso, poucos estudos realizaram uma análise de sensibilidade da estimativa da TSA a esta variável (Mao et al., 2005), que é parte do trabalho desenvolvido no Capítulo 2.

A segunda dificuldade é a correção dos efeitos atmosféricos. A radiação emitida pela atmosfera não é a mesma que chega ao sensor (chamada de radiação no topo da atmosfera – TOA, do inglês *top of atmosphere*), mas esta é afetada pela atmosfera, principalmente em função do vapor d'água (Jiménez-Muñoz e Sobrino, 2003). De fato, apesar do espectro do TIR utilizada pelos sensores (10 a 12 μm, geralmente) se situar em uma janela atmosférica, ainda há considerável influência da atmosfera nesta região do espectro, que atua tanto emitindo radiação (em todas as direções, portanto na direção do sensor e também em direção à superfície) quanto absorvendo e refletindo parte da radiação emitida pela superfície, como mostrado na Figura 1.4. Por isto, o sensoriamento remoto da superfície é limitado apenas a pixels sem cobertura de nuvens (*cloud-free pixels*). A não-remoção destes efeitos, isto é, calcular a temperatura de brilho diretamente utilizando a radiação TOA medida pelo sensor pode acarretar em erros de até 2°C, em casos de rios

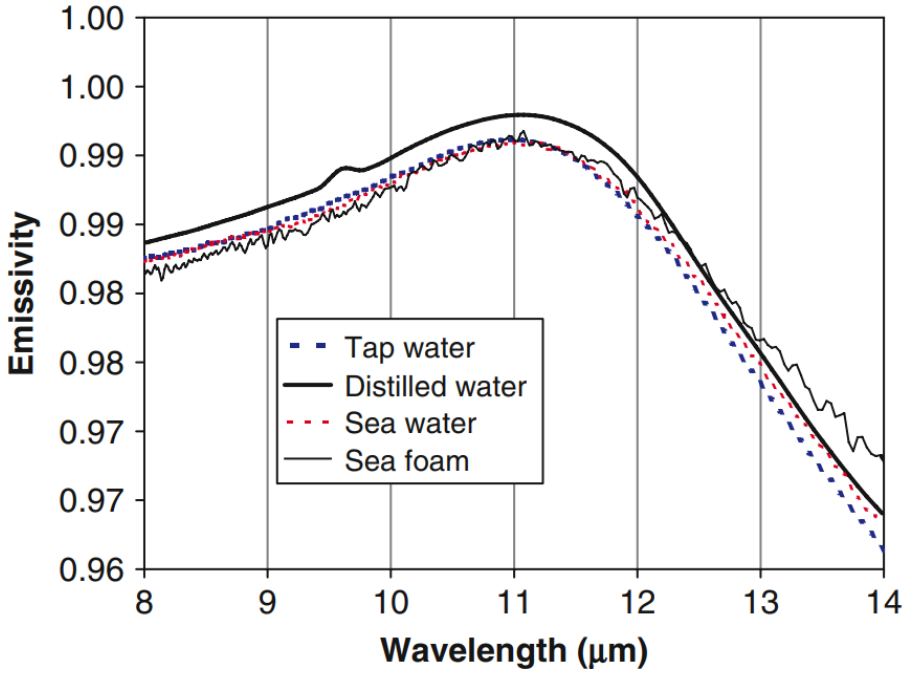

Figura 1.3 – Emissividade da água destilada (*destilled water*), da torneira (*tap water*), do mar (*sea water*) e da espuma do mar (*sea foam*) na faixa de 8–14 μm do TIR. (Fonte: Handcock et al., 2012, a partir de Zhang, 1999)

e lagos (Kay et al., 2005). A correção destes efeitos é feita apenas com o conhecimento dos perfis verticais da temperatura e da quantidade de vapor d'água atmosféricos (Perry e Moran, 1994 *apud* Li et al., 2013).

Estes efeitos são dados por três variáveis: τ, a transmissividade da atmosfera (sem unidade), que é uma medida da interação entre a atmosfera e a radiação em dado comprimento de onda e varia de 0 (totalmente opaca) a 1 (totalmente transparente), L_{up} (*upwelling radiance*), que é a quantidade de radiação emitida pela atmosfera na direção do sensor, e L_{down} (*downwelling radiance*), que é a quantidade de radiação emitida ou refletida pela atmosfera na direção da superfície, cujas unidades são as mesmas da radiação absorvida pelo sensor. Para cada pixel, a radiação TOA medida pelo sensor é dada por (Schott, 2007):

$$L_{\text{sensor}} = [\varepsilon B + (1-\varepsilon)L^{\text{down}}]\tau + L^{\text{up}} \tag{1.10}$$

em que L_{sensor} é a radiação medida pelo sensor (TOA, em W/(m^2 sr μm), e ε é a emissividade da superfície.

Com o uso de modelos de transferência radiativa, como os modelos MODTRAN e Lowtran, é possível fazer a estimativa destas variáveis usando os perfis de temperatura e vapor d'água da atmosfera para se chegar ao valor corrigido de radiação emitida pela superfície imageada. A correção da radiação é feita usando a seguinte equação (Schott, 2007):

$$L_{\text{corr}} = \frac{L_{\text{sensor}} - L^{\text{up}} - \tau L^{\text{down}}(1-\varepsilon)}{\varepsilon\tau} \tag{1.11}$$

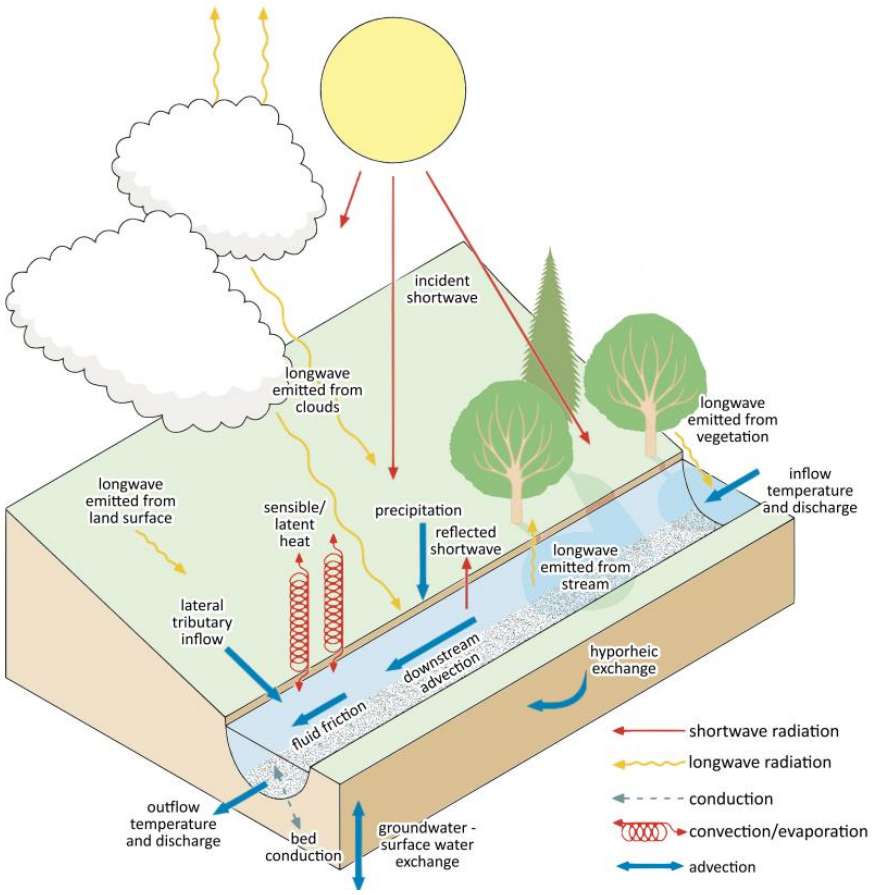

Figura 1.4 – Os diversos fluxos de calor e energia num trecho de rio, mostrando as diversas fontes de radiação TIR (em amarelo) que podem influenciar na radiação emitida pelo rio que é medida pelo sensor. (Fonte: Handcock et al., 2012)

Com o valor corrigido de L e da emissividade da água, é possível, então, se calcular a temperatura de superfície invertendo a lei de Planck (Equação 1.8).

Contudo, esses valores de correção dependem de perfis acurados da atmosfera, que nem sempre estão disponíveis, e dos modelos de transferência radiativa, que são softwares privados e caros (Li et al., 2013). Por isso, outros modelos foram desenvolvidos com este intuito, e que podem ser divididos em três grandes grupos, considerando que a emissividade da superfície seja conhecida (Li et al., 2013): com uma banda termal, com várias bandas termais, ou uma aproximação multi-ângulo. Aqui, apenas os dois primeiros grupos serão tratados, pois o primeiro inclui os sensores Landsat, e o segundo grupo inclui o MODIS.

No caso do Landsat, a radiação medida pelo sensor é diretamente corrigida na Equação 1.11, utilizando informações auxiliares para prover os valores das variáveis atmosféricas. Atualmente, há várias fontes de perfis atmosféricos que podem ser utilizadas como entrada para os modelos de transferência radiativa. O principal e mais acurado é o uso de dados locais de radiossonda, a bordo de balões meteorológicos (Jiménez-Muñoz et al., 2010; Allan et al., 2016). Como estes dados são de muito difícil obtenção, é possível utilizar dados globais providos pelo Centro Nacional para Predição Ambiental

(NCEP/NOAA), nos EUA, produtos de reanálise, e até um produto MODIS, o MOD07 (Jiménez-Muñoz et al., 2010; Coll et al., 2012). Por causa do necessário uso de softwares pagos, a NASA desenvolveu uma plataforma online gratuita, o AtmCorr (*Atmospheric Correction Parameter Calculator*, disponível em `https://atmcorr.gsfc.nasa.gov/`) para gerar estes perfis atmosféricos e os parâmetros de correção atmosférica para os sensores Landsat (Barsi et al., 2003a, 2005). Estes parâmetros são interpolados de uma grade de 1° × 1°, gerados a cada 6h pelo NCEP, para o dia, hora e local desejado. Apesar de esta ser uma estimativa menos precisa, dada a resolução espacial mais grosseira dos parâmetros atmosféricos, esta plataforma tem mostrado bons resultados em estudos relacionados à TS (Jiménez-Muñoz et al., 2010; Coll et al., 2012; Lamaro et al., 2013; Fricke e Baschek, 2013).

Dada a escassez de dados atmosféricos, dois algoritmos foram propostos para simplificar a RTE. O algoritmo de Qin et al. (2001), chamado de *mono-window* (janela única), que depende apenas do conhecimento da temperatura do ar e do conteúdo de vapor d'água, e pode ser aplicado apenas ao Landsat 5 TM. Em uma tentativa similar, Jiménez-Muñoz e Sobrino (2003) desenvolveram um algoritmo, chamado de *single-channel* (canal único), inicialmente para o Landsat 5 TM, e atualizado por Jiménez-Muñoz et al. (2009) para incluir os sensores Landsat 4 TM e 7 ETM+. Neste algoritmo, os parâmetros atmosféricos foram substituídos por chamadas funções atmosféricas, que dependem apenas do conteúdo de vapor d'água atmosférico, e ajustados polinômios de segundo grau a eles, considerando um grande número de perfis atmosféricos (com temperaturas de superfície variando de 250 K a 320 K e quantidade de vapor d'água atmosférico variando desde 0,15 g/cm^2 a 6,71 g/cm^2) e utilizando o MODTRAN. Neste algoritmo, a temperatura superficial é dada por:

$$\mathrm{ST} = \gamma[\varepsilon^{-1}(\psi_1 L_{\mathrm{sensor}} + \psi_2) + \psi_3 - L_{\mathrm{sensor}}] + T_{\mathrm{sensor}} \tag{1.12}$$

em que T_{sensor} é a temperatura de brilho, ψ_1, ψ_2, e ψ_3 são as funções atmosféricas, e γ é uma função calculada por:

$$\gamma = \left[\frac{c_2 L_{\mathrm{sensor}}}{T^2_{\mathrm{sensor}}}\left(\frac{\lambda^4_{\mathrm{eff}}}{c_1} L_{\mathrm{sensor}} + \lambda^{-1}_{\mathrm{eff}}\right)\right]^{-1} \tag{1.13}$$

em que c_1 e c_2 são as constantes de Planck, e λ_{eff} é o comprimento de onda efetivo da banda TIR. A relação entre estas funções atmosféricas e os parâmetros atmosféricos se dá por:

$$\begin{aligned} \psi_1 &= \frac{1}{\tau} \\ \psi_2 &= -L^{\mathrm{down}} - \frac{L^{\mathrm{up}}}{\tau} \\ \psi_3 &= L^{\mathrm{down}} \end{aligned} \tag{1.14}$$

e são calculadas por:

$$\psi_n = c_n w^2 + b_n w + a_n \tag{1.15}$$

em que $n = 1, 2, 3$; w é o conteúdo de vapor d'água, e a, b, e c são as constantes encontradas em Jiménez-Muñoz et al. (2009), de acordo com a base de dados de perfis atmosféricos. O algoritmo também foi atualizado por Cristóbal et al. (2009) para incluir a temperatura do ar no cálculo das funções atmosféricas, o que mostrou melhora de sua acurácia.

A principal limitação destes algoritmos é que, em geral, eles têm uma grande perda de performance quando há alta quantidade de vapor d'água na atmosfera, devido à relação empírica entre as funções atmosféricas e os parâmetros atmosféricos ser instável quando o valor de w é alto (Jiménez-Muñoz et al., 2009, 2010; Li et al., 2013).

Sobrino et al. (2004) testaram a performance de 3 algoritmos para a aquisição da temperatura de superfície de tipos diferentes de solos e superfícies numa região da Espanha: a aplicação direta da equação de transferência radiativa, o algoritmo mono-janela de Qin et al. (2001) e o algoritmo de janela única de Jiménez-Muñoz e Sobrino (2003). Os autores mostraram que a aplicação direta da equação é bastante eficiente, porém são necessários valores de parâmetros atmosféricos derivados de medições *in situ*. Quando apenas dados de sensoriamento remoto estavam disponíveis, os autores encontraram valores médios de viés de -0,78°C e de REQM de 0,93°C para o algoritmo de Jiménez-Muñoz e Sobrino (2003), e de de viés de -2,09°C e de REQM de 2,15°C para o algoritmo de Qin et al. (2001).

O algoritmo do MODIS entra no grupo de algoritmos com várias bandas termais. Há dois produtos de temperatura de superfície disponibilizados pelo MODIS, o MOD11, que é o produto de LST, e o MOD28, que é o produto de temperatura superficial dos oceanos (SST, sigla para *sea surface temperature*). Apesar deste último ser um produto oceânico, ele está disponível para alguns lagos costeiros, e já foi utilizado em estudos de TSA (Reinart e Reinhold, 2008; Chavula et al., 2009). Estes produtos também usam algoritmos diferentes para calcular a temperatura, mas ambos usam o que é chamado de *split-window* (janela dividida), que usa informação das duas bandas termais para fazer a estimativa. Esses algoritmos usam a diferença de radiância que é medida por cada banda termal (com comprimentos de onda adjacentes) para fazer a estimativa da temperatura.

O MOD11 LST usa um algoritmo *split-window* linear, chamado de generalizado, desenvolvido por Wan e Dozier (1996) especificamente para o MODIS. Ele é baseado em uma relação linear entre as temperaturas de brilho nas bandas 31 e 32, e considera a diferença de emissividade em cada banda, que é um valor tabelado (Zhang, 1999) e calculado com base no uso de solo utilizando outras bandas (*e.g.,* vermelho e NIR), utilizando a equação:

$$\text{LST} = b_0 + \left(b_1 + b_2\frac{1-\bar{\varepsilon}}{\bar{\varepsilon}} + b_3\frac{\Delta\varepsilon}{\bar{\varepsilon}^2}\right)\frac{T_i + T_j}{2} + \left(b_4 + b_5\frac{1-\bar{\varepsilon}}{\bar{\varepsilon}} + b_6\frac{\Delta\varepsilon}{\bar{\varepsilon}^2}\right)\frac{T_i - T_j}{2} \tag{1.16}$$

em que T_i e T_j são as temperaturas de brilho, $\bar{\varepsilon}$ é a emissividade média das duas bandas, $\Delta\varepsilon$ é a diferença de emissividade entre as duas bandas, e b_n, $n = 0, 1, ..., 6$ são constantes, que são calibradas usando dados medidos de temperatura, e variam conforme a emissividade, o ângulo de visada do sensor, o vapor d'água atmosférico e a temperatura do ar (calculados no produto MOD07 de perfis atmosféricos do MODIS). Estes coeficientes estão em constante revisão e calibração pela equipe do MODIS (*e.g.* Hulley et al., 2011), de modo a melhorar a acurácia da estimativa da LST pelo produto MOD11, que é de cerca de 1°C (Wan e Dozier, 1996).

Já o produto MOD28 SST usa um algoritmo *split-window* não-linear (Kilpatrick et al., 2015), que é uma versão modificada do algoritmo *Non-linear SST* desenvolvido por Walton et al. (1998). Usando uma relação não-linear entre a temperatura de brilho e a temperatura de superfície, se reduzem os erros encontrados em dias quentes e quando há grande quantidade de vapor d'água na atmosfera (Li et al., 2013). Como a temperatura é derivada apenas para águas oceânicas, este algoritmo não depende da emissividade da superfície, mas apenas das temperaturas de brilho calculadas por cada banda e um valor *a priori* (uma primeira estimativa) da temperatura da superfície, e é dada por (Kilpatrick et al., 2015):

$$\text{SST} = c_1 + c_2 T_i + c_3 (T_i + T_j) T_{fg} + c_4 (\sec(\theta) - 1)(T_i - T_j) \tag{1.17}$$

em que θ é o ângulo zenital do satélite, T_{fg} é uma primeira estimativa da temperatura, para a qual é utilizado o valor do produto "blended" Reynolds semanal do NOAA/NCEP (Reynolds et al., 2007), e c_n, $n = 0, 1, ..., 4$ são constantes, que são calibradas usando valores de temperatura medidos em boias, e dependem do vapor d'água atmosférico, do mês do ano e da latitude.

1.2.5 Acurácia da estimativa da TSA por sensoriamento remoto

Vários estudos analisaram a acurácia da estimativa da TSA por sensoriamento remoto, geralmente focando em apenas um sensor. Está análise é feita por comparação direta entre a temperatura estimada e a temperatura medida. Assim, para lagos assume-se que a temperatura (medida na superfície) é constante dentro do pixel contendo o ponto de medição, e para rios é assumido mistura completa e que a temperatura é uniforme tanto transversalmente (a temperatura varia pouco, a não ser em rios muito grandes) quando num curto trecho longitudinalmente, que é utilizado para a estimativa da temperatura pelo sensor remoto. Os trabalhos que verificaram a acurácia da TSA usando os sensores MODIS ou Landsat em lagos se encontram na Tabela 1.2, e em rios, na Tabela 1.3. Observa-se que a literatura tratando de lagos é muito mais extensa do que a de rios. Isto se deve, provavelmente, ao tamanho dos pixels dos sensores em comparação com o tamanho da largura dos canais dos rios: não pode haver mistura entre água e solo para haver uma

correta estimativa apenas da temperatura da água do corpo hídrico. Por isso, a aplicação do sensor MODIS se limita a rios muito largos, havendo apenas uma tentativa de utilizá-lo no trabalho de Handcock et al. (2006); no caso do sensor Landsat 7 ETM+, sua banda termal possui 60 m de comprimento, e por isso sua aplicação também está limitada a rios mais volumosos. Por causa disso, há muitos estudos que fazem uso de sensores termais a bordo de aeronaves (como helicópteros ou drones), pois estes possuem uma resolução espacial (1 m ou superior) muito superior aos sensores a bordo de satélites, podem ser aplicados, então, a rios ou riachos bastante estreitos (*e.g.* Torgersen et al., 2001; Dugdale et al., 2018).

Nota-se que os erros na estimativa da TSA de lagos são da ordem de 1–1,5°C, enquanto que para rios estes valor é mais alto, podendo-se obter resultados mais acurados, em ambos os casos, utilizando dados de radiossonda e modelos de transferência radiativa. Além de questões como ruído e problemas na calibração do sensor, da emissividade e correção dos efeitos atmosféricos (Seção 1.2.4), outras limitações e fontes de erros dessa estimativas são a mistura subpixel e os efeitos de superfície.

Tabela 1.2 – Acurácia encontrada por estudos na estimativa da TSA de lagos.

Estudo	**Sensor**	**Lago**	**Métricas (°C)**	**Comentários**
Schneider e Mauser (1996)	Landsat 5 TM	Lago Constance, Alemanha: profundo, alpino e de porte médio	REQM de 0,73°C	aplicação da RTE com parâmetros atmosféricos derivados pelo Lowtran-7
Oesch et al. (2005)	AVHRR MOD28 SST	Três lagos alpinos na Suíça	viés de -0,13–2,67°C, σ de 0,6–2,56°C	teste de dois algoritmos diferentes; considerados apenas valores diurnos (Terra)
Wloczyk et al. (2006)	Landsat 7 ETM+	Lagos costeiros na Alemanha	REQM de 1,4°C	aplicação da RTE com dados de radiossonda e MODTRAN
Reinart e Reinhold (2008)	MOD28 SST	Dois lagos grandes na Suécia	viés de -0,65°C, erro absoluto de 0,41°C	comparação com dados *in situ* medidos abaixo da superfície
Crosman e Horel (2009)	MOD11 LST	Great Salt Lake, EUA	viés de -1,5°C, REQM de 1,63–1,73°C	dois pontos de medição; comparação com dados *in situ* medidos abaixo da superfície
Lamaro et al. (2013)	Landsat 7 ETM+	Reservatório Río Tercero, Argentina: pequeno e profundo	REQM de 1,23° REQM de 1,04°	aplicação do algoritmo de canal-único com dados de reanálise; aplicação da RTE com parâmetros do AtmCorr
Sima et al. (2013)	MOD11 LST	Lago Urmia, Irã: grande, raso e hipersalino	viés de -0,27°C, REQM de 2,26°C	possíveis erros nas medições de temperatura *in situ*; medições nem sempre na superfície do lago

Tabela 1.2 – Acurácia encontrada por estudos na estimativa da TSA de lagos.

Simon et al. (2014)	Landsat 7 ETM+	Dois reservatórios pequenos e profundos na França	viés de -0,47°C, REQM de 1,75°C	aplicação do algoritmo de canal-único com dados de reanálise; testes das diferentes bases de dados do algoritmo
Zhang et al. (2014)	MOD11 LST	Verificação no Lago Nam Co, Tibet: grande e profundo	viés de -1,4°C, REQM de 4,53°C	diferença entre o local de medição pelo sensor *in situ* e pelo sensor remoto
Liu et al. (2015)	MOD11 LST	Lago Taihu, China: grande e raso	REQM de 1,2–1,8°C	vários locais de amostragem no lago
Allan et al. (2016)	Landsat 7 ETM+	Vários lagos na Nova Zelândia	REQM de 0,48–0,94°C	aplicação da RTE com MODTRAN e diferentes fontes de dados atmosféricos
Pareeth et al. (2016)	MOD11 LST	Lago Garda, Itália: profundo, subalpino e de porte médio	REQM de 0,92–1,04°C	diversos sensores AVHRR e o MODIS Aqua também foram utilizados, mas apenas os resultados do MODIS Terra foram incluídos
Prats et al. (2018)	Landsats 5 e 7	Vários lagos na França	REQM de 1,2°C	aplicação do algoritmo de canal-único com dados de reanálise

Tabela 1.3 – Acurácia encontrada por estudos na estimativa da TSA de rios.

Estudo	**Sensor**	**Lago**	**Métricas (°C)**	**Comentários**
Kay et al. (2005)	ASTER Landsat 7 ETM+	3 rios nos EUA	sem cálculo de métricas erro médio próximo a 1°C	análise dos efeitos de correção atmosférica e da emissividade
Cherkauer et al. (2005)	ASTER	Mesmos rios de Kay et al. (2005)	viés de -1,1–15,2°C, σ de 0,1–3,7°C	resultados ruins para os rios com pixels mistos rio–solo, dada a resolução de 90 m do sensor
Handcock et al. (2006)	ASTER e Landsat 7 ETM+	Mesmos rios de Kay et al. (2005)	viés de 1,2°C, σ de 0,3°C ($>$ 3 pixels) viés de 2,2°C, σ de 0,4°C (1–3 pixels)	estudo relacionando a quantidade de pixels com a acurácia das estimativas
Wawrzyniak et al. (2012)	Landsat 7 ETM+	Rio Ródano, França	erro médio de $\pm$1,1°C, σ de 0,4°C (>3 pixels) erro médio de $\pm$1,4°C, σ de 0,5°C (1–3 pixels)	
Fricke e Baschek (2013)	Landsat 7 ETM+	Rio Reno, Alemanha	erro absoluto de 0,8°C σ de 1,0°C	
Fricke e Baschek (2015)	Landsat 7 ETM+	Rio Reno, Alemanha	viés de -1,09°C, σ de 0,49°C	

O primeiro afeta, geralmente, apenas imagens de rios, já que esta questão é em função da relação entre o tamanho do pixel e a largura do corpo d'água. Por isso, apenas os sensores Landsat, com a banda termal com resolução espacial de 60–120 m, e o ASTER, com bandas termais com 90 m, podem ser utilizados para imageamento de rios. Muitas vezes os pixels não são totalmente água, e sim uma mistura com outros materiais, como solo, vegetação e até mesmo rochas sobre a superfície da água. Como o calor específico e a inércia termal da água são bastante altos, geralmente bem maior do que a de outros materiais, a radiância medida pelo sensor (pela manhã, quando a água ainda está aquecendo ou resfriando, quando há passagem de frente fria) será uma mistura entre as duas temperaturas. Portanto, é essencial que estudos da TSA em rios utilizem apenas pixels "puros" contendo apenas água (assuin) (Kay et al., 2005). Isso foi ressaltado no trabalho de Cherkauer et al. (2005), no qual, utilizando o sensor ASTER, encontrou viés e σ de -1,1°C e 0,1°C, respectivamente, para o rio Columbia, bastante largo, mas valores de 4,6°C e 1,4°C para o rio Green, e de 15,2°C e 3,7°C para o rio Yakima, em trechos com largura comparável à resolução do sensor. Para o rio Yakima, mesmo o pixel com o menor erro, em um ponto mais largo do rio, obteve um erro de cerca de 7°C. Neste mesmo sentido, o trabalho de Handcock et al. (2006) mostrou que o ideal é que se tenha pelo menos três pixels na seção do rio para uma acurada estimativa da TSA. Portanto, para o Landsat 7 ETM+, a sua aplicação está limitada, segundo os autores, a rios com no mínimo 180 m de largura, isto ainda a depender da configuração dos pixels sobre o corpo d'água.

A segunda limitação é que a temperatura estimada por sensoriamento remoto é apenas da superfície da água (próximo dos 100 µm superiores, chamada de *"skin temperature"*, Handcock et al., 2012), e isso pode afetar a estimativa por causa de alguns efeitos que ocorrem na superfície, como o efeito de pele fria (do inglês *"cool-skin effect"*), também chamado de resfriamento evaporativo, causado pela formação de uma pequena camada limite por ação do vento e dos fluxos de calor, resultando na perda de calor pela evaporação da fina camada superior da água, e que pode deixar a temperatura da superfície até 0,5°C mais fria que a camada inferior (Robinson et al., 1984); o efeito de camada quente (do inglês *"warm-layer effect"*), em que ocorre o aquecimento preferencial da superfície da água, a até 1 m de profundidade, ocorrendo apenas em águas paradas ou em fluxo laminar, e que pode deixar a água até 5°C mais quente na superfície do corpo d'água (Schluessel et al., 1990); reflexão múltipla, radiação emitida e refletida por objetos próximos à superfície em direção ao sensor, aumentando a temperatura aparente da água (Kay et al., 2005); e a reflexão difusa, em que regiões em que a água é mais agitada refletem a luz de forma mais difusa, diminuindo a emissividade aparente da superfície e também aumentando a temperatura aparente da água (Dugdale, 2016). Além disso, a emissividade varia com a ângulo de visada do sensor, o que não é um problema para os sensores Landsat (os ângulos de visada são sempre pequenos), mas pode ser para o caso do MODIS (Masuda et al., 1988; Dugdale, 2016). Considerando estes fatores, a representatividade da

temperatura da água estimada para toda a camada depende da mistura do corpo d'água; em rios a estratificação térmica raramente ocorre por causa do seu fluxo turbulento, que mistura a camada e deixa uma temperatura mais uniforme verticalmente, mas pode ocorrer em rios mais profundos, principalmente em dias ensolarados (Torgersen et al., 2001; Kay et al., 2005). Em lagos, estes efeitos são bastante comuns; o efeito de camada quente ocorre apenas em lagos com estratificação térmica, comum a lagos profundos, enquanto que o efeito de pele fria geralmente ocorre, e sua intensidade depende principalmente da diferença de temperatura entre a água e o ar e da velocidade do vento (Fairall et al., 1996). Devido à longa história de métodos para estimativas da SST (Barton, 1995), métodos para remover o efeito de pele fria em águas oceânicas foram desenvolvidos (Schluessel et al., 1990). Contudo, para águas continentais, ainda há a necessidade da adaptação e aplicação destas técnicas para melhorar as estimativas da TSA. O trabalho de Prats et al. (2018) tentou adaptar um destes algoritmos para lagos, mas os autores concluíram que ainda é necessário um melhor desenvolvimento do mesmo para uma correta aplicação.

1.2.6 *Trade-off* entre a resolução espacial/temporal dos sensores remotos

A resolução espacial das imagens de sensoriamento remoto está intimamente relacionada com a resolução temporal dos mesmos: sensores com maior resolução espacial possuem menor resolução temporal, e vice-versa (Jensen, 2009). Enquanto para lagos da ordem de dezenas de km^2 ou maiores isso não é um problema, para rios apenas sensores com maior resolução espacial e, portanto, menor resolução temporal podem ser empregados. Para o uso como fonte de dados para calibração de modelos, utilizando o sensor Landsat e considerando que a estimativa da temperatura possa ser feita a partir de todas as imagens disponíveis para o corpo d'água (*i.e.* livre da cobertura de nuvens e outros erros, como saturação da banda), são gerados apenas cerca de 24 dados de temperatura da água por ano, o que pode refletir em um calibração ruim do modelo e, consequentemente, em uma série insuficiente de temperatura da água para o trecho de rio desejado.

Dada a limitação da resolução espacial de imageadores com maior frequência temporal, técnicas de *downscaling* de imagens são uma ferramenta que permite a combinação de imagens de diferentes sensores, com diferentes resoluções espaciais e temporais, desde que as radiâncias em suas bandas sejam comparáveis, de modo a se obter imagens com a melhor característica de cada sensor. Muitos algoritmos para *downscale* foram propostos na literatura (Wald, 2002; Mukherjee et al., 2014), mas poucos são voltados para aplicações em corpos d'água, e como mostrado por Mukherjee et al. (2014), a maioria depende de uma relação entre o NDVI e temperatura, relação esta que não é válida para a água.

Gao et al. (2006) introduziu uma técnica de fusão de imagens de satélite, o STARFM (sigla para *Spatial and Temporal Adaptive Reflectance Fusion Model*), para a fusão de imagens Landsat e MODIS, focando na reflectância da superfície. Este algoritmo propôs

combinar um ou dois pares de imagens do Landsat e do MODIS em dias distintos (um par em cada data) e uma imagem MODIS para cada dia entre os pares, para gerar imagens de reflectância de superfície com resolução temporal do MODIS e resolução espacial do Landsat, transformando os pixels das imagens MODIS (resolução de 250 m, 500 m ou 1000 m, dependendo do produto) para a mesma resolução dos pixels das imagens Landsat (30 m). Ele faz uma comparação pixel a pixel utilizando os pares de imagens e a imagem MODIS da data alvo (entre os pares) usando uma relação linear para estimar a reflectância da superfície para a data alvo, e em seguida aplicando o método para as demais datas. O algoritmo fez bastante sucesso, tendo diversas aplicações na literatura (e.g. Emelyanova et al., 2013; Swain e Sahoo, 2017) e sendo aprimorado diversas vezes. Zurita-Milla et al. (2008) aprimoraram a rotina para fazer o *downscale* utilizando também imagens do sensor MERIS (*Medium Resolution Imaging Spectrometer*). Hilker et al. (2009) desenvolveram a rotina STAARCH (sigla para *Spatial Temporal Adaptive Algorithm for mapping Reflectance Change*), baseada no STARFM, na qual o algoritmo adaptou o método para monitoramento da mudança de uso do solo, focando em áreas vegetadas que perderam a vegetação entre duas imagens Landsat. O algoritmo utiliza dois pares de imagens MODIS e Landsat, gerando o resultado a partir de mapas de classificação de uso do solo. Uma limitação de ambos modelos é que eles só conseguem predizer corretamente a reflectância da superfície dos pixels do MODIS quando estes são homogêneos, ou seja, quando os pixels do Landsat são homogêneos dentro um pixel da imagem grosseira (são todos de floresta, água ou agricultura, por exemplo). No caso dos pixels do MODIS compostos por misturas de tipos de uso do solo, há uma considerável perda da qualidade do *downscale*. Abordando este problema, Zhu et al. (2010) desenvolveram uma atualização do algoritmo, chamado de *Enhanced* STARFM (ESTARFM), focando em melhorar a acurácia do *downscale* para estes pixels. Segundo os autores, esta rotina usa elementos de teoria de "desmistura espectral", junto com a tendência da reflectância de um pixel entre dois pontos no tempo, para melhor estimar a reflectância em cada pixel do downscale da imagem do MODIS. Focando especificamente no *downscale* da temperatura de superfície, Weng et al. (2014) aprimoraram o algoritmo de Zhu et al. (2010), chamado de SADFAT (*Spatio-temporal Adaptive Data Fusion Algorithm for Temperature mapping*), focando o processo na radiância, em vez da reflectância da superfície, incluindo uma componente termal na conversão dos pixels grosseiros para pixels finos. Assim, o SADFAT é um dos poucos algoritmos de fusão de imagens com foco na temperatura que não consideram diretamente o NDVI para a aplicação, apesar deste índice depender apenas das bandas do vermelho e NIR, que também são imagens de entrado no SADFAT. A Figura 1.5 demonstra o potencial destes algoritmos em fazer a fusão de imagens para aumentar a resolução espacial das imagens MODIS.

Com a aplicação do SADFAT, aliando imagens Landsat 7 ETM+ e MODIS, é possível se gerar uma série de temperatura da água com dados diários, o que resulta,

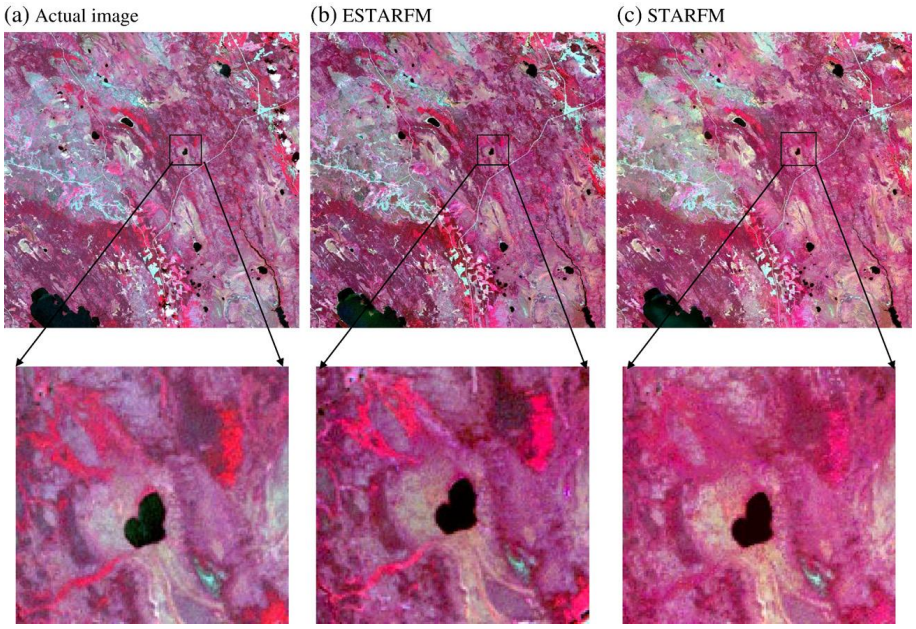

Figura 1.5 – Comparação de (a) uma imagem composta NIR-verde-azul do Landsat 7 ETM+ com as resultantes do downscale da imagem MODIS na mesma data utilizando (b) o ESTARFM e (c) o STARFM. (Fonte: Zhu et al., 2010)

teoricamente, numa melhor calibração do modelos de temperatura da água dos rios estudados. Entretanto, não há aplicações deste algoritmo para este fim na literatura, e algumas limitações devem ser contornadas, como o possível grande número de falhas tanto do Landsat como do MODIS, com o fato de ser um *downscale* a nível de pixel (e não de cenas, como geralmente é feito em aplicações do algoritmo), e a grande diferença da inércia termal e do calor específico entre a água e o solo, considerando que os rios estão em pixels MODIS não-homogêneos, fatores estes não levados em consideração na conversão linear do pixel grosseiro para a resolução fina.

1.3 Justificativa

Dada a escassez de dados de campo de temperatura da água, tanto espacialmente quanto temporalmente, se faz necessário o uso de outras técnicas para se estimar esta variável, como o sensoriamento remoto. Apesar de alguns estudos já terem feito análises da acurácia das estimativas da temperatura da água de lagos, ainda há incerteza quanto aos métodos que podem ser aplicados para as imagens Landsat, e também de como estas estimativas comparam com as do MODIS, por exemplo, já que este sensor possui maior resolução radiométrica (Barnes et al., 1998) e possui algoritmos próprios desenvolvidos pela equipe MODIS (Wan e Dozier, 1996). Para rios, esta incerteza é ainda maior, devido à escassez de estudos na área, reflexo principalmente da resolução espacial do sensor.

Além disso, há poucos trabalhos tratando da calibração de modelos da temperatura de rios utilizando apenas temperatura estimada por sensoriamento remoto, algo já notado

na literatura por Handcock et al. (2012) e Dugdale et al. (2017). Com a mudança climática afetando e tendendo a afetar ainda mais a temperatura de lagos e rios (van Vliet et al., 2013; O'Reilly et al., 2015), se faz necessária uma ferramenta de análise do padrão temporal deste parâmetro em rios que não possuem dados medidos, e também para servirem de dados de entrada na modelagem ecológica de lagos.

1.4 Questões científicas

- Qual é a acurácia, a precisão e os principais fatores influenciando nos erros das estimativas da temperatura superficial da água de lagos usando diferentes produtos de sensoriamento remoto?
- Para imagens Landsat, quais as diferenças entre os métodos utilizados para as estimativas da temperatura da água de lagos e rios?
- Quais são os principais parâmetros que podem ser trabalhados para melhorar as estimativas da temperatura da água por sensoriamento remoto?
- Qual a acurácia e a precisão da técnica de *downscaling* SADFAT na estimativa da temperatura da água de rios?
- É possível calibrar modelos de temperatura da água de rios utilizando apenas dados de temperatura da água derivados de sensoriamento remoto para se gerar séries consistentes de temperatura?

1.5 Objetivo

O objetivo deste trabalho é validar métodos de estimativa da temperatura superficial da água de lagos e rios por sensoriamento remoto e avaliar a performance de modelos de temperatura da água de rios calibrados com estes dados.

1.6 Organização do trabalho

Para responder estas questões científicas, os estudos foram desenvolvidos e apresentados nos capítulos 2 e 3, na forma de artigos:

- Capítulo 2:

  Comparison of methods to estimate lake-surface-water temperature using Landsat 7 ETM+ and MODIS imagery: Case study of a large shallow subtropical lake in Southern Brazil. Water, 11(1):168, 2019.

Validação de produtos de sensoriamento remoto na Lagoa Mangueira.

- Capítulo 3:

  Validation of river water temperature models calibrated using satellite-derived river water temperature – An approach using Landsat 7 ETM+ and MODIS imagery. Artigo a ser submetido.

  Validação de produtos de sensoriamento remoto e calibração de modelos de temperatura no rio White, nos EUA.

A Figura 1.6 mostra a organização dos capítulos da dissertação, seus principais temas e a relação entre eles.

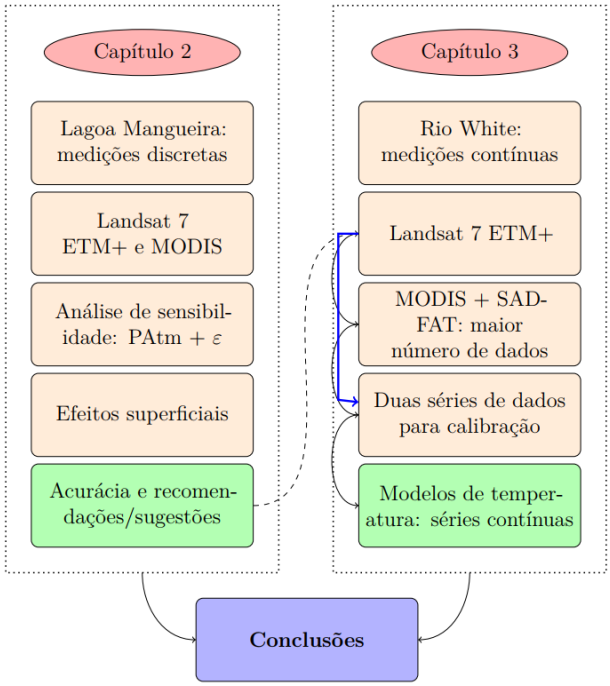

Figura 1.6 – Organização dos capítulos da dissertação.

No Capítulo 2 foi estudada a acurácia da estimativa da temperatura superficial de um lago, a Lagoa Mangueira, utilizando os sensores Landsat 7 ETM+, este com aplicação de diferentes métodos, e MODIS, utilizando seus produtos MOD11 (de temperatura continental) e MOD28 (de temperatura oceânica). Além disso, foram analisadas a sensibilidade da acurácia a duas variáveis, a emissividade e os parâmetros atmosféricos, e os principais fatores limitantes destas estimativas.

No Capítulo 3 foi analisada a consistência de séries contínuas da temperatura do rio White geradas por dois modelos de temperatura de rios, o *air2stream* e um modelo estocástico (este em três versões diferentes), calibradas com dados derivados dos sensores Landsat 7 ETM+ e MODIS, este após o uso de uma técnica de *downscale*. Além da consistência da série final, foi também avaliada a acurácia dos dados de temperatura gerados por cada um dos sensores utilizados, e verificadas as limitações de cada passo.

Capítulo 2

A comparison of methods to estimate lake surface water temperature using Landsat 7 ETM+ and MODIS imagery: Case study of a large shallow subtropical lake in Southern Brazil

Matheus Henrique Tavares
Augusto Hugo Farias da Cunha
David da Motta Marques
Anderson Ruhoff
J. Rafael Cavalcanti
Carlos Ruberto Fragoso Jr.
Juan Martín Bravo
Andrés Mauricio Munar
Fernando Mainardi Fan
Lucia Helena Ribeiro Rodrigues

Artigo publicado no periódico "Water", fator de impacto (ISI): 2.069, Qualis CAPES: Engenharias I – A2. DOI: https://doi.org/10.3390/w11010168

A comparison of methods to estimate lake surface water temperature using Landsat 7 ETM+ and MODIS imagery: Case study of a large shallow subtropical lake in Southern Brazil

Matheus Henrique Tavares[a,*], Augusto Hugo Farias Cunha[a], David da Motta-Marques[a], Anderson Luís Ruhoff[a], J. Rafael Cavalcanti[a], Carlos Ruberto Fragoso Jr[b], Juan Martín Bravo[a], Andrés Mauricio Munar[c], Fernando Mainardi Fan[a], Lucia Helena Ribeiro Rodrigues[a]

[a]*Instituto de Pesquisas Hidráulicas Universidade Federal do Rio Grande do Sul, 91501-970, Porto Alegre, Rio Grande do Sul, Brazil*
[b]*Centro de Tecnologia, Universidade Federal de Alagoas, 57072-970, Maceió, Alagoas, Brazil*
[c]*Escuela de Ciencias Agrícolas, Pecuarias y del Medio Ambiente, Universidad Nacional Abierta y a Distancia, 111411, Bogotá, Colombia*

Abstract

Water temperature regulates many processes in lakes; therefore, evaluating it is essential to understand its ecological status and functioning, and to comprehend the impact of climate change. Although few studies assessed the accuracy of individual sensors in estimating lake-surface-water temperature (LSWT), comparative analysis considering different sensors is still needed. This study evaluated the performance of two thermal sensors, MODIS and Landsat 7 ETM+, and used Landsat methods to estimate the SWT of a large subtropical lake. MODIS products MOD11 LST and MOD28 SST were used for comparison. For the Landsat images, the radiative transfer equation (RTE), using NASA's Atmospheric Correction Parameter Calculator (AtmCorr) parameters, was compared with the single-channel algorithm in different approaches. Our results showed that MOD11 obtained the highest accuracy (RMSE of 1.05 °C), and is the recommended product for LSWT studies. For Landsat-derived SWT, AtmCorr obtained the highest accuracy (RMSE of 1.07 °C) and is the recommended method for small lakes. Sensitivity analysis showed that Landsat-derived LSWT using the RTE is very sensitive to atmospheric parameters and emissivity. A discussion of the main error sources was conducted. We recommend that similar tests be applied for Landsat imagery on different lakes, further studies on algorithms to correct the cool-skin effect in inland waters, and tests of different emissivity values to verify if it can compensate for this effect, in an effort to improve the accuracy of these estimates.

Keywords: Water-surface temperature, lakes, remote sensing, thermal infrared, Landsat, MODIS

1. Introduction

Water temperature regulates many physical, chemical, and biological processes in lakes and reservoirs, such as reaction and metabolic rates, species distribution, nutrient cycling, and the concentration of dissolved gases (Horne and Goldman, 1994). Therefore, evaluating water temperature in lakes is essential to understanding their function and ecological status. In addition, lakes are considered sentinels of climate change due to their sensitivity to the environment (Adrian et al., 2009), and lake-surface-water temperature (LSWT) is a proxy to analyse water-quality conditions and the impact of climate change on these systems (O'Reilly et al., 2015; Yang et al., 2018). A conventional way to assess LSWT is by using in situ sensors to measure temperatures at specific monitoring stations within a system. However, this approach requires the appropriate infrastructure and field work to install and maintain the sensors, which is expensive and time consuming. Moreover, for large aquatic ecosystems, this approach demands an extensive monitoring network to adequately measure the LSWT due to the spatiotemporal heterogeneity of these systems (Kay et al., 2005; Crosman and Horel, 2009). Unfortunately, technical and financial resources are not always available for such monitoring.

*Corresponding Author.
Email address: tavaresmatheush@gmail.com (Matheus Henrique Tavares)

Data from satellite sensors may provide better information on LSWT variability than conventional field monitoring, since most modern sensors have improved capabilities with respect to spectral (e.g., spectral range of the thermal infrared), radiometric, temporal, and spatial resolutions (Kay et al., 2005; Handcock et al., 2006). Although satellite-derived water temperature is a description of the LSWT only in the top layer (i.e., approximately the upper 100 μm, called "skin temperature"), it may provide important information about the patterns of water-temperature variations in lakes, and has been used in many studies, such as analysis of temperature patterns and heat budget (Alcântara et al., 2010; Curtarelli et al., 2013), spatial distribution of water-quality variables (Yang et al., 2018), evaporation estimation (Sima et al., 2013), LSWT spatial gradients (Crosman and Horel, 2009; Liu et al., 2015; Allan et al., 2016; Ling et al., 2017), LSWT temporal-variation patterns (Pareeth et al., 2016; Prats et al., 2018), and the assessment of the impact of El Niño/La Niña events (Luz et al., 2017) and climate change (Schneider and Hook, 2010; O'Reilly et al., 2015; Woolway and Merchant, 2018) on lakes.

Thermal infrared (TIR) bands are usually employed to retrieve accurate estimations of LSWT from satellite sensors, which are available only from a restricted number of these sensors. Two widely used thermal sensors for retrieving surface temperature (ST) are the Moderate Resolution Imaging Spectroradiometer (MODIS), aboard the Terra and Aqua satellites, and Thematic Mapper (TM), Enhanced Thematic Mapper Plus (ETM+) and Thermal Infrared Sensor (TIRS), aboard Landsat missions 4 to 8 (e.g. Jiménez-Muñoz and Sobrino, 2003; Handcock et al., 2006; Li et al., 2013; Weng et al., 2014). Landsat sensors have a temporal resolution of 16 days, and a spatial resolution of 30 m, with the exception of their thermal bands, which have a spatial resolution of 60–120 m. MODIS thermal bands (31 and 32) have a spatial resolution of 1000 m and a daily overpass; however, its products have a resolution of 1–9 km (Kilpatrick et al., 2015). The Terra and Landsat satellites have an identical orbit, with about 15 min between overpass times, which makes their sensor measurements comparable. For lakes and reservoirs, these sensors can be used for monitoring SWT, depending on the size of the water body as well as the purpose of the study (e.g. Reinart and Reinhold, 2008; Lamaro et al., 2013). Besides spatial and temporal resolution, radiometric precision differs among these sensors: MODIS TIR bands have a noise-equivalent change in temperature (NEΔT) of 0.05 °C at 27 °C (Barnes et al., 1998), while Landsat 7 ETM+ thermal band has a NEΔT of 0.22 °C at 7 °C (Barsi et al., 2003b).

Most LSWT studies have evaluated the accuracy of individual sensors (Gholizadeh et al., 2016), such as MODIS (e.g. Reinart and Reinhold, 2008; Crosman and Horel, 2009; Sima et al., 2013; Luz et al., 2017) and Landsat (e.g. Schneider and Mauser, 1996; Lamaro et al., 2013; Allan et al., 2016), indicating the limitations of each sensor, namely, the spatial/temporal resolution trade-off, different Landsat methodologies, and sensor accuracy. Therefore, comparative analysis considering different sensors to estimate LSWT is still needed and may reveal important differences and limitations in the application of each sensor and direct studies (Ruiz-Verdú et al., 2016). Furthermore, while MODIS has SWT products that can be directly downloaded and used in these studies, for Landsat imagery, the SWT needs to be derived by the user, and it can be done using a few available methods (Li et al., 2013). Moreover, as noted by Allan et al. (2016), these methods still have to be further validated using ground measurements, especially in the Southern Hemisphere. Additionally, few studies discuss the sensitivity of these methods to their input variables, such as water emissivity and atmospheric water vapour content, which can significantly impact the result (Jiménez-Muñoz and Sobrino, 2006; Jiménez-Muñoz et al., 2010; Hulley et al., 2011; Yu et al., 2014). Since few studies have assessed these methods (Lamaro et al., 2013; Fricke and Baschek, 2013; Simon et al., 2014; Allan et al., 2016) from different perspectives, it is also important to test and compare these multiple methods of temperature estimates.

This study evaluated the performance of two thermal sensors, MODIS and Landsat 7 ETM+, and Landsat methods to estimate the SWT of a large subtropical lake in Southern Brazil.

2. Materials and Methods

2.1. Study Area and Field Measurements

The study subject is Lake Mangueira, a large shallow subtropical lake located in the coast of Rio Grande do Sul, close to the Brazil–Uruguay border. It has a surface area of 820 km^2 and is elongated, with a length of 90 km and width of 3–10 km, mean depth of 2.6 m, and maximum depth of 6.9 m. Its trophic state ranges from oligotrophic to mesotrophic (Fragoso Jr et al., 2011; Crossetti et al., 2013). The local climate is subtropical (Cfa type in Köppen's climate classification) (Kottek et al., 2006), with a mean annual temperature of 16 °C and annual precipitation of 1800–2200 mm. The water-temperature time series was measured over 18 years, between 2001 and 2018, at the

water surface at three stations across Lake Mangueira, namely, TAMAN (Northern), TAMAC (Central), and TAMAS (Southern), as shown in Figure 1. All measurements were made during the morning, and temperature was considered steady during this time of day (i.e., there was no variation in time between temperature measurements and satellite overpass at around 10:30 a.m. local time), as there is little diel variation in temperature (around 0.5 °C between morning and night) in large lakes (Woolway et al., 2016).

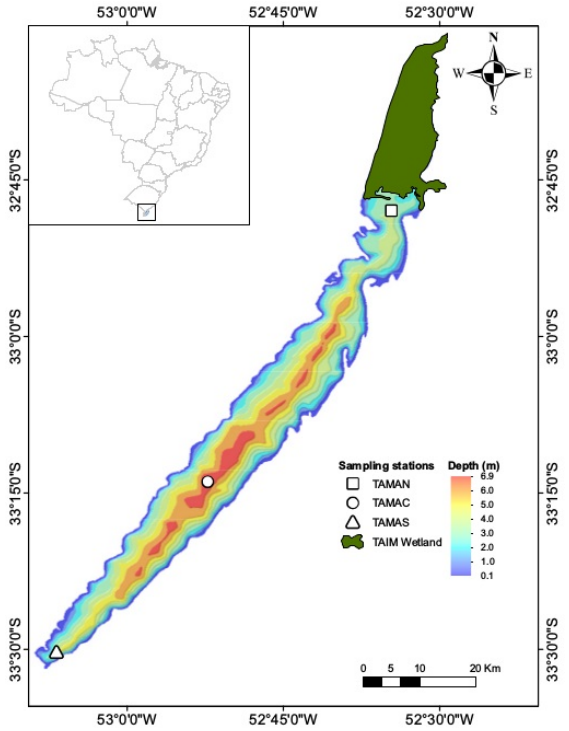

Figure 1: Map of Lake Mangueira, showing the three stations, Northern (TAMAN), Central (TAMAC) and Southern (TAMAS). (Source: Munar (2017)).

To compare the water-temperature estimates, one Landsat sensor and two MODIS products were used. Landsat 7 ETM+ was chosen over other Landsat sensors because it has a time series that covers the entire period of the measured data, providing more matching dates of observed temperatures and satellite images, whereas the Landsat 5 mission ended in 2011, and Landsat 8 OLI was launched in 2013, resulting in fewer suitable images from these two sensors. In the case of MODIS, both MOD11 and MOD28, which have been used in previous studies of LSWT (e.g. Reinart and Reinhold, 2008; Chavula et al., 2009; Alcântara et al., 2010; Sima et al., 2013; Zhang et al., 2014; Luz et al., 2017), are available for Lake Mangueira, and are described in the following sections.

Landsat 7 ETM+ and MODIS images were selected in order to compare the estimated LSWT with the measured data. Cloud cover is of major concern in SWT estimation using the TIR bands, since water vapour both absorbs and emits radiance in this spectrum (Jiménez-Muñoz and Sobrino, 2003), limiting the SWT estimation to cloudfree pixels. Since the Landsat images coincided with water-temperature measurements on only a few days (cloud cover substantially reduced the number of available dates), in order to increase the available data, in this study we used a window of two days of difference between the measurement and the satellite image, as in large lakes the water temperature varies only slightly over this period of time (Lamaro et al., 2013; Cavalcanti et al., 2016). When Landsat images were from a different date than the measurement, MODIS images from the same Landsat date were also used when possible, to better compare them. The dates used in this study, with the availability of images for each sensor and station, are shown in Table S1.

In total, 26 dates were used, spread over all seasons, with 68 in situ temperature measurements (considering that, in some field campaigns, water temperature was not measured at all three monitoring stations). Altogether, considering

all three stations, there were 58 Landsat 7 ETM+ estimations, 46 MOD28 estimations, and 64 MOD11 estimations. In order to assess the performance of each method and sensor, we used bias, absolute error, root mean squared error (RMSE), and the correlation coefficient (r^2). A statistical procedure was done in order to verify the assumption of normality (Shapiro–Wilk test) and equal variance (Bartlett's test) of the residuals (difference between the calculated and measured temperatures), as well as to assess whether the performance of the methods was statistically different (ANOVA followed by Tukey's honestly significant difference test).

The procedure used in this work followed the flowchart in Figure 2. The following sections detail the methods used for each sensor.

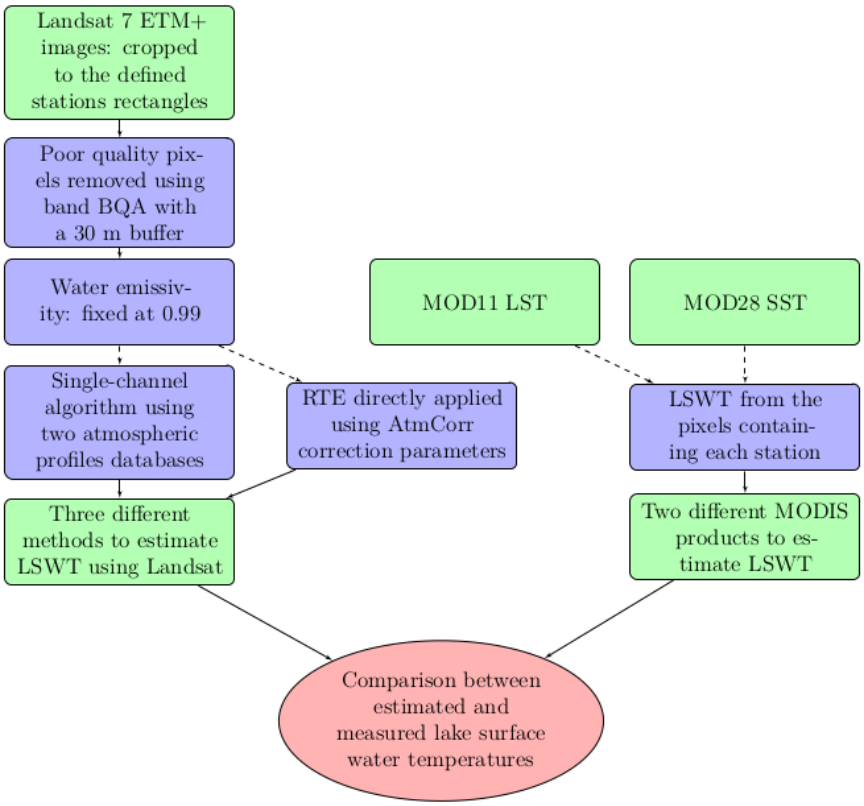

Figure 2: Flowchart illustrating the procedure used to estimate lake-surface-water temperature (LSWT) using Landsat 7 ETM+ and MODIS imagery to compare with measured data.

2.2. MODIS Products

MODIS has two products of surface temperature available for download: MOD28, which is a product of sea-surface temperature (SST), and MOD11, which is a product of land-surface temperature (LST). In the case of the coastal Lake Mangueira, both products are available. MOD28 is available with two different spatial resolutions, 4 and 9 km, and based on two different spectra, the TIR (~ 11–12 μm) and the MWIR (~ 3.5–4.1 μm) spectra (Kilpatrick et al., 2015). For comparison with Landsat images, for which temperature estimates were made based on the TIR band, and because SST derived from the MWIR are only for night time, only MODIS TIR products were used.

MODIS has two thermal bands, band 31, with wavelengths in the range of 10.78–11.28 μm, and band 32, in the range of 11.77–12.27 μm. For the estimation of the ST, both products use a split-window algorithm, which bases the correction of the atmospheric effects on the variation of the radiance measured by each TIR band, although they have differences, which are briefly described next.

2.2.1. MOD11 LST

The MOD11 LST product uses other bands (e.g., red, NIR) to determine land cover, and the ST is derived using generalised split-window algorithm of Wan and Dozier (1996) for pixels with known emissivity, which is the case with water. It considers the difference of emissivity between bands 31 and 32, along with constants calibrated for the sensor, to estimate the ST. The main issue with its LSWT estimation is the assumption that emissivity is constant for water, whereas it varies with many components of water, such as salinity, for example, which can result in errors of 0.2–0.5 °C (Friedman, 1969; Hulley et al., 2011).

MOD11A1 LST images are daily and have a spatial resolution of 1 km, and are available directly via NASA's LAADS DAAC page or on demand (available on `https://ladsweb.modaps.eosdis.nasa.gov/search/`), where users can select the products, and the images can be reprojected to the desired projection/UTM zone. MODIS Collection 6 LST products for the dates shown in Table S1 were downloaded, and the ST was extracted for each date and for each station using ArcGIS 10.3.

2.2.2. MOD28 SST

MOD28 SST is derived using a split-window algorithm, which is a modified version of the nonlinear split-window algorithm of Walton et al. (1998). It depends on brightness temperatures calculated by each thermal band and an a priori (first-approximation) estimate of the ST, and uses empirical coefficients for each month of the year, derived from in situ buoy and satellite observations and different atmospheric profiles based on latitude. The main issues with to the SST estimate and its application to lakes, besides its coarse spatial resolution, are the effect of wind on the relationship between skin and subsurface temperatures, and the fact that it was designed for sea water, so emissivity can be slightly overestimated. For more information on MOD28 characteristics, please refer to Kilpatrick et al. (2015).

MOD28 SST is available directly via NASA's PODAAC/JPL FTP (available on `ftp://podaac-ftp.jpl.nasa.gov/OceanTemperature/modis/L3/terra/11um/v2014.0/4km/daily/`). As was done with MOD11, the SST products for the dates shown in Table S1 were downloaded, and the ST was extracted for each date and for each station using ArcGIS 10.3.

2.3. Landsat 7 ETM+ Images

2.3.1. Methods to Estimate LSWT

While MODIS has specific products of ST, with standard algorithms designed and applied by the MODIS team (e.g. Wan and Dozier, 1996), the user needs to estimate the ST from Landsat images, using the radiative transfer equation (RTE) or algorithms developed for this purpose (Li et al., 2013).

The radiance measured by sensors aboard satellites is different from that leaving the surface, since the atmosphere, mainly water vapour, both absorbs and emits radiance in this spectrum (Jiménez-Muñoz et al., 2010). For a precise estimate of the ST, it is necessary to remove these atmospheric effects considering three atmospheric parameters: atmospheric transmittance (τ), and the emitted (L^{up}) and absorbed (L^{down}) radiance. Their relationship to the radiance measured by the sensor is described by the radiative transfer equation, given by (Schott, 2007):

$$L_{\text{sensor}} = [\varepsilon B + (1 - \varepsilon)L^{\text{down}}]\tau + L^{\text{up}} \quad (1)$$

where L_{sensor} is the top-of-atmosphere (TOA) radiance measured by the sensor, ε is the surface emissivity, and B is the spectral radiance emitted by a black body with temperature T.

While MODIS has two thermal bands and its own algorithm to correct for these effects, Landsat TM and ETM+ sensors have only one thermal band, which makes this correction using its own band measurements unfeasible (Barsi et al., 2003b; Li et al., 2013). These correction parameters must be derived from additional data provided from other sources, and are most accurately calculated using radiative transfer codes, with in situ radiosonde data and weather models to provide the input data for the atmospheric profiles (Jiménez-Muñoz et al., 2010; Allan et al., 2016). When no local atmospheric data are available to apply this equation, as is the case of most lake applications, algorithms can be used. For sensors with a single thermal band, Jiménez-Muñoz and Sobrino (2003) developed a single-channel algorithm to estimate surface temperatures, focusing on Landsat 5 TM, replacing the atmospheric parameters by functions of the total columnar atmospheric water vapour content and then adjusting second-degree polynomials to it, considering a number of atmospheric profiles and using the MODTRAN radiative transfer code. Jiménez-Muñoz et al. (2009)

updated the algorithm to include Landsat 4 TM and Landsat 7 ETM+. In their algorithm, surface temperature is given by:

$$\mathrm{ST} = \gamma[\varepsilon^{-1}(\psi_1 L_{\mathrm{sensor}} + \psi_2) + \psi_3 - L_{\mathrm{sensor}}] + T_{\mathrm{sensor}} \tag{2}$$

where T_{sensor} is the brightness temperature, ψ_1, ψ_2, and ψ_3 are atmospheric functions, and γ is a function calculated by:

$$\gamma = \left[\frac{c_2 L_{\mathrm{sensor}}}{T_{\mathrm{sensor}}^2}\left(\frac{\lambda_{\mathrm{eff}}^4}{c_1} L_{\mathrm{sensor}} + \lambda_{\mathrm{eff}}^{-1}\right)\right]^{-1} \tag{3}$$

where $c_1 = 1.191 \times 10^8\ \mathrm{W\mu m^4/m^2 sr}$ and $c_2 = 1.439 \times 10^4\ \mathrm{K\mu m}$ are the Planck's constants, and λ_{eff} is the effective wavelength of the thermal band, which is 11.269 μm for Landsat 7 ETM+ (Cristóbal et al., 2009). The atmospheric functions are related to atmospheric parameters as:

$$\begin{aligned} \psi_1 &= \frac{1}{\tau} \\ \psi_2 &= -L^{\mathrm{down}} - \frac{L^{\mathrm{up}}}{\tau} \\ \psi_3 &= L^{\mathrm{down}} \end{aligned} \tag{4}$$

and calculated by:

$$\psi_n = c_n w^2 + b_n w + a_n \tag{5}$$

where $n = 1, 2, 3$; w is the atmospheric water vapour content, and a, b, and c are constants given by Jiménez-Muñoz et al. (2009), according to the chosen atmospheric profile database. In this study, we used two databases: SAFREE, which is a compilation of maritime profiles, and thus should be useful for coastal zones; and TIGR3, which has a wide range of atmospheric profiles, and showed better results in our preliminary tests.

For the atmospheric water vapour content, we used the MODIS product MOD07L2, which is daily and has a spatial resolution of 5 km, considering that this parameter does not have a large spatial variability in comparison to its spatial resolution; thus, it could be used here (Jiménez-Muñoz et al., 2010; Díaz-Delgado et al., 2010), and because it showed good results in the study of atmospheric parameter sources by Jiménez-Muñoz et al. (2010).

However, as these constants are generalised for a number of atmospheric profiles, it is expected that estimates are not quite precise, especially when atmospheric water vapour content is high (Jiménez-Muñoz and Sobrino, 2003). Because of this, in this study we also used NASA's Atmospheric Correction Parameter Calculator (AtmCorr) (Barsi et al., 2003a, 2005), a freely available online platform (available on `https://atmcorr.gsfc.nasa.gov/`) that provides these parameters by applying MODTRAN 4.0 to atmospheric profiles modeled by the National Centers for Environmental Prediction (NCEP/NOAA), generated every 6 h for each node of meridians and parallels ($1^\circ \times 1^\circ$ grid), interpolating the terms of atmospheric correction for Landsat thermal band for the time, date and location desired. With these data, the radiance measured by the thermal band can be corrected from the atmospheric effects (L_{corr}), and the estimated ST is given by brightness temperature. At-sensor radiance was corrected using the following equation (Schott, 2007):

$$L_{\mathrm{corr}} = \frac{L_{\mathrm{sensor}} - L^{\mathrm{up}} - \tau L^{\mathrm{down}}(1 - \varepsilon)}{\varepsilon\tau} \tag{6}$$

Emissivity strongly influences the estimated temperatures but, as it is difficult to estimate (Sobrino and Raissouni, 2000), a fixed value is commonly employed (e.g. Schneider and Mauser, 1996; Lamaro et al., 2013; Prats et al., 2018). Here, water emissivity was fixed at 0.99, as was done in Díaz-Delgado et al. (2010), Okwen et al. (2011), and Deng and Wu (2013), for example, and found in MODIS emissivity product MOD11 (0.992 for band 31 and 0.988 for band 32) for Lake Mangueira. Emissivity is discussed further in Section 2.4.

Altogether, three different methods were used to estimate Lake Mangueira's SWT using Landsat 7 ETM+ images. The nomenclature for each method is described in Table 1.

2.3.2. Processing Landsat Images

Only Landsat 7 ETM+ T1 images (Tier 1 images, the highest-quality data available, with geometric and radiometric correction) were used. We used the radiance measured by Landsat 7 $B6_2$ (*high gain*) thermal band, which had higher

Table 1: Nomenclature of the methods used for the estimation of LSWT using Landsat 7 ETM+ imagery.

Method	Description
AtmCorr	Radiative transfer equation applied with atmospheric correction parameters from AtmCorr
SC-SAFREE	Single-channel algorithm using SAFREE database and MOD07L2's water vapour
SC-TIGR	Single-channel algorithm using TIGR3 database and MOD07L2's water vapour

radiometric precision than $B6_1$ (*low gain*), although it worked in a narrower temperature range (Chander et al., 2009). First, images were cropped to a polygon of 1 × 1 km around each station, in order to provide more pixels for the estimation, given the limiting factor of cloud cover in the region and the known gaps in the images due to a malfunction of the satellite's scan-line corrector. Low-quality pixels (due to cloud cover and shading, for example) were removed using the pixel quality band (BQA) with a 30 m buffer around them. Then, the DN (Digital Number) values in the image were transformed into spectral radiance (in W/m^2 sr μm), using values in the metadata file, and then to brightness temperature, in K, by inverting Planck's law, according to Chander et al. (2009):

$$T = \frac{K2}{\ln\left(\frac{K1}{L_{\text{sensor}}} + 1\right)} \tag{7}$$

where K1 and K2 are calibration constants, and for Landsat 7 ETM+ they are 666.09 W/(m^2 sr μm) and 1282.71 K, respectively.

The LSWT was then calculated for each Landsat image and for each polygon; then, the calculated temperature for each station was assumed to be the mean temperature of the pixels in each polygon. The algorithm for all these processes was written in *R* (R Core Team, 2017), with the help of packages *maptools* (Bivand and Lewin-Koh, 2017), *sp* (Pebesma and Bivand, 2005), *raster* (Hijmans, 2017), *rgdal* (Bivand et al., 2017), and *rgeos* (Bivand and Rundel, 2017).

2.4. Sensitivity Analysis

Besides the spatial, spectral, and radiometric resolution of sensors, the accuracy of the temperature estimate depends mainly on two variables: the emissivity and the atmospheric-correction parameters (Schneider and Mauser, 1996; Jiménez-Muñoz and Sobrino, 2006). Therefore, an assessment of the sensitivity of the temperature estimates to these variables can improve the understanding of the errors resulting from remote sensing-derived temperatures (Mao et al., 2005; Yu et al., 2014). Because in MODIS products they are calculated using internal algorithms developed by the MODIS team, we only analyzed the sensitivity of the estimates for Landsat images.

2.4.1. Emissivity

Emissivity is difficult to estimate from remote-sensing data. A few methods to estimate surface emissivity have been developed (Sobrino et al., 2004, 2008; Li et al., 2013), most of them fixing values for different land covers. MOD11, for example, provides a product of surface emissivity for each of its thermal bands, and uses fixed values of emissivity for water, which depend on the characteristics of the water-surface images in the red and NIR bands. Water emissivity varies with temperature and dissolved materials, for example, but in the TIR region, it approaches a blackbody (Handcock et al., 2012). A range of emissivity values has been used in the literature (e.g., 0.9925 in Schneider and Mauser, 1996 and 0.98 in Wloczyk et al., 2006), but the most common values are 0.9885 (Lamaro et al., 2013; Simon et al., 2014; Prats et al., 2018), which is the mean of the mean water-emissivity values for MODIS bands 31 and 32 (Snyder et al., 1998), and 0.99 (Díaz-Delgado et al., 2010; Okwen et al., 2011; Deng and Wu, 2013), which is an approximate value derived by Masuda et al. (1988) for distilled water for a range of wavelength and sensor viewing angles.

For sensitivity analysis, we estimated the LSWT using the RTE with AtmCorr parameters, varying emissivity from 0.97 to 1.0 by increments of 0.005.

2.4.2. Atmospheric-Correction Parameters

There are a few sources of atmospheric parameters that can be used when no local data are available. Jiménez-Muñoz et al. (2010) compared three different sources of atmospheric profiles, AtmCorr, MOD07L2, and MAPRI (developed by the authors from Reanalysis products from the NCEP), with local radiosonde data for ST estimation. In their study, however, the authors used only one Landsat 5 TM image, limiting its conclusions. The authors found errors of up to 3.5% for τ and up to 20% for L^{up} and L^{down} when using MOD07L2 for ASTER thermal bands, and 8% for τ and 30% for L^{up} and L^{down} when using AtmCorr, and 10% for τ and 60% for L^{up} and L^{down} when using MAPRI for the Landsat 5 TM thermal band. Coll et al. (2012) ran a similar analysis, finding RMSE of 0.9, 1.0, and 1.1 K when using MOD07, AtmCorr, and radiosonde data, respectively.

For sensitivity analysis, we only used the RTE with the atmospheric parameters given by AtmCorr. The Reanalysis product was not used due to its coarse spatial resolution ($2.5° \times 2.5°$). Since the results calculated by Jiménez-Muñoz et al. (2010) were only for a single date, and are therefore difficult to extrapolate, here we considered a variation of -5% to $+5\%$ with increments of 2.5% for τ and -10% to $+10\%$ with increments of 5% for L^{up} and L^{down}, which are more realistic in terms of the variations of these parameters. Although the variation was consistent for all parameters, that is, all parameters varied positively or negatively, we note that, as atmospheric water vapour increases, τ tends to decrease (the atmosphere interacts more with the radiance emitted and reflected by the surface) and L^{up} and L^{down} tend to increase (the atmosphere both emits and absorbs more radiance), which we would expect to compensate each other.

We also assessed the sensitivity of the single-channel algorithm to atmospheric water vapour content. Since AtmCorr also provides an estimation of atmospheric water vapour content, it was compared with MOD07L2. As it has been reported, the algorithm is not very sensitive to the water vapour content (according to Prats et al., 2018, a 50% decrease in the value of w produced a decrease in the estimated temperature of 0.2–0.3 °C), we varied the water vapour from -50% to $+50\%$ to assess its sensitivity.

3. Results

3.1. Temperature Pattern in the Lake

The largest temperature difference between the three stations (Figure 3) was observed on 15 March 2013 (day 74), during late summer, when the temperature at the Central station was 21.79 °C, and at the Southern station was 18.83 °C. However, most of the time, the difference in temperature between the three stations was ≤ 1.5°C.

The lake shows a clear seasonal pattern, with temperatures in the range of 20–25 °C during summer, and reaching less than 8 °C during winter. The Central and Southern stations showed the lowest temperatures in almost the same number of measurements each, while the Northern station showed the highest temperatures in most measurements, as previously reported (Fragoso Jr et al., 2011; Crossetti et al., 2013).

3.2. Estimated Temperatures

All three methods using Landsat images showed good performance (Figure 5), with most estimates within a window of +2 °C/−3 °C of the measured temperatures. In most cases, LSWT was underestimated, which is supported by the negative bias found for all methods (Table 2). As ANOVA showed significant statistical difference between all methods, we also ran Tukey's post hoc test to pairwise analyse the differences between the methods (Table 3). AtmCorr estimated LSWT with the highest accuracy, showing the best values for all calculated metrics, with values of RMSE and r^2 of 1.07 °C and 0.964, respectively. Among the estimates using the single-channel algorithm, the TIGR3 database functioned better than SAFREE for this region, reducing absolute error and RMSE by around 0.2 °C, and bias by almost 0.5 °C, although no significant statistical difference between the two methods was found (p-value = 0.198, Table 3). Tukey's post hoc test also showed that AtmCorr and TIGR3 residuals (Figure 4) had no significant statistical difference (p-value = 0.967).

Both MODIS products also showed good performance (Figure 5), but MOD11 performed better than MOD28, with values of RMSE and r^2 of 1.05 °C and 0.962, respectively (Table 2), and statistically similar to the residual results found for AtmCorr (Table 3). Despite showing the smallest bias (in terms of magnitude) among all estimators, MOD28 showed higher inconsistencies, in some cases overestimating the temperatures by more than 3 °C (Figure 4), with a significant statistical difference of residuals from all methods (Table 3). It also consistently overestimated temperatures,

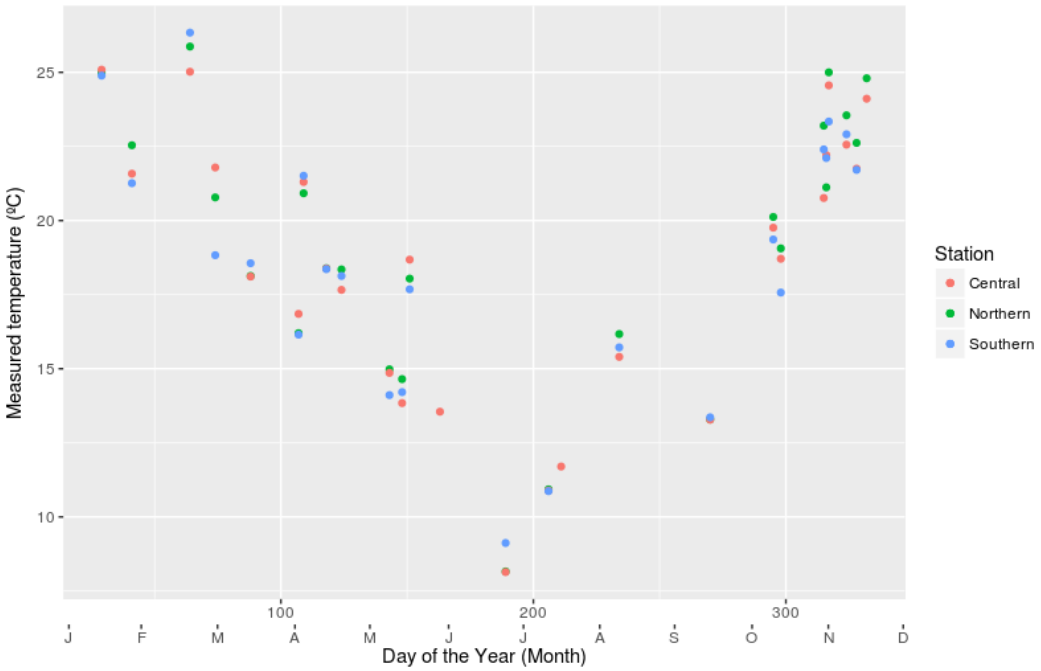

Figure 3: Measured temperatures in the three stations across Lake Mangueira from 2001 to 2018, plotted according to the day of the year. Summer starts on day 356 and ends on day 80, and winter starts on day 173 and ends on day 266.

Table 2: Metrics calculated for each method of estimating Lake Mangueira's SWT using Landsat 7 ETM+ imagery and MODIS products.

Method	**Absolute error (ºC)**	**Bias (ºC)**	**RMSE (ºC)**	r^2
AtmCorr	0.880	-0.465	1.07	0.964
SC-SAFREE	1.19	-0.990	1.50	0.936
SC-TIGR	1.00	-0.560	1.32	0.938
MOD11	0.825	-0.523	1.05	0.962
MOD28	0.989	0.329	1.25	0.906

with a positive bias of 0.329 °C, which was not found for the other estimators. This is also reflected in the low values of the correlation coefficients between the MOD28 and Landsat methods (Table 4).

The accuracy of the estimates using Landsat images is directly affected by atmospheric water vapour content (Figure 6), as seen in the regression lines (Table 5), while MODIS estimations do not seem to follow this pattern (p-value > 0.05).

3.3. Sensitivity Analysis

Sensitivity analysis (Figure 7) showed that, for emissivity, there is a considerable variation in error (Table 6), with RMSE values varying by almost 12% for emissivities in the 0.97–0.99 range. Bias and the absolute maximum error showed an almost linear increase, with minimum values found for emissivities of 0.975 and 0.980, respectively. In the case of the atmospheric-correction parameters, the temperature was very sensitive to changes (when applying the radiative transfer equation): even a small change of 5% in these parameters (2.5% for atmospheric transmissivity) increased the RMSE and the maximum error by 2 °C (Table 7). The increases in errors were sharper when the values of the atmospheric parameters are decreased.

On the other hand, the single-channel algorithm is only slightly sensitive to the atmospheric parameters (simplified as atmospheric water vapour content). The algorithm showed a very similar performance when using MOD07L2 or AtmCorr as the source of water vapour (Table 8), despite the significant changes in the values given by each source,

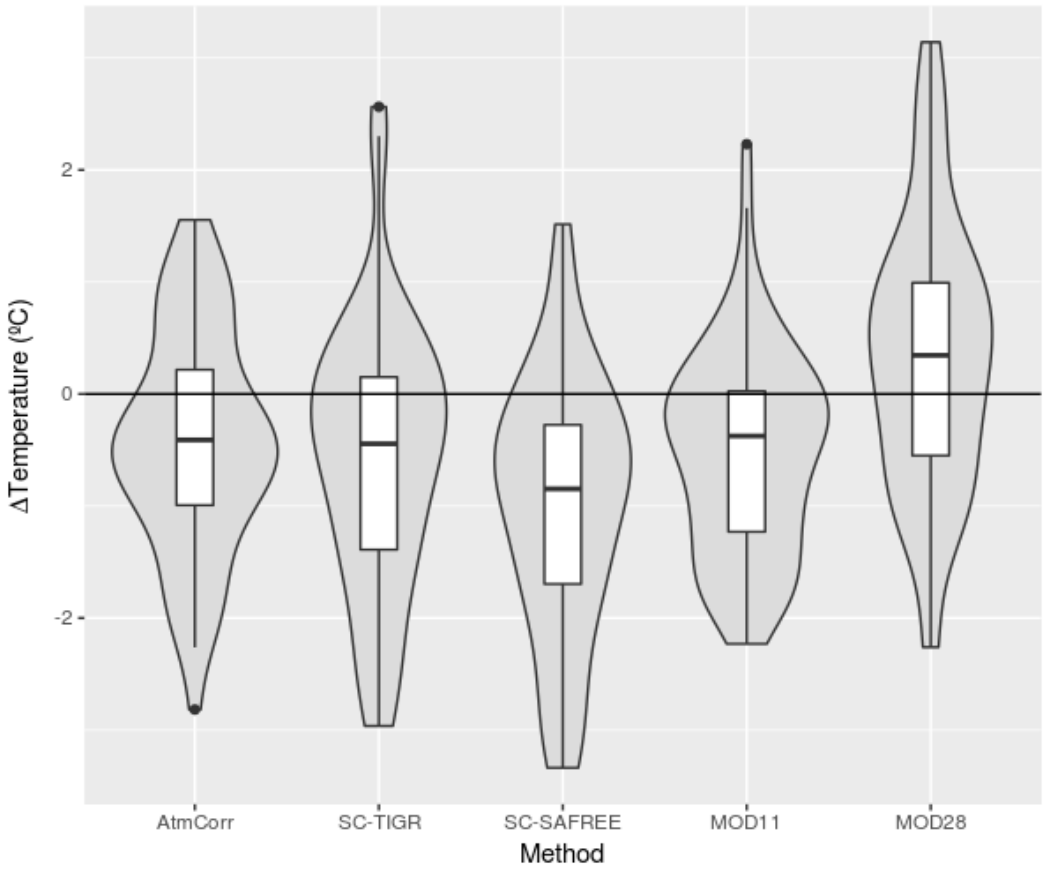

Figure 4: Boxplot and violin plot of the residuals between the temperatures estimated by each method and the measured temperatures.

with values of RMSE of 0.39 g/cm^2 (23.5%), maximum difference of −1.26 g/cm^2 (64%), and r^2 of 0.675. An even more pronounced difference in water vapour content, increasing or decreasing its value by 50%, showed a variation in the results considerably smaller than in the case of the radiative transfer equation, considering its order of magnitude. The same pattern was observed when varying AtmCorr's water vapour content by −50% and +50%, with quite similar values of bias, RMSE, and maximum absolute error.

4. Discussion

4.1. Comparison of Landsat 7 ETM+ and MODIS Performance

When using TIGR3 database constants, AtmCorr and the single-channel algorithm both showed good performance (with no statistical difference between their residual data), corroborating with similar studies found in the literature (Lamaro et al., 2013; Yu et al., 2014; Prats et al., 2018). TIGR3 outperforming SAFREE (Table 3) for coastal-lake SWT estimation was previously reported (Simon et al., 2014), suggesting that the SAFREE database should not be used in such studies.

The main limiting factor for LSWT estimates using Landsat imagery is the correction of the atmospheric effects. Using commercial radiative transfer codes to estimate these parameters and applying the RTE, Schneider and Mauser (1996) found an RMSE of 0.73 °C when applying Lowtran with Landsat 5 images, and Allan et al. (2016) found an RMSE between 0.48 °C and 0.94 °C when applying MODTRAN with Landsat 7 ETM+. These studies showed how specific, more accurate atmospheric-correction parameters can improve LSWT estimation. While AtmCorr is the best alternative (to the authors' knowledge) for freely obtaining these parameters, it provides only a point estimate,

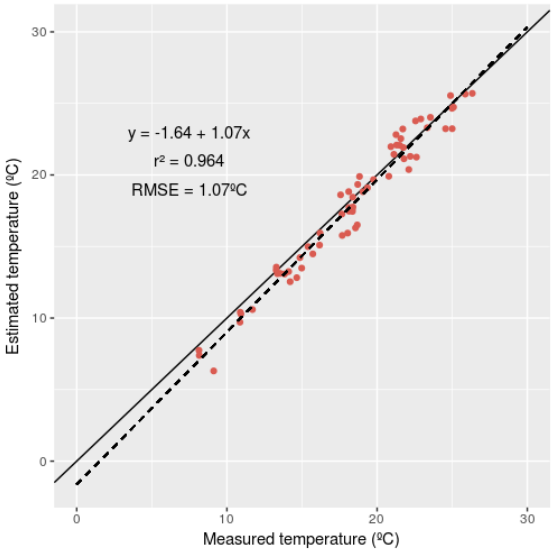

(a) AtmCorr

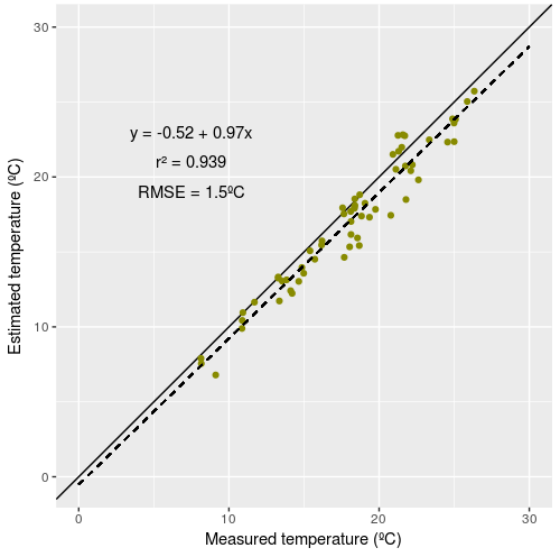

(b) SC-SAFREE

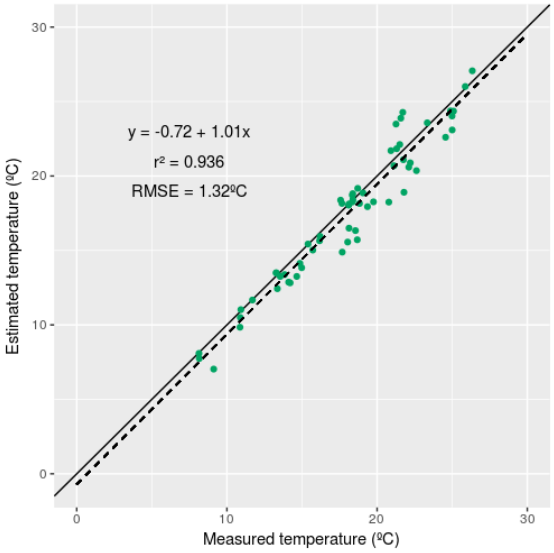

(c) SC-TIGR

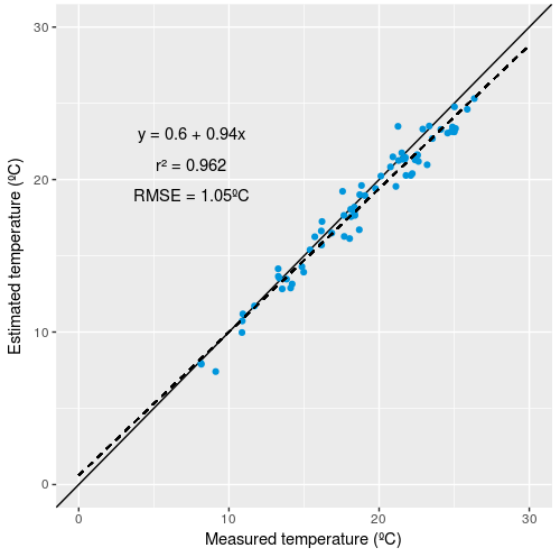

(d) MOD11

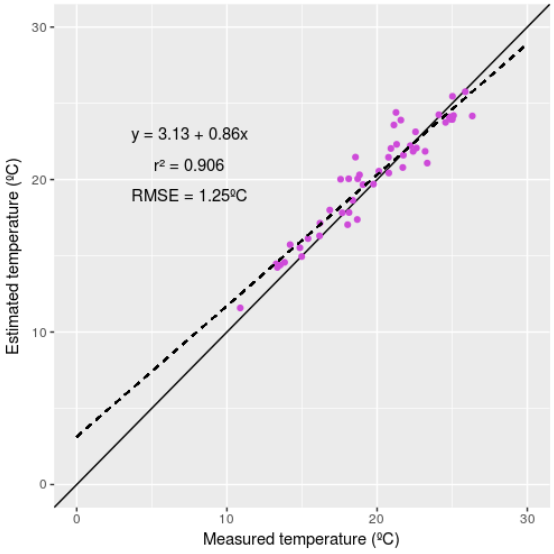

(e) MOD28

Figure 5: Comparison of the LSWT estimated by each product/method with in situ measured temperatures.

Table 3: p-value of the Tukey's test between the residuals of each method.

Method	**AtmCorr**	**SC-TIGR**	**SC-SAFREE**	**MOD11**	**MOD28**
AtmCorr	NA	0.967	<0.05	0.990	<0.05
SC-TIGR	0.967	NA	0.198	0.999	<0.05
SC-SAFREE	<0.05	0.198	NA	0.113	<0.05
MOD11	0.990	0.999	0.113	NA	<0.05
MOD28	<0.05	<0.05	<0.05	<0.05	NA

Table 4: Correlation coefficient between the residuals of each method.

Method	**AtmCorr**	**SC-TIGR**	**SC-SAFREE**	**MOD11**	**MOD28**
AtmCorr	NA	0.768	0.730	0.606	0.355
SC-TIGR	0.768	NA	0.962	0.670	0.324
SC-SAFREE	0.730	0.962	NA	0.704	0.425
MOD11	0.670	0.606	0.496	NA	0.644
MOD28	0.324	0.355	0.425	0.644	NA

which is interpolated from the closest nodes of parallels and meridians ($1^\circ \times 1^\circ$ grid). For large lakes, this can be a problem when estimating the temperature for its whole surface and, considering the operational limitation of AtmCorr, MOD07L2 may be the best option when using Landsat imagery in these cases, since it provides water vapour content with spatial variability. The main issue with the estimates using MOD07L2 with the single-channel algorithm in our study is the lower accuracy in some SWT estimates, reaching out to a ΔT of $\pm$ 3 °C in some cases. Many of these low-quality estimates are consistent with the results found by Jiménez-Muñoz et al. (2009), in which the error of the ST estimates increased considerably for atmospheric water vapour content higher than 3.0 g/cm^2 (Figure 6).

The performance found for MODIS also compared well with the literature, with both products showing performance similar to what was found in most studies (Chavula et al., 2009; Crosman and Horel, 2009; Sima et al., 2013; Liu et al., 2015; Pareeth et al., 2016). Reinart and Reinhold (2008) used MOD28 to estimate the LSWT of two large lakes in Sweden, and found a mean absolute difference and r^2 of 0.41 °C and 0.993 for both lakes, respectively. In spite of the good performance found by the authors, LSWT estimates were compared with measured bulk temperatures, and so this may not be the case for the ST, since many of the data were from the summer months, when both lakes may have been thermally stratified.

Our findings showed higher similarity between LSWT estimations based on MOD11, AtmCorr, and SC-TIGR, different from LSWT estimations based on MOD28. Despite the similar performance shown by MOD28 and SC-TIGR (in terms of absolute error and RMSE), MOD28 showed more erratic behaviour, with a smaller correlation coefficient and different linear regression (Figure 5). Besides that, MOD28 showed a positive bias, while all other estimators showed a negative bias. Additionally, good agreement between the estimates using Landsat and MOD11 (Tables 3 and 4) indicates that they are consistent estimators over this lake, while MOD28 is not, as there is a high correlation between the residuals for the Landsat methods and MOD11, but not between the former and MOD28. Even though high correlation was found between MOD11 and MOD28, it may be due to the fact that both MODIS products similarly overestimated small-to-medium temperatures and underestimated higher temperatures (despite MOD28 showing a positive bias), which was not observed in the Landsat estimates.

The lower performance obtained for MOD28 may be explained by its low spatial resolution of 4 km, which might be too coarse for Lake Mangueira due to its narrowness (5 km wide over the Northern station, and less than 4 km wide over the Southern station). In fact, errors in the estimates were considerably higher for the Southern station than for the Central and Northern stations, pointing to this. Considering that temperature varies more widely near the shores (Crosman and Horel, 2009; Alcântara et al., 2010; Lamaro et al., 2013), it can be inferred that this product is not recommended for applications to lakes with narrow widths (in comparison to its spatial resolution), as is the case for Lake Mangueira.

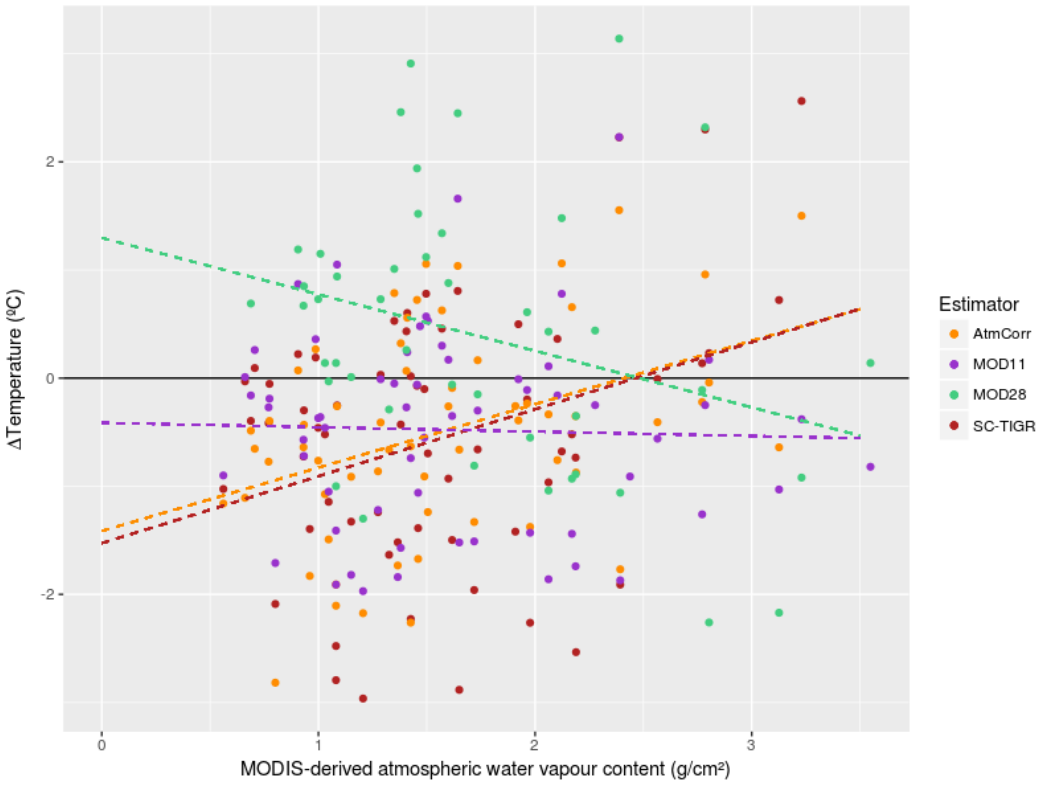

Figure 6: Comparison of the residuals found for estimations using Landsat 7 ETM+ and MODIS with atmospheric water vapour content estimated by MOD07L2. The dashed lines represent the linear regression between ΔT and w for each method (values are in Table 5).

Table 5: p-value of the linear regression between the residuals and w for each method.

Method	**Slope**	**Intercept**	***p*-value**
AtmCorr	0.587	-1.41	<0.01
SC-TIGR	0.620	-1.53	<0.01
MOD11	-0.041	-0.413	0.813
MOD28	-0.522	1.30	0.0513

4.2. Sensitivity to Parameters and Source of Errors

As seen in the literature, error in lake-water temperatures derived from remote-sensing imagery can occur mainly due to poor correction of atmospheric effects (Harris and Mason, 1992; Jiménez-Muñoz and Sobrino, 2006), water-surface effects (Robinson et al., 1984), and due to the misrepresentation of water emissivity (Friedman, 1969; Jiménez-Muñoz and Sobrino, 2006).

There is difficulty associated with estimating and removing atmospheric effects, which can promote substantial errors (Jiménez-Muñoz et al., 2010; Coll et al., 2012). In fact, estimates tend to have lower accuracy when the water vapour content in the atmosphere is higher, since this increases the uncertainty regarding the effect of the atmosphere on the radiance measured by the sensor and, thus, in the correction parameters. Jiménez-Muñoz et al. (2009) showed that the error in ST estimates considerably increased for atmospheric water vapour content higher than 3.0 g/cm^2. Here, Landsat-derived estimates using AtmCorr showed a similar (although less pronounced) pattern. As atmospheric water vapour content (from the MOD07L2 water vapour product) increases, so does the error in the estimates of both SC-TIGR and AtmCorr, although this is not the case for MOD11 and MOD28 (Figure 6, Table 5). Although in other studies the accuracy of MODIS products decreased with higher temperatures (e.g. Liu et al., 2015), which is related to higher water vapour content, this was not evident here (p-value > 0.05 for both products, Table 5). This may be due to

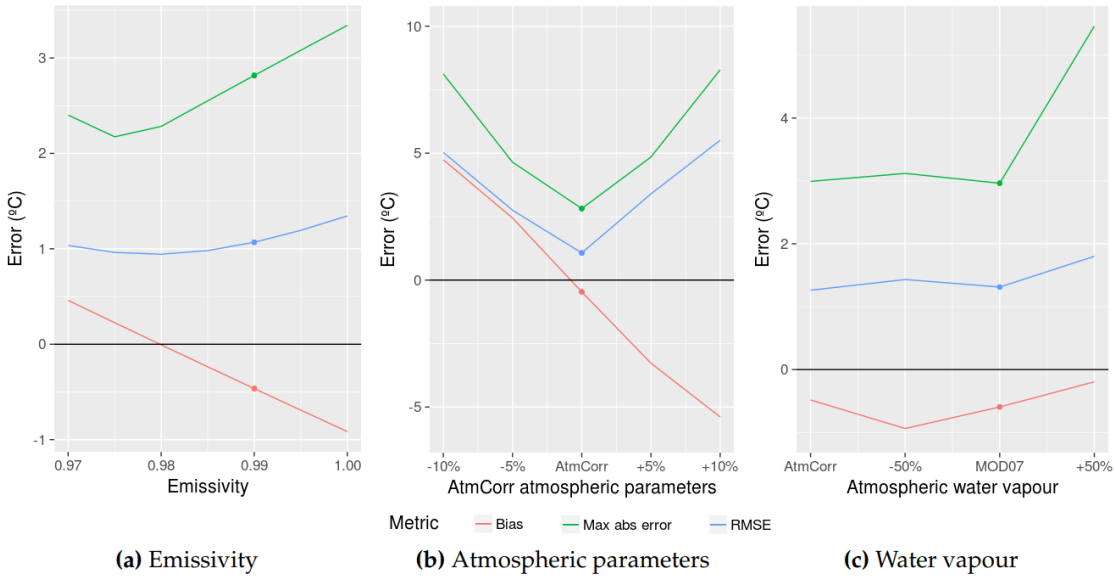

Figure 7: Sensitivity analysis of the estimated LSWT to (**a**) emissivity, (**b**) atmospheric parameters, and (**c**) water vapour content, showing the resulting bias, absolute maximum error, and RMSE when varying them, for (**a**) from 0.97 to 1.0, for (**b**) from −10% to +10% (−5% to +5% for atmospheric transmissivity), and for (**c**) from −50% to +50%, taking MOD07L2 as reference. The dots represent the values employed in this work.

Table 6: Metrics calculated for the analysis of sensitivity of the temperatures estimates to emissivity.

Emissivity	**Bias (ºC)**	**RMSE (ºC)**	**Maximum error (ºC)**	r^2
1.00	-0.916	1.34	-3.34	0.965
0.995	-0.691	1.19	-3.08	0.965
0.990*	-0.465	1.07	-2.82	0.965
0.985	-0.237	0.981	-2.55	0.965
0.980	-0.0068	0.943	-2.28	0.965
0.975	0.225	0.962	2.17	0.965
0.970	0.459	1.04	2.40	0.965

*value of emissivity used in this study

the refined quality of the MODIS algorithm to remove these effects using its own band measurements (Jiménez-Muñoz et al., 2010), and to directly apply it in its ST products.

Temperature estimates using the RTE are very sensitive to atmospheric parameters (Figure 7), particularly to atmospheric transmissivity. For instance, a small change of 2.5% in atmospheric-transmissivity value implied an increase of about 2 °C in the RMSE. The increase in errors is more pronounced when decreasing the values of the atmospheric parameters, showing that τ (which decreases as atmospheric water vapour increases) has a more important effect on L_{corr} than L^{up} and L^{down} (both increase as atmospheric water vapour increases), which is expected considering Equation (6). In this case, negative bias also contributes to this sharp increase in errors, as it increased in magnitude when the atmospheric parameters negatively varied. This result highlights the importance of an accurate, precise source of estimation of the influence of the atmosphere on the radiance measured by the sensor, as has been shown in the literature by good results in estimation of LSWT when using in situ radiosonde data and radiative transfer models (e.g. Allan et al., 2016).

The single-channel algorithm is much less sensitive to changes in atmospheric parameters, i.e., atmospheric water vapour content. Prats et al. (2018) reported that a 50% decrease in water vapour content produced a decrease of 0.2–0.3 °C in the estimated temperatures; in our sensitivity analysis, this decrease produced a (negative) increase of 0.3 °C in

Table 7: Metrics calculated for the analysis of sensitivity of the temperatures estimates to the atmospheric parameters.

Atmospheric parameters	**Bias (°C)**	**RMSE (°C)**	**Maximum error (°C)**	r^2
AtmCorr	-0.465	1.07	-2.82	0.965
-10%	-5.39	5.51	-8.28	0.960
-5%	-3.27	3.40	-4.85	0.945
+5%	2.44	2.75	4.64	0.963
+10%	4.74	5.03	8.12	0.957

Table 8: Metrics calculated for the analysis of sensitivity of the temperatures estimates to the atmospheric water vapour content.

Water vapour source	**Bias (°C)**	**RMSE (°C)**	**Maximum error (°C)**	r^2
AtmCorr	-0.483	1.26	-2.82	0.944
MOD07L2*	-0.594	1.31	-2.99	0.938
MOD07L2 -50%	-0.937	1.43	-3.12	0.944
MOD07L2 +50%	-0.195	1.80	5.46	0.912

*source of water vapour content used in this study

the bias, and only marginally increased the RMSE (0.07 °C). On the other hand, for increased w values, the RMSE and maximum error increased by 0.5 °C and 1 °C, respectively, which is consistent with the report of Jiménez-Muñoz et al. (2009). Considering the small size (in comparison to emissivity and the radiance measured by the sensor) of the contribution of the water vapour content to the temperature estimates in this algorithm, MOD07L2 can be used for retrievals of LSWT using Landsat images, since data are measured daily and are spatially distributed, and this product is ready to use.

In our study, only a few estimates were made when water vapour content was high (>3 g/cm^2, Figure 6), which limits further understanding of the performance of these methods under such conditions. However, as seen in these few estimates and in the literature (e.g. Jiménez-Muñoz et al., 2009; Liu et al., 2015), studies estimating LSWT in areas with high atmospheric water vapour, such as tropical areas, should keep in mind that estimation is bound to produce higher errors, especially when using Landsat imagery (Table 8). For the Landsat methods, other sources of atmospheric parameters, such as reanalysis products (Jiménez-Muñoz et al., 2010; Prats et al., 2018), should also be further studied in order to be used with the radiative transfer equation in an effort to increase the accuracy of the estimates.

The cool bias found in our study was also found in most LSWT studies (e.g. Crosman and Horel, 2009; MacCallum and Merchant, 2012; Sima et al., 2013; Liu et al., 2015; Prats et al., 2018). This can be a result of the cool-skin-layer effect, when the few millimetres at the top of the water column are colder than the water underneath. Usually, this is not measured by in situ sensors but affects estimates made using remote sensing (Schluessel et al., 1990). The cool-skin-layer effect reduces water temperature over a range of 0.1–0.6 °C, occurring as a result of heat loss from water to air due to evaporation, and is affected mainly by wind speed (Robinson et al., 1984; Fairall et al., 1996). A warm-layer effect can also be observed during calm sunny days in deeper lakes, where thermal stratification can occur, and can increase the ST up to several degrees (Ward, 2006), but as observed here and in other studies (e.g. Fragoso Jr et al., 2011), this is not the case for the shallow Lake Mangueira.

While this effect is different for each lake and depends on in situ lake-temperature measurements to be understood, techniques are available to address the cool-skin-layer effect in sea water, which assume this to be a function of wind speed (Fairall et al., 1996). Although we did not attempt to assess and remove the cool-skin-layer effect in the estimations here, our study shows that it is important in LSWT studies using remote sensing. Prats et al. (2018) estimated the LSWT for French water bodies for a long time series using Landsat 5 TM and 7 ETM+ images, applying an adjusted sea-water algorithm to remove the effects of the cool-skin-layer and warm-layer effects, and testing these approaches on a reservoir with in situ data to validate it. The estimated cool-skin-layer effect reduced the LSWT by about 0.3 to 0.6 °C for most of the data, and even though the authors concluded that the algorithm required further adaptations for use on continental waters, it demonstrated how techniques to remove these effects can be useful to improve the accuracy of remote sensing-derived SWT in lake studies.

In the case of emissivity, considering that MODIS products use a fixed value of emissivity for water, as was also used in our study for Landsat 7 ETM+ images (as well as in most studies of water-temperature estimations using remote sensing, e.g. Lamaro et al., 2013; Prats et al., 2018), it can also be a source of considerable error. Emissivity varies with several parameters, such as salinity and turbidity, which can result in errors of estimation ranging from 0.2 to 0.5 °C (Friedman, 1969). Hulley et al. (2011) used an algorithm to improve the estimation of water emissivity and the coefficients for the split-window algorithm for MOD11, in order to improve its estimation of inland SWT. They found differences of emissivity in up to 0.01 for MODIS, which resulted in errors of 0.3–0.7 °C.

As shown in the sensitivity analysis, emissivity has a significant impact on the estimated temperatures, and showed an optimal value of 0.98, reducing the RMSE and maximum absolute error by 10% and 20%, respectively, compared to our standard value of 0.99. This, however, can be a result of the balancing of the cool-skin-layer effect: as the latter reduces water temperature at the surface, a lower value of emissivity (i.e., further from its physical, more-likely value) makes the surface appear warmer than it is, partially compensating for the cool-skin effect. Although this 0.98 emissivity value produced the best results, we assumed (taking into account that it was not measured) that the closest value, from 0.97 to 1, to its real value is 0.99, which was calculated by Masuda et al. (1988) and also found in MODIS product MOD11 (0.992 for band 31 and 0.988 for band 32) for Lake Mangueira. Due to the limitation of water-emissivity estimation (Handcock et al., 2012), most approaches still use a fixed, tabulated value of emissivity, found in reflectivity and emissivity data available in spectral libraries such as MODIS' (Zhang, 1999). As emissivity and the removal of the cool-skin-layer effect are limiting factors to be improved in LSWT estimations, the use of lower emissivity values can be tested in future studies to reduce errors resulting from the latter in an effort to improve the accuracy of LSWT estimates.

5. Conclusions

In this study, we compared different methods for estimating lake-surface-water temperatures using Landsat 7 ETM+ and MODIS products. Considering the results from our study and the literature, MOD11 is the recommended product to be used in LSWT studies due to its accuracy (values of bias, RMSE, and r^2 of −0.523 °C, 1.05 °C and 0.962, respectively), temporal resolution, and ease of use, and should be preferred over MOD28, which gave less accurate results. Landsat 7 ETM+ should be used in small lakes, due to its higher spatial resolution, and we recommend the application of the radiative transfer equation with atmospheric-correction parameters when possible. Despite its high sensitivity to these parameters, as shown in our work, which can result in gross errors in temperature estimates, this equation was successfully applied in Lake Mangueira with AtmCorr, and showed quite similar performance to MOD11 (values of bias, RMSE, and r^2 of −0.465 °C, 1.07 °C, and 0.964, respectively). The limitations of this application are difficulties in operating this platform, and that it only provides correction parameters for a point (i.e., it is not spatially distributed). Although not as accurate, the single-channel algorithm can also be used with Landsat imagery using the TIGR3 database, and most sources of atmospheric water vapour content, since it is not very sensitive to this parameter. We recommend MOD07L2 to be used with this algorithm, because the data are measured daily and spatially distributed, and it is ready to use. However, users should take into account that the accuracy of this algorithm is considerably reduced in cases when atmospheric water vapour content is high.

We recommend that similar tests be done for Landsat imagery (especially on RTE sensitivity to different sources of atmospheric parameters) on other lakes with different geographical and morphological characteristics to support our findings. We also recommend the further development and adaptation of techniques to assess and remove the cool-skin-layer effect in SWT estimations in inland waters to reduce the cool bias seen in most studies on this subject, and tests of different emissivity values, to verify if they can compensate, to some degree, for the cool-skin effect, in an effort to improve the accuracy of these estimates.

6. References

Adrian, R., O'Reilly, C. M., Zagarese, H., Baines, S. B., Hessen, D. O., Keller, W., Livingstone, D. M., Sommaruga, R., Straile, D., Donk, E. V., Weyhenmeyer, G. A., and Winderl, M. (2009). Lakes as sentinels of climate change. Lymnology and Oceanography, 54(6):2283–2297.

Alcântara, E. H., Stech, J. L., Lorenzzetti, J. A., Bonnet, M. P., Casamitjana, X., Assireu, A. T., and de Moraes Novo, E. M. L. (2010). Remote sensing of water surface temperature and heat flux over a tropical hydroelectric reservoir. Remote Sensing of Environment, 114(11):2651–2665.

Allan, M. G., Hamilton, D. P., Trolle, D., Muraoka, K., and McBride, C. (2016). Spatial heterogeneity in geothermally-influenced lakes derived from atmospherically corrected Landsat thermal imagery and three-dimensional hydrodynamic modelling. International Journal of Applied Earth Observation and Geoinformation, 50:106–116.

Barnes, W. L., Pagano, T. S., and Salomonson, V. V. (1998). Prelaunch characteristics of the Moderate Resolution Imaging Spectroradiometer (MODIS) on EOS-AM1. IEEE Transactions on Geoscience and Remote Sensing, 36(4):1088–1100.

Barsi, J. A., Barker, J. L., and Schott, J. R. (2003a). An atmospheric correction parameter calculator for a single thermal band earth-sensing instrument. In Proceedings of the 2003 IEEE Geoscience and Remote Sensing Symposium (IGARSS'03), volume 5, pages 3014–3016.

Barsi, J. A., Schott, J., Palluconi, F. D., Helder, D. L., Hook, S. J., Markham, B. L., Chander, G., and O'Donnell, E. M. (2003b). Landsat TM and ETM+ thermal band calibration. Canadian Journal of Remote Sensing, 29(2):141–153.

Barsi, J. A., Schott, J., Palluconi, F. D., and Hook, S. J. (2005). Validation of a web-based atmospheric correction tool for single thermal band instruments. In Earth Observing Systems X, volume 5882, page 58820E. International Society for Optics and Photonics.

Bivand, R., Keitt, T., and Rowlingson, B. (2017). rgdal: Bindings for the 'Geospatial' Data Abstraction Library. R package version 1.2-15.

Bivand, R. and Lewin-Koh, N. (2017). maptools: Tools for Reading and Handling Spatial Objects. R package version 0.9-2.

Bivand, R. and Rundel, C. (2017). rgeos: Interface to Geometry Engine - Open Source ('GEOS'). R package version 0.3-26.

Cavalcanti, J. R., da Motta-Marques, D. M. L., and Fragoso Jr, C. R. (2016). Process-based modeling of shallow lake metabolism: Spatio-temporal variability and relative importance of individual processes. Ecological Modelling, 323:28–40.

Chander, G., Markham, B. L., and Helder, D. L. (2009). Summary of current radiometric calibration coefficients for Landsat MSS, TM, ETM+, and EO-1 ALI sensors. Remote Sensing of Environment, 113:893–903.

Chavula, G., Brezonik, P., Thenkabail, P., Johnson, T., and Bauer, M. (2009). Estimating the surface temperature of lake malawi using AVHRR and MODIS satellite imagery. Physics and Chemistry of the Earth, Parts A/B/C, 34(13-16):749–754.

Coll, C., Caselles, V., Valor, E., and Niclòs, R. (2012). Comparison between different sources of atmospheric profiles for land surface temperature retrieval from single channel thermal infrared data. Remote Sensing of Environment, 117:199–210.

Cristóbal, J., Jiménez-Muñoz, J. C., Sobrino, J. A., Ninyerola, M., and Pons, X. (2009). Improvements in land surface temperature retrieval from the Landsat series thermal band using water vapor and air temperature. Journal of Geophysical Research, 114:D08103.

Crosman, E. T. and Horel, J. D. (2009). MODIS-derived surface temperature of the Great Salt Lake. Remote Sensing of Environment, 113(1):73–81.

Crossetti, L. O., Becker, V., de Souza Cardoso, L., Rodrigues, L. R., da Costa, L. S., and Motta-Marques, D. (2013). Is phytoplankton functional classification a suitable tool to investigate spatial heterogeneity in a subtropical shallow lake? Limnologica-Ecology and Management of Inland Waters, 43(3):157–163.

Curtarelli, M., Alcântara, E., Rennó, C., and Stech, J. (2013). Effects of cold fronts on MODIS-derived sensible and latent heat fluxes in Itumbiara reservoir (Central Brazil). Advances in Space Research, 52(9):1668–1677.

Deng, C. and Wu, C. (2013). Examining the impacts of urban biophysical compositions on surface urban heat island: A spectral unmixing and thermal mixing approach. Remote Sensing of Environment, 131:262–274.

Díaz-Delgado, R., Ameztoy, I., Cristóbal, J., and Bustamante, J. (2010). Long time series of Landsat images to reconstruct river surface temperature and turbidity regimes of Guadalquivir Estuary. In Proceedings of the 2010 IEEE Geoscience and Remote Sensing Symposium (IGARSS'10), pages 233–236.

Fairall, C., Bradley, E. F., Godfrey, J., Wick, G., Edson, J. B., and Young, G. (1996). Cool-skin and warm-layer effects on sea surface temperature. Journal of Geophysical Research: Oceans, 101(C1):1295–1308.

Fragoso Jr, C. R., Marques, D. M. M., Ferreira, T. F., Janse, J. H., and van Nes, E. H. (2011). Potential effects of climate change and eutrophication on a large subtropical shallow lake. Environmental Modelling & Software, 26(11):1337–1348.

Fricke, K. and Baschek, B. (2013). Water surface temperature profiles for the Rhine river derived from Landsat ETM+ data. In Proceedings of SPIE 8887, Remote Sensing for Agriculture, Ecosystems, and Hydrology XV, page 88870E.

Friedman, D. (1969). Infrared characteristics of ocean water (1.5–15 μ). Applied Optics, 8(10):2073–2078.

Gholizadeh, M., Melesse, A., and Reddi, L. (2016). A comprehensive review on water quality parameters estimation using remote sensing techniques. Sensors, 16(8):1298.

Handcock, R., Gillespie, A., Cherkauer, K., Kay, J., Burges, S., and Kampf, S. (2006). Accuracy and uncertainty of thermal-infrared remote sensing of stream temperatures at multiple spatial scales. Remote Sensing of Environment, 100(4):427–440.

Handcock, R. N., Torgersen, C. E., Cherkauer, K. A., Gillespie, A. R., Tockner, K., Faux, R. N., and Tan, J. (2012). Thermal infrared remote sensing of water temperature in riverine landscapes. Fluvial Remote Sensing for Science and Management, pages 85–113.

Harris, A. and Mason, I. (1992). An extension to the split-window technique giving improved atmospheric correction and total water vapour. International Journal of Remote Sensing, 13(5):881–892.

Hijmans, R. J. (2017). raster: Geographic Data Analysis and Modeling. R package version 2.6-7.

Horne, A. J. and Goldman, C. R. (1994). Limnology. McGraw-Hill New York.

Hulley, G. C., Hook, S. J., and Schneider, P. (2011). Optimized split-window coefficients for deriving surface temperatures from inland water bodies. Remote Sensing of Environment, 115(12):3758–3769.

Jiménez-Muñoz, J. and Sobrino, J. (2006). Error sources on the land surface temperature retrieved from thermal infrared single channel remote sensing data. International Journal of Remote Sensing, 27(05):999–1014.

Jiménez-Muñoz, J. C., Cristobal, J., Sobrino, J. A., Soria, G., Ninyerola, M., Pons, X., and Pons, X. (2009). Revision of the single-channel algorithm for land surface temperature retrieval from Landsat thermal-infrared data. IEEE Transactions on Geoscience and Remote Sensing, 47(1):339–349.

Jiménez-Muñoz, J. C. and Sobrino, J. A. (2003). A generalized single-channel method for retrieving land surface temperature from remote sensing data. Journal of Geophysical Research, 108:D22.

Jiménez-Muñoz, J. C., Sobrino, J. A., Mattar, C., and Franch, B. (2010). Atmospheric correction of optical imagery from MODIS and Reanalysis atmospheric products. Remote Sensing of Environment, 114(10):2195–2210.

Kay, J. E., Kampf, S. K., Handcock, R. N., Cherkauer, K. A., Gillespie, A. R., and Burges, S. J. (2005). Accuracy of lake and stream temperatures estimated from thermal infrared images. JAWRA Journal of the American Water Resources Association, 41(5):1161–1175.

Kilpatrick, K., Podestá, G., Walsh, S., Williams, E., Halliwell, V., Szczodrak, M., Brown, O., Minnett, P., and Evans, R. (2015). A decade of sea surface temperature from MODIS. Remote Sensing of Environment, 165:27–41.

Kottek, M., Grieser, J., Beck, C., Rudolf, B., and Rubel, F. (2006). World map of the Köppen-Geiger climate classification updated. Meteorologische Zeitschrift, 15(3):259–263.

Lamaro, A. A., Mariñelarena, A., Torrusio, S. E., and Sala, S. E. (2013). Water surface temperature estimation from Landsat 7 ETM+ thermal infrared data using the generalized single-channel method: Case study of Embalse del Río Tercero (Córdoba, Argentina). Advances in Space Research, 51(3):492–500.

Li, Z.-L., Tang, B.-H., Wu, H., Ren, H., Yan, G., Wan, Z., Trigo, I. F., and Sobrino, J. A. (2013). Satellite-derived land surface temperature: Current status and perspectives. Remote Sensing of Environment, 131:14–37.

Ling, F., Foody, G. M., Du, H., Ban, X., Li, X., Zhang, Y., and Du, Y. (2017). Monitoring thermal pollution in rivers downstream of dams with Landsat ETM+ thermal infrared images. Remote Sensing, 9(11):1175.

Liu, G., Ou, W., Zhang, Y., Wu, T., Zhu, G., Shi, K., and Qin, B. (2015). Validating and mapping surface water temperatures in Lake Taihu: Results from MODIS land surface temperature products. IEEE Journal of Selected Topics in Applied Earth Observations and Remote Sensing, 8(3):1230–1244.

Luz, G. A., Guasselli, L. A., and Rocha, D. (2017). Temperature surface of Guaíba Lake, RS, from time series of MODIS images. Brazilian Journal of Water Resources, 22.

MacCallum, S. N. and Merchant, C. J. (2012). Surface water temperature observations of large lakes by optimal estimation. Canadian Journal of Remote Sensing, 38(1):25–45.

Mao, K., Qin, Z., Shi, J., and Gong, P. (2005). A practical split-window algorithm for retrieving land-surface temperature from MODIS data. International Journal of Remote Sensing, 26(15):3181–3204.

Masuda, K., Takashima, T., and Takayama, Y. (1988). Emissivity of pure and sea waters for the model sea surface in the infrared window regions. Remote Sensing of Environment, 24(2):313–329.

Munar, A. M. (2017). Pareamento Bacia-Lagoa usando modelagem hidrológica-hidrodinâmica e sensoriamento remoto. PhD Thesis, Postgraduate Program in Water Resources and Environmental Sanitation, Federal University of Rio Grande do Sul, 139 p.

Okwen, R., Pu, R., and Cunningham, J. (2011). Remote sensing of temperature variations around major power plants as point sources of heat. International Journal of Remote Sensing, 32(13):3791–3805.

O'Reilly, C. M., Sharma, S., Gray, D. K., Hampton, S. E., Read, J. S., Rowley, R. J., Schneider, P., Lenters, J. D., McIntyre, P. B., Kraemer, B. M., et al. (2015). Rapid and highly variable warming of lake surface waters around the globe. Geophysical Research Letters, 42(24):10–773.

Pareeth, S., Salmaso, N., Adrian, R., and Neteler, M. (2016). Homogenised daily lake surface water temperature data generated from multiple satellite sensors: A long-term case study of a large sub-alpine lake. Scientific reports, 6:31251.

Pebesma, E. J. and Bivand, R. S. (2005). Classes and methods for spatial data in R. R News, 5(2):9–13.

Prats, J., Reynaud, N., Rebière, D., Peroux, T., Tormos, T., and Danis, P.-A. (2018). LakeSST: Lake Skin Surface Temperature in French inland water bodies for 1999–2016 from Landsat archives. Earth System Science Data, 10(2):727–743.

R Core Team (2017). R: A Language and Environment for Statistical Computing. R Foundation for Statistical Computing, Vienna, Austria.

Reinart, A. and Reinhold, M. (2008). Mapping surface temperature in large lakes with MODIS data. Remote Sensing of Environment, 112:603–611.

Robinson, I., Wells, N., and Charnock, H. (1984). The sea surface thermal boundary layer and its relevance to the measurement of sea surface temperature by airborne and spaceborne radiometers. International Journal of Remote Sensing, 5(1):19–45.

Ruiz-Verdú, A., Jiménez, J. C., Lazzaro, X., Tenjo, C., Delegido, J., Pereira, M., Sobrino, J. A., and Moreno, J. (2016). Comparison of MODIS and Landsat-8 retrievals of chlorophyll-a and water temperature over Lake Titicaca. In Proceedings of the 2016 IEEE Geoscience and Remote Sensing Symposium (IGARSS'16), pages 7643–7646.

Schluessel, P., Emery, W. J., Grassl, H., and Mammen, T. (1990). On the bulk-skin temperature difference and its impact on satellite remote sensing of sea surface temperature. Journal of Geophysical Research: Oceans, 95(C8):13341–13356.

Schneider, K. and Mauser, W. (1996). Processing and accuracy of Landsat Thematic Mapper data for lake surface temperature measurement. International Journal of Remote Sensing, 17(11):2027–2041.

Schneider, P. and Hook, S. J. (2010). Space observations of inland water bodies show rapid surface warming since 1985. Geophysical Research Letters, 37(22).

Schott, J. R. (2007). Remote sensing: the image chain approach. Oxford University Press; 2nd edition.

Sima, S., Ahmadalipour, A., and Tajrishy, M. (2013). Mapping surface temperature in a hyper-saline lake and investigating the effect of temperature distribution on the lake evaporation. Remote Sensing of Environment, 136:374–385.

Simon, R., Tormos, T., and Danis, P.-A. (2014). Retrieving water surface temperature from archive LANDSAT thermal infrared data: Application of the mono-channel atmospheric correction algorithm over two freshwater reservoirs. International Journal of Applied Earth Observation and Geoinformation, 30:247–250.

Snyder, W. C., Wan, Z., Zhang, Y., and Feng, Y.-Z. (1998). Classification-based emissivity for land surface temperature measurement from space. International Journal of Remote Sensing, 19(14):2753–2774.

Sobrino, J. A., Jiménez-Muñoz, J. C., and Paolini, L. (2004). Land surface temperature retrieval from Landsat TM 5. Remote Sensing of Environment, 90(4):434–440.

Sobrino, J. A., Jiménez-Muñoz, J. C., Soria, G., Romaguera, M., Guanter, L., Moreno, J., Plaza, A., and Martinez, P. (2008). Land surface emissivity retrieval from different VNIR and TIR sensors. IEEE Transactions on Geoscience and Remote Sensing, 46(2):316–327.

Sobrino, J. A. and Raissouni, N. (2000). Toward remote sensing methods for land cover dynamic monitoring: Application to Morocco. International Journal of Remote Sensing, 21(2):353–366.

Walton, C., Pichel, W., Sapper, J., and May, D. (1998). The development and operational application of nonlinear algorithms for the measurement of sea surface temperatures with the NOAA polar-orbiting environmental satellites. Journal of Geophysical Research: Oceans, 103(C12):27999–28012.

Wan, Z. and Dozier, J. (1996). A generalized split-window algorithm for retrieving land-surface temperature from space. IEEE Transactions on Geoscience and Remote Sensing, 34(4):892–905.

Ward, B. (2006). Near-surface ocean temperature. Journal of Geophysical Research: Oceans, 111(C2).
Weng, Q., Fu, P., and Gao, F. (2014). Generating daily land surface temperature at Landsat resolution by fusing Landsat and MODIS data. Remote Sensing of Environment, 145:55–67.
Wloczyk, C., Richter, R., Borg, E., and Neubert, W. (2006). Sea and lake surface temperature retrieval from landsat thermal data in Northern Germany. International Journal of Remote Sensing, 27(12):2489–2502.
Woolway, R. I., Jones, I. D., Maberly, S. C., French, J. R., Livingstone, D. M., Monteith, D. T., Simpson, G. L., Thackeray, S. J., Andersen, M. R., Battarbee, R. W., et al. (2016). Diel surface temperature range scales with lake size. PLoS One, 11(3):e0152466.
Woolway, R. I. and Merchant, C. J. (2018). Intralake heterogeneity of thermal responses to climate change: A study of large Northern Hemisphere lakes. Journal of Geophysical Research: Atmospheres, 123(6):3087–3098.
Yang, K., Yu, Z., Luo, Y., Yang, Y., Zhao, L., and Zhou, X. (2018). Spatial and temporal variations in the relationship between lake water surface temperatures and water quality–a case study of Dianchi Lake. Science of the Total Environment, 624:859–871.
Yu, X., Guo, X., and Wu, Z. (2014). Land surface temperature retrieval from Landsat 8 TIRS–comparison between radiative transfer equation-based method, split window algorithm and single channel method. Remote Sensing, 6(10):9829–9852.
Zhang, Q., Ye, X.-c., Werner, A. D., Li, Y.-l., Yao, J., Li, X.-h., and Xu, C.-y. (2014). An investigation of enhanced recessions in Poyang Lake: comparison of Yangtze River and local catchment impacts. Journal of Hydrology, 517:425–434.
Zhang, Y. (1999). MODIS UCSB Emissivity Library. `https://icess.eri.ucsb.edu/modis/EMIS/html/em.html`. Acessed on December 5th, 2018.

Capítulo 3

Calibration of river water temperature models using Landsat 7 ETM+ and downscaled MODIS-derived data

Matheus Henrique Tavares

Artigo a ser submetido.

Calibration of river water temperature models using Landsat 7 ETM+ and downscaled MODIS-derived data

Matheus Henrique Tavares*

Abstract

In this work, we tested the calibration of two river water temperature (RWT) models, *air2stream* and a stochastic model, using water temperature data derived from Landsat 7 ETM+ images and downscaled MODIS images, in order to generate continuous daily water temperature data series. This study is divided into three parts: *(i)* in the first part we evaluated two methods to estimate RWT Landsat 7 ETM+ imagery, with the additional application of a thermal sharpening technique; *(ii)* in the second part we evaluated the effectiveness of a downscaling technique to estimate RWT; and *(iii)* in the third part we evaluated the calibration, using these images, of the models to generate the continuous river temperature data series. White river was selected as the subject of study, located near Hazleton, IN, USA. The downscaling technique employed was the data fusion model SADFAT, and a selection criteria was developed to avoid the assimilation of inaccurate data in the series. For the Landsat-derived RWT, the application of the radiative transfer equation with the Atmospheric Correction Paramater Calculator (AtmCorr) showed the best results, with bias and RMSE of 0.014°C and 1.32°C, respectively, and the thermal sharpening improved the accuracy of all results. The data fusion model showed a poor performance, with RMSE of 5.41°C, and the selection criteria greatly improved the accuracy of the MODIS-derived RWT data series, reducing RMSE to 2.25°C, although there were a few overestimated RWT incorporated in the data series, and the RMSE of the resulting combined series (Landsat and MODIS-derived RWT) was 2°C. The *air2stream* model outperformed the stochastic models, with RMSE of 1.91°C, when calibrated with Landsat data, and 1.88°C when calibrated with Landsat and MODIS data combined. The inclusion of the downscaled MODIS data had very little impact on the performance of *air2stream*. Considering the low number of input data of its calibration, the model showed a great performance, generating a consistent, continuous RWT data series, and can be applied in many studies in rivers with no measured *in situ* water temperature data, such as analysing past and present trends in river temperatures, and in modelling tributary temperatures for ecological models. We recommend tests of the accuracy of the Landsat-derived water temperatures in other rivers, as there is limited studies in this subject, further tests of the performance of the *air2stream* model calibrated with RWT derived from remote sensing, with the inclusion of data derived from other sensors, such as Landsat 8 TIRS and encourage the development of thermal sharpening techniques and data fusion models focusing on water resources, taking advantage of the recent launching of the Sentinel-3 program, in a way to improve the temporal resolution and the accuracy of retrievals of river water temperatures from remote sensing imagery, efforts that are necessary for the development of a open global database of surface temperatures.

Keywords: Water-surface temperature, rivers, remote sensing, downscaling, river temperature modelling, Landsat, MODIS

1. Introduction

Water temperature regulates many physical, chemical and biological processes in rivers and streams, such as species metabolic rates and distribution, primary production, nutrient cycling and oxygen solubility (Allan and Castillo, 2007). An increasing of interest in water temperature data has emerged due to the need to evaluate the impacts of anthropogenic interventions and climate change on rivers. As these impacts are not uniform across different rivers and streams, but

*More authors will be included before submission.

vary with climatic, morphological and geographical characteristics (van Vliet et al., 2013), the knowledge and patterns of variation of water temperature is necessary to assess and predict such impacts, and is required for managing water resources (Orr et al., 2015). Additionally, tributary rivers can influence the temperature profiles of lakes and reservoirs, and therefore, are important as input data in the ecological modelling of lakes (Fenocchi et al., 2017; Vinnå et al., 2017). Despite its importance in understanding the past and present ecological status of these water bodies, river water temperature (RWT) data are scarce (Webb et al., 2008). In cases where there are no *in situ* RWT measurements, a synthetic river temperature data series can be estimated using other available data (*e.g.* meteorological and hydrological data), in a way to improve the understanding of the river thermal regime (*e.g.* Stefan and Preud'homme, 1993; Mohseni and Stefan, 1999; Caissie et al., 2001; Sahoo et al., 2009).

River temperature modelling has been extensively used as a tool to simulate water temperature in poorly gauged and ungauged rivers (Caissie, 2006). It has many useful applications, such as in predicting fish growth rate (Crisp and Howson, 1982), predicting the impact of projected air temperatures (Sinokrot et al., 1995; Mohseni et al., 1999) and riparian vegetation cover and stream discharge (Woltemade and Hawkins, 2016) on water temperature, assessing the spatiotemporal suitability of cold fish habitats (Ruesch et al., 2012; Jackson et al., 2018), assessing the impact of a dam on the dynamics of a river (Cai et al., 2018), and evaluating the impact of predicted higher air temperatures in lake water temperatures using a lake water model (Piccolroaz et al., 2018). River temperature modelling is challenging, since water temperature is a result of a multitude of factors (Caissie, 2006; Dugdale et al., 2017), but in a daily timescale, air temperature is its major driver (Caissie et al., 2001; Webb et al., 2008), controlled by river discharge (Gu et al., 1998; Toffolon and Piccolroaz, 2015).

Several models to estimate RWT have been proposed, ranging from simple regression models (*e.g.* Crisp and Howson, 1982) and stochastic models (*e.g.* Caissie et al., 2001) to more complex deterministic models (*e.g.* Sinokrot and Stefan, 1993). The main restrain of most of these models, however, is that it is assumed that there are *in situ* water temperature data enough for calibration and validation, considering the reach of river studied. However, in many cases measurements of RWT are scarce or nonexisting, impeding their application. A still underexplored approach to overcome this is to use remote sensing to estimate RWT (Handcock et al., 2012; Dugdale et al., 2017). Despite limitations (mainly the spatial and temporal sensor resolutions trade-offs, and the estimation being limited to the "skin temperature" – top 100 μm – only), it is a growing and well established practice, since it provides information of spatiotemporal variation of water temperature (Kay et al., 2005; Handcock et al., 2012). Although it has a more restrict range of applications in the literature, when compared to land surface (*e.g.* Fu and Weng, 2016) or lake surface water temperatures (*e.g.* Allan et al., 2016), it has being successfully applied in studies of spatiotemporal patterns of river temperature (Díaz-Delgado et al., 2010; Ling et al., 2017), longitudinal profiles of river temperatures (Wawrzyniak et al., 2012; Fricke and Baschek, 2013, 2015), and calibrating a river temperature (Cristea and Burges, 2009) and a hydrodynamic model (Pahlevan et al., 2011).

Despite the range of applications of airborne thermal sensors in river studies (*e.g.* Wawrzyniak et al., 2013; Vatland et al., 2015; Dugdale et al., 2018; Marruedo Arricibita et al., 2018), they can not be used in the long-term calibration of water temperature models due to its limited temporal availability. For long-term studies of objects such as rivers and urban environments, which require a better spatial resolution, the most widely used sensor is Landsat 7 ETM+ (*e.g.* Handcock et al., 2006; Wawrzyniak et al., 2012; Fu and Weng, 2016), due to its medium spatial and temporal resolution and large temporal availability, with the mission starting in 1999. It has a temporal resolution of 16 days and a spatial resolution of 30 m, with the exception of its thermal band, which has a resolution 60 m, restricting its application to larger water bodies. However, due to its temporal resolution and the limiting factor of cloud cover, in most cases there are just under 20 images (and, therefore, water temperature data) per year, which might result in an inefficient calibration of the water temperature models. Therefore, efforts to include thermal images from other sensors to complement the Landsat-derived river temperature data are important to improve the calibration of these models.

MODIS images, which are daily, are commonly employed in studies of land surface temperature (LST) (*e.g.* Crosman and Horel, 2009; Vancutsem et al., 2010; Schwarz et al., 2011; Weng et al., 2014), also due to its long time series, with the Terra satellite being launched in 2000. However due to its coarse resolution of 1000 m, it can not be used in studies of RWT. Downscaling techniques may be used in order to improve the spatial resolution of coarser spatial resolution sensors (but better temporal resolution) by combining them with Landsat images. Many algorithms to downscale coarser spatial resolution images have been proposed, however these algorithms were not developed focusing on water resources, and most can not be used in studies of water bodies due to assumption of a relationship between temperature and NDVI, which is only valid for land surface temperatures (Mukherjee et al., 2014). Weng

et al. (2014) developed a spatial image fusion technique, SADFAT (Spatio-temporal Adaptive Data Fusion Algorithm for Temperature mapping), as a result of an improvement of STARFM (Spatial and Temporal Adaptive Reflectance Fusion Model), developed by Gao et al. (2006), and ESTARFM (Enhanced Spatial and Temporal Adaptive Reflectance Fusion Model), developed by Zhu et al. (2010), to fusion MODIS and Landsat surface temperature images to produce a series of thermal images with Landsat spatial resolution and MODIS temporal resolution. STARFM, which has been constantly improved since its creation (*e.g.* Hilker et al., 2009 and Zhu et al., 2010), proposed to combine two pairs of Landsat and MODIS images on the same date to apply linear functions based on their similarities to the MODIS images in between these dates, in order to enhance the spatial resolution of the MODIS images, focusing mainly on changes in vegetation. Although SADFAT has the potential of increasing the number of images per year with resolution high enough for the river water temperature to be derived, it has not been tested yet for retrieving river temperatures or the information of single pixels inside MODIS heterogeneous pixels, and thus its performance needs to be assessed.

Using only remote sensing data, by combining MODIS LST product MOD11 with Landsat 7's estimated LST (which needs to be derived by the user, using different available methods, as reviewed by Li et al., 2013), it is possible to calibrate a river water temperature model to generate a continuous daily water temperature data series. The objective of this study is to test this approach, using SADFAT to downscale MODIS LST images, with Landsat-derived LST images as basis, and using the resulting river temperature data to calibrate water temperature models. This study is divided into three parts: *(i)* in the first part we evaluated methods to estimate river water temperature using Landsat 7 ETM+ imagery; *(ii)* in the second part we evaluated the effectiveness of the downscaling technique to estimate river water temperatures; and *(iii)* in the third part we evaluated the calibration, using these images, of different models to generate the continuous river temperature data series.

2. Materials and methods

2.1. Study area and field data

Our approach was tested in White river, in Hazleton, Indiana, USA. The climate is Dfa (Kottek et al., 2006), characterised by hot, wet summers and cold winters, when the White river can freeze, a mean temperature of 12.55°C and a mean annual precipitation of 1200 mm. Land is mostly covered by agriculture and grasslands in the region. The river temperature and flow data were downloaded for the White river station (Figure 3.1) at Hazleton, IN (code 03374100) from the freely available National Real-Time Water Quality platform, from the US Geological Survey (available on `https://nrtwq.usgs.gov/`). The selected study period comprised of 01-01-2013 to 31-12-2017. The measured river water temperature data series presented a few missing data, most of them concentrated in a seven-month period ranging from 26-2-2015 to 7-10-2015. The air temperature data was download for the Lancennes airport meteorological station (Lawrenceville-Vincennes International Airport, code 13809), 30 km away from the river station (Figure 3.1), from the freely available National Centers for Environment Protection (NCEP/NOAA, `https://www.ncei.noaa.gov/`) database. The data series was complete, and transformed in a daily mean time-series of air temperature.

The simplified methodology of this work was divided in the following steps, illustrated by the flow chart in Figure 3.2:

1. Remote estimation of river water temperature from Landsat 7 ETM+ images, converting the thermal band to surface temperature using three different methods and assessing their performance
2. downscaling MOD11A1 daily LST, using SADFAT and the Landsat surface temperatures generated in step 1 as basis, and then evaluating the performance of this algorithm in generating river temperatures
3. comparing both approaches as input data to calibrate the water temperature models, and then compare the output synthetic river water temperature data series with *in situ* data

The following sections detail the water temperature models and the methods used for the Landsat and MODIS images in this study. The algorithms for all these processes was written in *R* (R Core Team, 2018), with the help of packages *maptools* (Bivand and Lewin-Koh, 2017), *raster* (Hijmans, 2017), *rgdal* (Bivand et al., 2018), *rgeos* (Bivand and Rundel, 2017) and *sp* (Pebesma and Bivand, 2005).

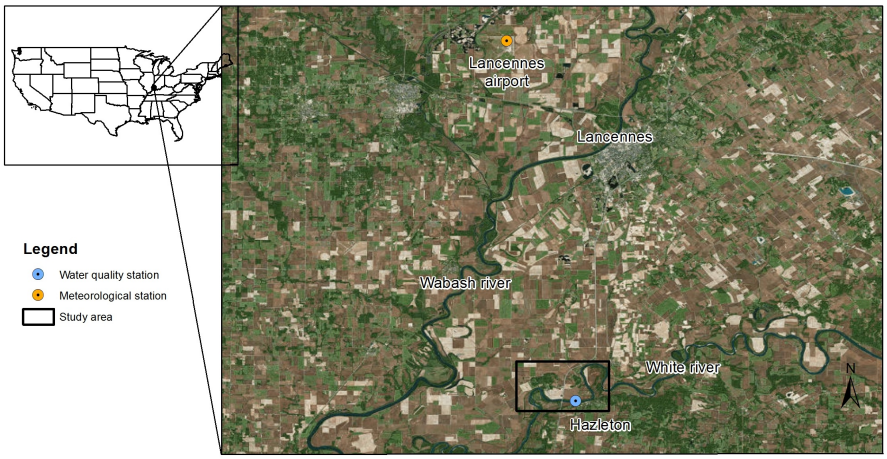

Figure 3.1: Map of the study area showing the White river in Hazleton, Indiana, USA, the water quality station and the meteorological station at the Lancennes Airport.

2.2. River water temperature models

A number of models have been proposed in the literature, from simple regressions to physically-based models. The latter, more complex models, require a great number of input data, mainly of meteorological variables, and so were not considered here. Recently, Toffolon and Piccolroaz (2015) developed a hybrid model to produce river temperature data series based on air temperature and river discharge. Their model, called *air2stream*, is an adaptation of the *air2lake* model, which depends only on air temperature (Piccolroaz et al., 2013). Despite its recent publication, it has attracted attention due to its good performance over a range of different rivers (Cai et al., 2018; Piotrowski and Napiorkowski, 2018). Piccolroaz et al. (2016) compared a range of models, such as linear regressions and stochastic models, with *air2stream* in Swiss rivers with different morphological characteristics, and the latter (in its complete version) showed better performance in most cases, with mean value of a modified Nash-Sutcliffe efficiency coefficient (NSE*) and root-mean squared error (RMSE) of 0.49 and 0.8°C, respectively. Despite the complex physical basis of the model, it only requires air temperature and river flow and temperature data to be calibrated. It is interesting to test our approach using other models as well, since no study has accessed the performance of models calibrated with series with very low temperature data. With this intent, a simpler, stochastic model was employed, as considered in the work of Piccolroaz et al. (2016). The model was used in three different versions, as detailed in Section 2.2.1.

For comparison, these models were calibrated using both Landsat-derived and a combined temperature series using Landsat and MODIS sensors. For the stochastic models, only one calendar year of data can be used, and so 2013 was chosen for having a larger number of Landsat-derived temperature data, and 2017 for having a larger number of Landsat and MODIS combined temperature data.

2.2.1. Stochastic model

In the stochastic model, river water temperature is divided in two components (Caissie et al., 1998):

$$T_w(t) = \mathrm{LT}_w(t) + \mathrm{ST}_w(t) \tag{1}$$

where $\mathrm{LT}_w(t)$ is the annual variation component, or long-term component, and $\mathrm{ST}_w(t)$ is the anomaly or residue of this component, or the short-term component.

The long-term component is calculated for both water and air temperature and two methods can be applied: a Fourier series (Kothandaraman, 1971) or a sinusoidal function (Cluis, 1972). The Fourier series is given by:

$$\mathrm{LT}(t) = \frac{A_o}{2} + \sum_{n=1}^{\infty} \left\{ A_n \cos\left[(t-j-1)\frac{2n\pi}{N}\right] + B_n \mathrm{sen}\left[(t-j-1)\frac{2n\pi}{N}\right] \right\} \tag{2}$$

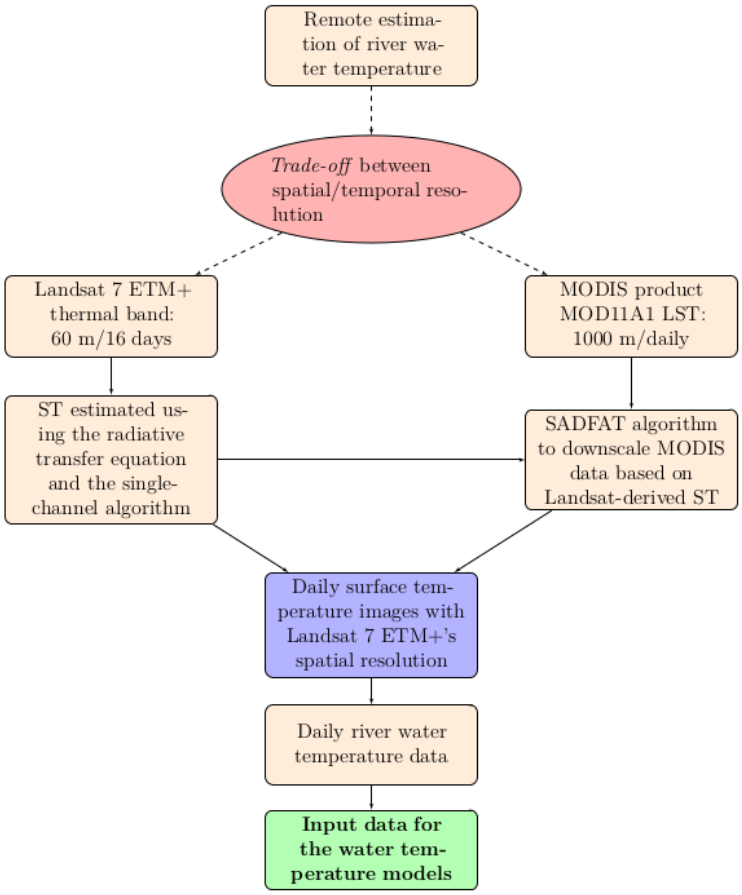

Figure 3.2: Flow chart illustrating the process of acquisition of river water temperature data, which are the input to the river temperature models.

where $A_o/2$ is the mean temperature in the period, n is the number of harmonics, t is time (days, in this case), j is the first observed Julian day in the period ($j = 90$, for example, if starting on March 31st), N is the number of days, and A_n and B_n are given by:

$$A_n = \frac{2}{N}\sum_{t=1}^{N} f(t)\text{sen}\left(\frac{2\pi nt}{N}\right) \tag{3}$$

and

$$B_n = \frac{2}{N}\sum_{t=1}^{N} f(t)\text{sen}\left(\frac{2\pi nt}{N}\right) \tag{4}$$

for the n harmonics, where $f(t)$ is the water or air temperature on day t. Here, values of $n = 1$ and $n = 2$ were considered.

The sinusoidal function is given by:

$$\text{LT}(t) = a + b\text{sen}\left[\frac{2\pi}{N}(t + t_o)\right] \tag{5}$$

where a, b and t_o are the fitted coefficients. Here, the coefficients were calculated using the least squared method, according to Cluis (1972).

After calculating the long-term components LT for air and water, each measured datum is subtracted by its respective component, resulting in the residue of each series. To model the short-term component, we chose a multiple regression

(Kothandaraman, 1971), used in the work of Caissie et al. (1998) due to the simplicity of application and its good results. This method consists in calculating the coefficients of a linear regression between water and air temperature series, where the air temperature series are also lagged 1-2 days. The short-term component is then calculated by (Kothandaraman, 1971):

$$R_w(t) = \beta_1 R_a(t) + \beta_2 R_a(t-1) + \beta_3 R_a(t-2) \tag{6}$$

where $R_w(t)$ and $R_a(t)$ are the residue of the water and air temperature series on day t, and β_n are the coefficients.

With the values of coefficients β_1, β_2 e β_3 calculated for the calibration period, they are used to calculate the component ST_w for each year of the validation period (*i.e.* the rest of the data series) and added to the long-term component LT_w for each day (Equation 1), obtaining the modelled water temperature series for the whole studied period.

2.2.2. air2stream model

The *air2stream* model is based on a lumped heat budget equation applied to river stretches, and considers that the heat exchange between the surface and the atmosphere is a function of air temperature (Mohseni and Stefan, 1999; Caissie et al., 2005). After a few simplifications and assumptions, the equation was transformed in a physical-empirical model of an ordinary differential equation with 8 parameters to be calibrated. The authors highlighted that this processes has the advantage of representing other local effects that are not taken into account directly in the heat budget equation, such as cloud and vegetation cover. The equation of the model is given by:

$$\frac{dT_w}{dt} = \frac{1}{\delta}\left\{a_1 + a_2 T_a - a_3 T_w + \theta\left[a_5 + a_6 \cos\left(2\pi\left(\frac{t}{t_y} - a_7\right)\right) - a_8 T_w\right]\right\} \tag{7}$$

where T_w is the water temperature, $\theta = \frac{Q}{\bar{Q}}$, Q is the river flow and $\bar{Q}$ is the mean flow during the period studied, $\delta = \theta^{a_4}$, T_a is the air temperature, t is the time (in days), t_y is the number of time steps over a year (number of days in the year, for a daily time step), and the a_n, $n = 1, 2, 3, .., 8$, are the eight parameters to be calibrated.

At each iteration, this differential equation is numerically integrated, and it is calibrated using an optimisation algorithm to minimise an objective-function. Here, the full 8-parameter model was employed, using Crank-Nicolson as the numerical scheme, and Particle Swarm Optimisation to minimise the RMSE. We used 4 years (2013–2016) as the calibration period, and one year (2017) for the validation of the resulting data series. Since the model depends on this calibration process, the model ran 5 times using each calibration data set, in order to verify the reliability of the results.

2.3. Landsat 7 ETM+ Images

Although computational process is similar,studies evaluating the accuracy of estimations of RWT using Landsat 7 ETM+ are scarce in the literature in comparison to studies of lake surface water temperatures (*e.g.* Lamaro et al., 2013; Simon et al., 2014; Allan et al., 2016; Prats et al., 2018). This is a consequence of this estimation being limited to larger water bodies, due to the 60 m spatial resolution of the thermal band. Few studies assessing this accuracy in rivers highlighted the issues in these estimations, such as the need of "pure" (*i.e.* unmixed) water pixels (Cherkauer et al., 2005), of atmospheric and emissivity correction (Kay et al., 2005), and the importance of at least 3 pure pixels covering the section of the river for reliable temperature estimations (Handcock et al., 2006), restraining this application to rivers at least 180 m wide. Additionally, most studies show errors around ~1°C for bias, ~0.3–1°C for standard deviation (σ), and ~1.5°C for root-mean squared error (RMSE) (Kay et al., 2005; Handcock et al., 2006; Wawrzyniak et al., 2012; Fricke and Baschek, 2013, 2015), considerably higher than the errors in estimating lake surface water temperatures (Allan et al., 2016, for example, found RMSE of 0.48–0.94°C).

There are different approaches available in estimating LST using Landsat images, which were already compared in a few lake studies, but only by Fricke and Baschek (2013) in rivers. They were also tested here, and are presented in section 2.3.1. Additionally, due to the limited accuracy in estimating river temperatures, an attempt was made to enhance it using a technique called *thermal sharpening*, which aims to enhance the spatial resolution of a thermal image by using auxiliary data (Zhan et al., 2013). The thermal sharpening technique employed in this study is presented in section 2.3.2.

2.3.1. Methods to estimate RWT

Remote estimation of the ST from Landsat images uses the radiative transfer equation or algorithms developed for this purpose (Li et al., 2013). The methodology applied here is similar to the study of Tavares et al. (2019), considering only freely available software and data, *i.e.* not considering proprietary radiative transfer models and radiosonde data.

The atmosphere affects the radiance measured by satellite-borne sensors, mainly water vapour, both absorbing and emitting radiance in the TIR spectrum (Jiménez-Muñoz et al., 2010). Therefore, it is necessary to correct the images from these atmospheric effects for an accurate estimation of the surface temperature. These effects are summarised by three atmospheric parameters: atmospheric transmittance (τ), and the emitted (L^{up}) and absorbed (L^{down}) radiance. The relationship between these parameters and the radiance measured by the sensor is described by the radiative transfer equation (RTE), given by (Schott, 2007):

$$L_{\text{sensor}} = [\varepsilon B + (1 - \varepsilon)L^{\text{down}}]\tau + L^{\text{up}} \tag{8}$$

where L_{sensor} is the top-of-atmosphere (TOA) radiance measured by the sensor, ε is the surface emissivity, and B is the spectral radiance emitted by a black body at a temperature T.

The atmospheric correction parameters must be derived from additional data provided from other sources, since it can not be done directly for sensor with only one thermal band (Barsi et al., 2003b; Li et al., 2013). We used NASA's Atmospheric Correction Parameter Calculator – AtmCorr (Barsi et al., 2003a, 2005), a freely available online platform (available on `https://atmcorr.gsfc.nasa.gov/`) that provides these parameters by applying MODTRAN 4.0 to atmospheric profiles modelled by the NCEP/NOAA, generated for a $1^\circ \times 1^\circ$ grid every 6 hours. The parameters are then linearly interpolated for the chosen Landsat thermal band for the time, date and location inputted on the platform. With these data, the TOA radiance is corrected using the following equation (Schott, 2007):

$$L_{\text{corr}} = \frac{L_{\text{sensor}} - L^{\text{up}} - \tau L^{\text{down}}(1 - \varepsilon)}{\varepsilon\tau} \tag{9}$$

The brightness temperature is calculated by inverting Planck's law, according to Chander et al. (2009):

$$T_{\text{sensor}} = \frac{K2}{\ln\left(\frac{K1}{L_{\text{sensor}}} + 1\right)} \tag{10}$$

where K1 and K2 are calibration constants, and for Landsat 7 ETM+ they are 666.09 W/(m^2 sr μm) and 1282.71 K, respectively.

In an attempt to simplify the RTE, Jiménez-Muñoz and Sobrino (2003) developed a single-channel algorithm to estimate surface temperature, focusing on Landsat 5 TM, creating atmospheric functions of the total columnar atmospheric water vapour content and then adjusting second-degree polynomials to it, considering a number of atmospheric profiles and applying the MODTRAN radiative transfer code to obtain the atmospheric parameters. Jiménez-Muñoz et al. (2009) updated the algorithm to include Landsat 4 TM and Landsat 7 ETM+. In this algorithm, the surface temperature is given by:

$$\text{ST} = \gamma[\varepsilon^{-1}(\psi_1 L_{\text{sensor}} + \psi_2) + \psi_3 - L_{\text{sensor}}] + T_{\text{sensor}} \tag{11}$$

where T_{sensor} is the brightness temperature, ψ_1, ψ_2, and ψ_3 are the atmospheric functions, and γ is calculated by:

$$\gamma = \left[\frac{c_2 L_{\text{sensor}}}{T_{\text{sensor}}^2}\left(\frac{\lambda_{\text{eff}}^4}{c_1}L_{\text{sensor}} + \lambda_{\text{eff}}^{-1}\right)\right]^{-1} \tag{12}$$

where $c_1 = 1.191 \times 10^8$ Wμm^4/m^{2}sr and $c_2 = 1.439 \times 10^4$ Kμm are the Planck's constants, and λ_{eff} is the effective wavelength of the thermal band, which is 11.269 μm for Landsat 7 ETM+ (Cristóbal et al., 2009). The atmospheric functions are calculated by:

$$\psi_n = c_n w^2 + b_n w + a_n \tag{13}$$

where $n = 1, 2, 3$; w is the atmospheric water vapour content, and a, b, and c are constants given by Jiménez-Muñoz et al. (2009), according to the chosen atmospheric profile database. In this study, we considered only one database,

TIGR3, which has a wide range of atmospheric profiles, and showed better results in our preliminary tests and in the study by Tavares et al. (2019) in lakes.

Although the atmospheric correction algorithm is little sensitive to the atmospheric water vapour content (Prats et al., 2018; Tavares et al., 2019), we tested two products of water vapour: *(a)* MODIS product MOD07L2, which is daily and has a spatial resolution of 5 km, and *(b)* AtmCorr, since it also provides an estimation of the water vapour content. Both products showed good results in the study of atmospheric parameter sources by Jiménez-Muñoz et al. (2010) and in the sensitivity analysis performed by Tavares et al. (2019).

The nomenclature of the different methods to estimate RWT is described in Table 3.1.

Table 3.1: Nomenclature of the methods used for the estimation of RWT using Landsat 7 ETM+ imagery.

Method	**Description**
AtmCorr	Radiative transfer equation applied with atmospheric correction parameters from AtmCorr
AtmCorr-TSh	AtmCorr with thermal sharpening
SC-ATC	Single-channel algorithm applied with AtmCorr's water vapour content
SC-ATC-TSh	SC-ATC with thermal sharpening
SC-MOD	Single-channel algorithm applied with MOD07L2's water vapour content
SC-MOD-TSh	SC-MOD with thermal sharpening

2.3.2. Thermal sharpening

Many thermal sharpening algorithms have been proposed, but as few of them were proposed for studies of water bodies (Teggi, 2012), and most of them are also based on a relationship between temperature and NDVI (*e.g.* Agam et al., 2007; Rodriguez-Galiano et al., 2012). As in the data fusion techniques, there is also a gap in the literature in studies comparing different thermal sharpening techniques to enhance the accuracy of thermal images focusing on water bodies (Zhan et al., 2013). Since this analysis is not the scope of this work, we employed a simple statistical algorithm, in order to evidence the power of these techniques in enhancing the accuracy of RWT estimations.

The algorithm employed was developed by Jing and Cheng (2010). It is a statistical non-linear algorithm, combined with a multivariate analysis between the TIR and other Landsat bands. While Jing and Cheng (2010) considered all Landsat bands, here we only used bands 1–4, that is, in the visible and NIR spectra, which have more influence on land cover and thus, on the sharpening of the thermal band. These bands are hereafter called auxiliary bands. First, the Landsat TIR band, which is resampled to 30 m pixels to match the other bands' pixel resolution (United States Geological Survey, 2010), is resampled to its original 60 m resolution, and so are the auxiliary bands, to match its resolution. Then, the now 60 m–auxiliary bands are bicubically upsampled to 30 m, and the *spatial detail* of these pixels, that is, the residue between the two, M_i, was calculated. The same processes was applied to the pixels raised to the power t, calculating $M_{i,t}$. Here, $t = 2$, following Jing and Cheng (2010). With these values, a multiple regression between the upsampled auxiliary bands, the squared upsampled auxiliary bands and the TIR band was established as:

$$M_{\mathrm{TIR}} = \sum_{i=1}^{n} [c_i (M_i)^2 + a_i M_i] + b + e \tag{14}$$

where M_{TIR} is the TIR band (60 m), n is number of auxiliary bands, and here $n = 1, 2, 3, 4$, a_i, b and c_i are the coefficients, calculated by the least squares method, and e is the residual. Finally, the sharpened thermal band is calculated by:

$$M_{\mathrm{TSH}} = M_{\mathrm{TIR}} + \sum_{i=1}^{n} (c_i (M_{i,t} + a_i M_i) \tag{15}$$

where M_{TSH} is the 30 m TIR band. For further information, please refer to Jing and Cheng (2010).

2.3.3. Processing Landsat images

Only Landsat 7 ETM+ T1 images (Tier 1 images, the highest-quality data available, with geometric and radiometric correction) were used. We used Landsat 7 $B6_2$ (*high gain*) thermal band, which has higher radiometric precision than

$B6_1$ (*low gain*) (Chander et al., 2009). First, the Landsat images are clipped to a rectangle containing a reach of the river with the water quality station. Low-quality pixels (due to cloud cover and shading, for example) were removed using the pixel quality band (BQA) with a 30 m buffer around them. The DN (Digital Number) values for each image were transformed into spectral radiance (in W/m^2 sr μm), using values in each image's metadata file, and then to brightness temperature, in K, by inverting Planck's law (Chander et al., 2009). The brightness temperature was only calculated after correcting L_{sensor} in the case of AtmCorr, and after the thermal sharpening when it was applied.

Land and water pixels were classified using MNDWI (Xu, 2006), and a value of emissivity assigned. Surface emissivity strongly influences the estimated temperatures, but it is difficult to be estimated (Sobrino and Raissouni, 2000). For land pixels, the simplified NDVI threshold method (Sobrino et al., 2008) was used, since the land surface temperature is important for the downscaling process. In studies of remote sensing of water bodies, a fixed value of emissivity is commonly employed. Here, water emissivity was fixed at 0.99, as adopted in Okwen et al. (2011), Despini and Teggi (2013), Fricke and Baschek (2015), and Tavares et al. (2019), based on the work of Masuda et al. (1988) and in MODIS Emissivity Library (Zhang, 1999).

The surface temperature was calculated for each Landsat image, and then the resulting image is clipped to a polygon designed for the river stretch (design based on the MNDWI and the NIR band), taking care not to include land–water boundary pixels, which can contaminate the river water estimated temperature due to land pixels, rocks and shadowing from the riparian forest (Handcock et al., 2012). The estimated temperature for the river on each date was taken as the mean temperature of the pixels inside this polygon. Then, the resulting image was composed with Landsat bands 3 and 4 (red and NIR), which was used as input data in SADFAT to estimate RWT, described below.

2.4. Downscaling MODIS images

The MODIS input images to SADFAT algorithm are products MOD11A1 LST, which are daily and have a spatial resolution of 1000 m, and MOD09GA red and NIR (near infrared) reflectance products, which are daily and have a spatial resolution of 250 m. Both products are available directly via NASA's LAADS DAAC page or on demand (available on `https://ladsweb.modaps.eosdis.nasa.gov/search/`), where users can select the products for download, and the images can be reprojected to the desired projection/UTM zone. MODIS Collection 6 products were downloaded and used in this study. As a preliminary selection criteria, the downscaling of MODIS images was only considered when the distance between two consecutive Landsat images was less than 48 days.

The SADFAT algorithm is based on the correlation between the fine-image pixels (*i.e.* Landsat pixels) to classify them in similar or not-similar, separating the coarse-image pixels (*i.e.* MODIS pixels) in homogeneous or heterogeneous. It requires the LST images and information from the band of red and NIR to support this similarity classification, considering that Landsat and MODIS bands are comparable. The flow chart of the downscaling process can be seen in Figure 3.3, where t_m and t_n are the Landsat and MODIS coinciding and subsequent dates, which are the basis for the downscaling of the MODIS images in-between them (t_p). First, the MODIS images are preprocessed: the LST images are resampled to 960 m pixels (in order to contain 32×32 full Landsat pixels) and the MOD09GA bands are resampled to 240 m (in order to contain 8×8 full Landsat pixels), and then cropped to the rectangle containing the river stretch. Then, the images are resampled to 30 m pixels, to match the number of Landsat pixels in the images, and a composition using the 3 bands is made, which is the input data to the algorithm.

The algorithm also depends on the definition of two variables: the number of classes of pixels and the size of the moving window. The former is important in the criterion for selecting similar pixels, and the latter defines how many pixels will be considered in the downscaling process of the central pixel. Although they can influence the resulting quality of the downscaling, little attention is usually given to these parameters. Efforts in this sense are found in the works of Ping et al. (2017), developing an algorithm to select an optimal window size for each step of the STARFM, and Cunha et al. (2019), assessing the impact of different moving window sizes on the resulting error of SADFAT. The studies of Gao et al. (2006) and Zhu et al. (2010) were tested in a boreal forest area, where most pixels were homogeneous; in both works, the moving window size was set as 50×50 Landsat pixels and 4 classes of land cover. Weng et al. (2014) tested SADFAT in a much larger area, over the Los Angeles county, with more land use types; the authors set moving window size as 25×25 Landsat pixels and 5 classes of land use. Here, we considered a window size of 50×50 Landsat pixels, which is thought to improve the results at the expense of more computational time, and 5 classes of land cover.

With all the input data (all the coincident Landsat and MODIS composite images, along with the MOD11 LST images in between), the algorithm is run. It is evaluated pixel by pixel, for every pixel in the images. It starts with

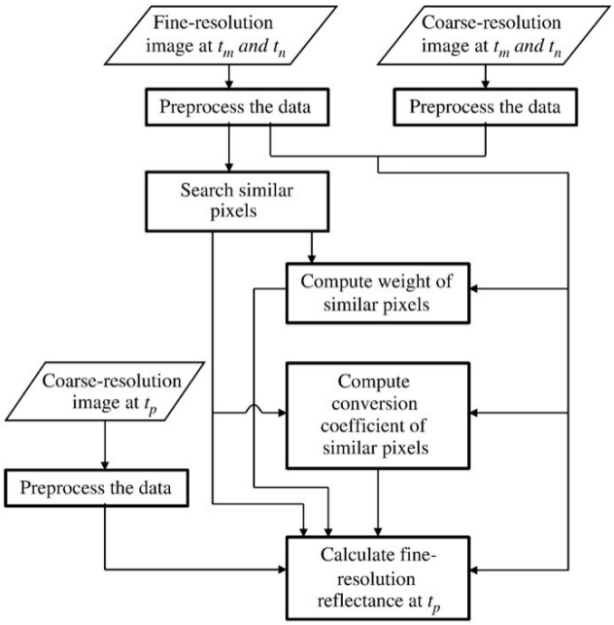

Figure 3.3: Flow chart illustrating the steps of the SADFAT algorithm. (Source: Zhu et al., 2010)

the search of similar pixels inside the moving window in dates t_m and t_n, that depends on the similarity between the central pixel and each pixels, the standard deviation of the pixels inside the moving window, and the number of classes of pixels. Then, considering only the similar pixels, the algorithm calculates a normalised weight W, depending on the distance between the pixels, a conversion coefficient C_t, based on a linear regression, and a temporal weight P_w, based on the difference between the value of each pixel in each date. With these values, the temperature of each pixel in the downscaled MOD11 LST image ins calculated. For more information on the algorithm, please refer to Zhu et al. (2010) and Weng et al. (2014).

2.4.1. RWT selection criteria

There a few limitations in the application of SADFAT for the retrieval of RWT besides those inherent to this application (differences in the the viewing angle and emissivity values, different band specifications, sensitivity and noise level, and differences in overpass times, for example) (Vlassova et al., 2014), namely the great number of missing data in MOD11 images, the fact that the algorithm was not developed with focus on single pixels, but scenes, and chiefly the huge difference between the heat capacity and thermal inertia of water and soil/vegetation, considering that MODIS pixels containing the river are heterogeneous pixels with a mixture of water and different kinds of soil cover, elements that are not taken into account in the downscaling process. The higher accuracy of data fusion algorithms in heterogeneous pixels, and variation of performance according to land cover have already been reported (Hilker et al., 2009; Wu et al., 2015). Due to this, a few criteria were established in order to remove poor-quality (in terms of RWT retrieval accuracy only) downscaled images. First, the temperature was only calculated when there were a least 5 pixels in the river stretch, and the resulting temperature was > 0°C. Second, a criterion was developed based on the air temperature data series (inspired by the stochastic method by Kothandaraman, 1971) and the temperature in selected mixed and pure soil pixels, as shown in Figure 3.4. This criterion was established based on a "estimated" river temperature data series, considering a linear regression between the river temperature data, which was estimated by the Landsat imagery, the temperature in the pure pixel and the mixed pixel in the same date, and the air temperature in the same date, and with a delay of 1 and 2 days. This is given by the equation:

$$T_w(t) = \alpha_1 T_a(t) + \alpha_2 T_a(t-1) + \alpha_3 T_a(t-2) + \alpha_4 T_{pp}(t) + \alpha_5 T_{mp}(t) + \gamma \tag{16}$$

where T_w is the Landsat-derived RWT, T_a is the daily mean air temperature, T_{pp} and T_{mp} are the temperature in the defined MODIS pure and mixed pixels, respectively, and γ and α_n, $n = 1, 2, 3, 4, 5$, are the coefficients of the linear

regression.

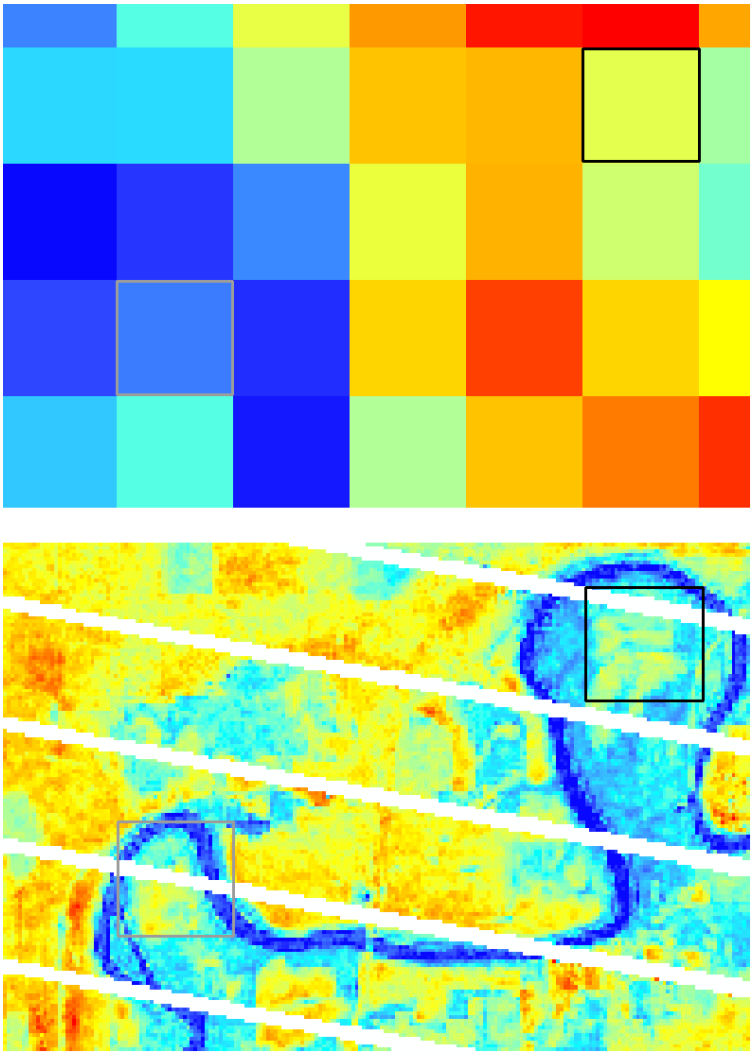

Figure 3.4: Pure soil pixel (black line) and mixed water-soil pixel (grey line) in the study area in Landsat and MODIS LST images, used as basis for the selection criteria of the MODIS-derived RWT.

For each date, the downscaled MODIS-derived RWT was only incorporated in the temperature data series if the difference between this temperature and the value estimated by this linear regression was $\leq 2.5°C$.

3. Results

3.1. Landsat 7 ETM+ derived RWT

Despite the high number of images, only 52 Landsat images could be used to estimate RWT in the 5 years period analysed due to the extensive cloud cover in the region, which is probably related to its closeness to the Great Lakes. In a few cases, the estimated temperature was lower than 0°C, and it was replaced by 0.1°C, when the river was not frozen (visualised in the visible spectra bands). All three methods performed well (Figure 3.5), with good values of metrics (Table 3.2). Additionally, the thermal sharpening technique improved the results of all three methods, reducing bias and absolute error in all cases. AtmCorr and SC-ATC showed the best results, and the latter showed best values of

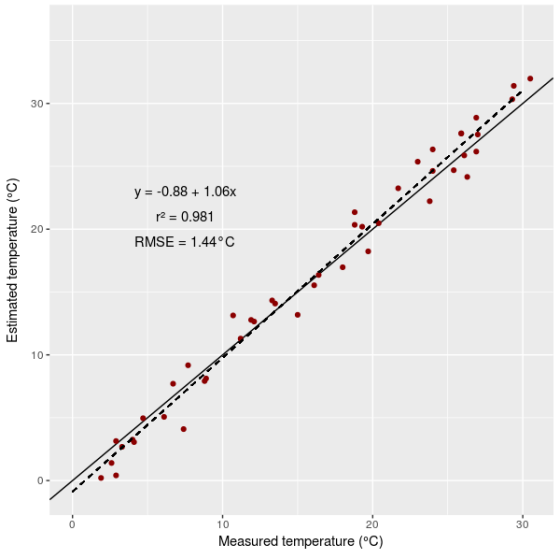

(a) AtmCorr

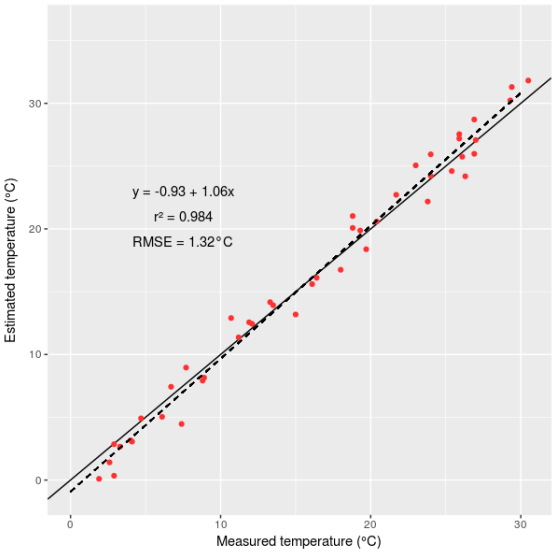

(b) AtmCorr-TSh

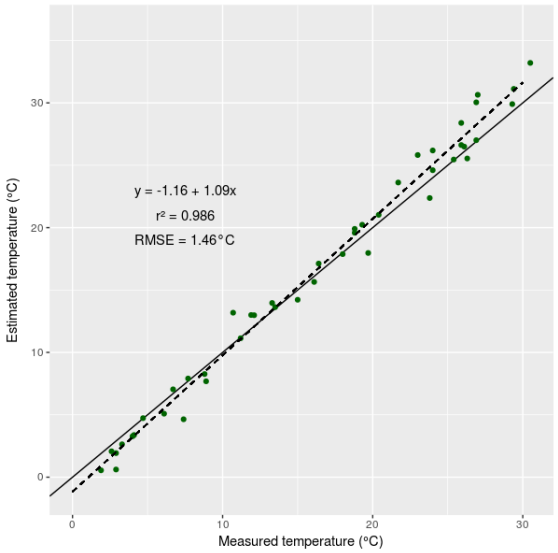

(c) SC-ATC

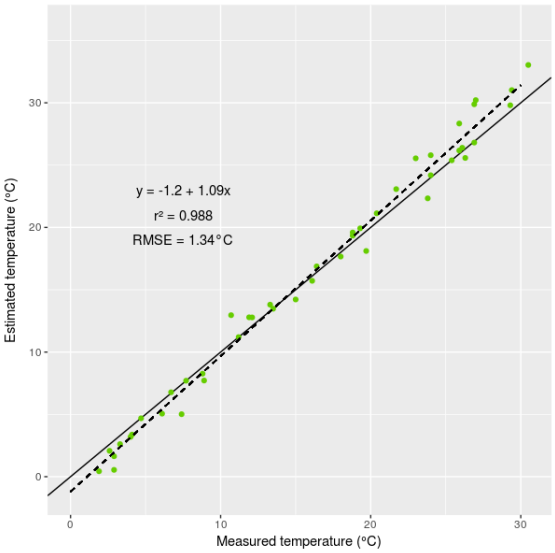

(d) SC-ATC-TSh

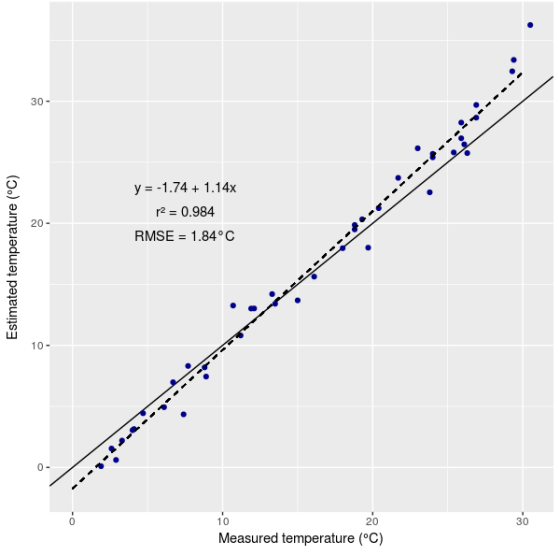

(e) SC-MOD

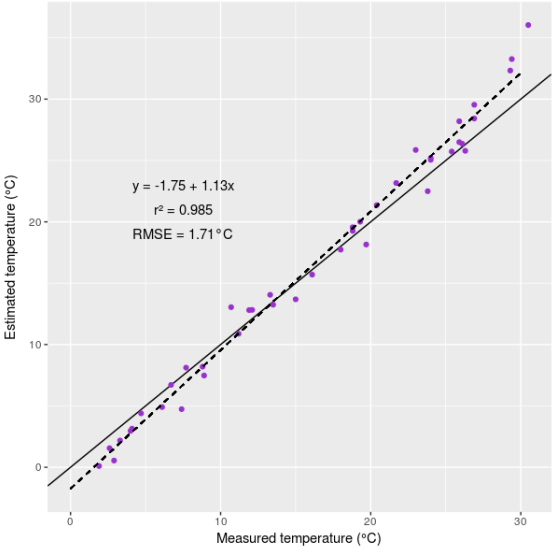

(f) SC-MOD-TSh

Figure 3.5: Comparison of the RWT estimated by each method with *in situ* measured temperatures.

Table 3.2: Metrics calculated for each method of estimating White river's water temperature using Landsat 7 ETM+ imagery.

Method	**Absolute error (°C)**	**Bias (°C)**	**RMSE (°C)**	r^2
AtmCorr	1.22	0.152	1.44	0.981
AtmCorr-TSh	1.11	0.014	1.32	0.984
SC-ATC	1.14	0.334	1.46	0.986
SC-ATC-TSh	1.02	0.199	1.34	0.988
SC-MOD	1.44	0.463	1.84	0.984
SC-MOD-TSh	1.31	0.340	1.71	0.985

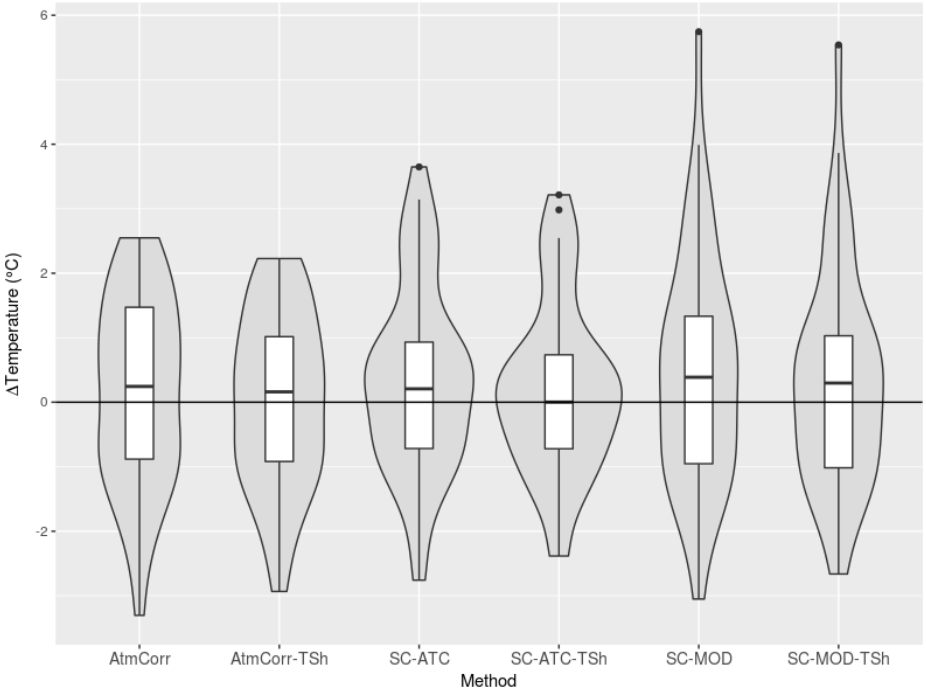

Figure 3.6: Box plot and violin plot of the residuals between the temperatures estimated by each method and the measured temperatures.

absolute error and r^2, but showed more outliers (Figure 3.6), while AtmCorr showed more physically consistent results with best values of bias and RMSE.

A loss of accuracy was found for higher values of water temperature (*i.e.* between 20°C and 30°C), for high levels of water vapour (ranging from 3 up to 6 g/cm^2), and reducing the accuracy of the single-channel algorithm more strongly than the RTE. This reduced accuracy also was seen by Jiménez-Muñoz et al. (2009) and Tavares et al. (2019).

Since the application of the RTE with the atmospheric parameters provided by AtmCorr showed a more robust performance in retrieving RWT from the Landsat images, and the thermal sharpening contributed to improve the accuracy of these estimations, the images resulting from AtmCorr-TSh were used was the input to the downscaling process.

3.2. Downscaled MODIS-derived RWT temperatures

Due to the high number of missing data (in a few cases in the Landsat dates, which impedes the downscaling), there were 205 downscaled MODIS derived RWT temperatures, but only 81 were incorporated in the temperature data series after the selection criteria. While the estimation of a few low accuracy data was expected, the performance of SADFAT was underwhelming (Figure 3.7), with high errors (Table 3.3), both over and underestimating RWT by more than 5°C in some cases, and with a calculated RMSE of 5.41°C. The developed selection criteria performed well in

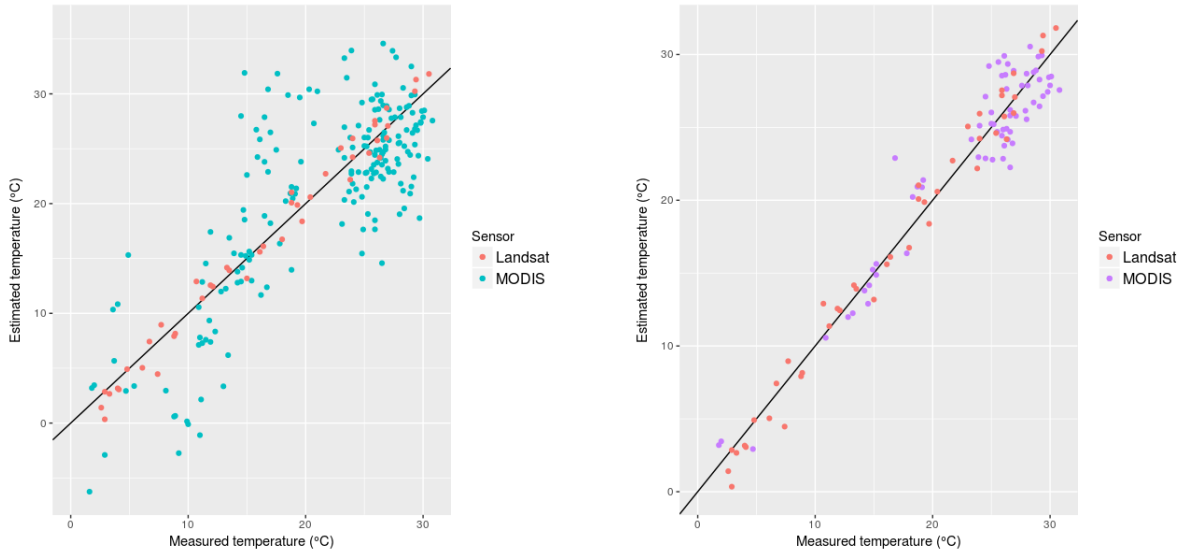

(a) All images

(b) After selection

Figure 3.7: Comparison of the the Landsat-derived RWT and *in situ* measured temperatures with the RWT estimated by downscaled MODIS-images (a) before and (b) after the selection criteria. Note the different axis in each plot.

incorporating only the accurate RWT estimations, improving all metrics, reducing the RMSE to 2.25°C (Table 3.3), for example, although this resulting MODIS-derived RWT still has accuracy below what is desired for river studies.

Table 3.3: Metrics calculated for the RWT derived from Landsat, downscaled MODIS before (BS) and after (AS) the selection criteria, and combined with Landsat.

Method	**Absolute error (°C)**	**Bias (°C)**	**RMSE (°C)**	r^2
Landsat	1.11	0.014	1.32	0.984
MODIS-BS	4.17	-0.346	5.41	0.611
MODIS-AS	1.67	-0.119	2.25	0.909
Combined	1.44	-0.051	2.00	0.956

The combined Landsat and MODIS derived RWT data series has a RMSE of 2°C, substantially above the 1.32°C achieved using Landsat images only, mainly due to a high number of overestimated RWT incorporated in the data series (Figure 3.8), showing a limitation of the selection criteria. However, this accuracy was considered sufficient for this application, especially when considering the limitations of this approach and the accuracy of RWT retrievals in the literature. Thus, both RWT data series (Landsat-derived only, and Landsat and MODIS derived combined) were employed for the calibration of the selected river temperature models.

3.3. River temperature model data series

The stochastic models showed difficulty in the calibration with the low number of RWT data provided by only one calendar year. This was reflected in their poor performance (Table 3.4), and there even was a considerable number of negative water temperatures, during the very low air temperature days (-5°C or less). The inclusion of more data, resulting from the downscale, greatly improved the performance of the stochastic models using the Fourier series, while the impact on the model using the sinusoidal function was only marginal. The series generated using the Fourier series with two harmonics showed a good performance, with RMSE and NSE of 2.31° and 0.931, respectively.

The *air2stream* model showed a consistent performance across the calibrations: RMSE varied from 1.91°C to 1.98°C, and the NSE from 0.948 to 0.952, when using only Landsat-derived RWT, and from 1.88°C to 1.92°C and 0.952 to 0.953, respectively, when using Landsat and MODIS combined. The selected series were chosen based on the

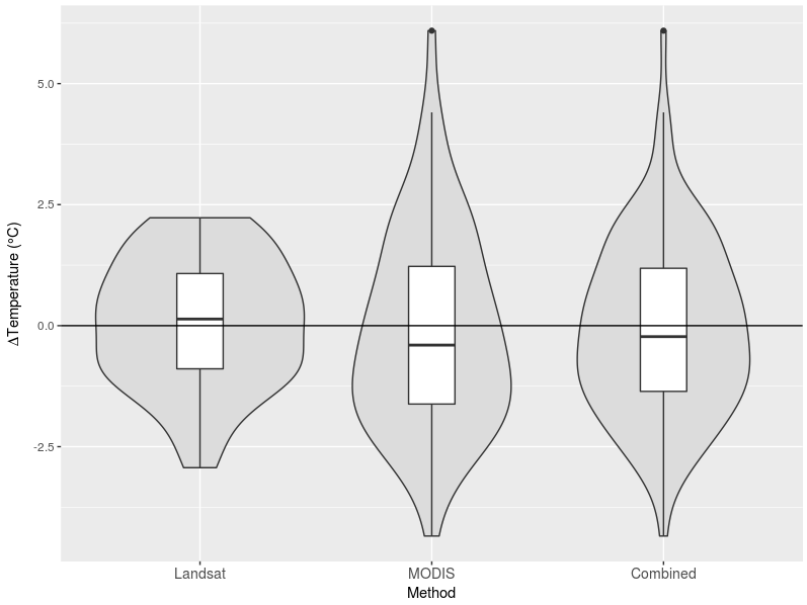

Figure 3.8: Box plot and violin plot of the residuals between temperatures estimated using Landsat images, downscaled MODIS images, and them combined.

Table 3.4: Metrics calculated for each model, calibrated using Landsat (LS) and Landsat with MODIS (MD) images, in estimating White river's water temperature.

Method	**Bias (°C)**	**RMSE (°C)**	**NSE**	r^2
Fourier1h-LS	1.28	4.16	0.775	0.857
Fourier1h-MD	1.51	2.44	0.923	0.959
Fourier2h-LS	1.36	3.88	0.804	0.875
Fourier2h-MD	1.46	2.31	0.931	0.964
Sinusoidal-LS	-2.54	4.23	0.766	0.859
Sinusoidal-MD	-3.34	4.02	0.789	0.943
a2s-LS	0.209	1.91	0.952	0.964
a2s-MD	0.350	1.88	0.953	0.958

metrics calculated in relation to the Landsat-derived RWT, instead of the measured temperatures. The resulting RWT data series were very similar, independent of the inputted calibration data set (Table 3.4), and both performed better than the stochastic models, especially due to the bias of the series, both close to 0°C. A small difference is noted in the residuals of the series (Figure 3.9), with the a2s-MD showing smaller temperature differences for the outliers. A Tukey's honestly significant difference test (post hoc ANOVA) showed that there is a significant difference between the residuals of *air2stream* and all stochastic methods (Table 3.5), but there is not between the residuals of *air2stream* calibrated with the two different RWT data.

4. Discussion

4.1. Landsat-derived temperatures

The results show good values of metrics, especially when compared to the literature (Kay et al., 2005; Wawrzyniak et al., 2012; Fricke and Baschek, 2013, 2015). Despite White river being only 120–170 m wide, that is, less than 180 m wide, the results of all three methods compare really well with those derived by Handcock et al. (2006) in wider rivers, what evidences that these estimations can be made in narrowed water bodies, depending on the pixel arrangement, and

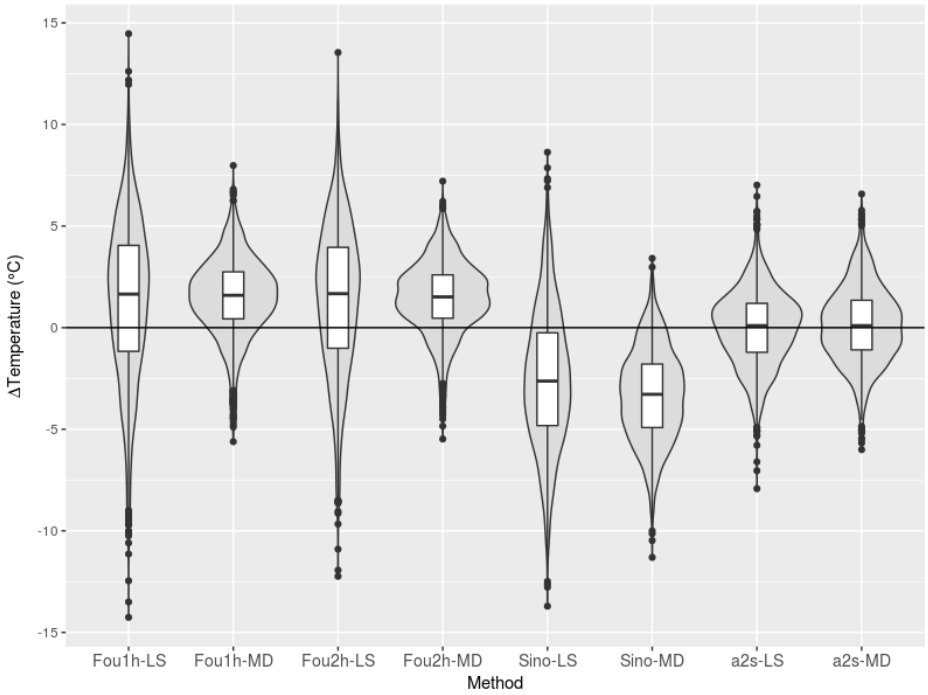

Figure 3.9: Box plot and violin plot of the residuals between the temperatures estimated by each model, with Landsat (LS) and Landsat and MODIS (MD) derived RWT, and the measured temperatures.

even more when combined with a thermal sharpening technique. Even though the algorithm developed by Jing and Cheng (2010) is quite simple and was not developed with a focus in water bodies, it improved the results in all cases (Figure 3.5), and showed how these techniques can and should be applied to increase the accuracy of RWT estimated by Landsat imagery. In this sense, a comparative study of the performance of the available algorithms is still needed, and attempts to develop a robust technique for Landsat images should be encouraged, such as done by Lillo-Saavedra et al. (2018), especially for Landsat 8 TIRS, which consists of two thermal bands with a improved radiometric resolution, in comparison of the previous Landsat missions bands, but with a spatial resolution of 100 m, limiting its application in retrieving accurate water temperature to very wide rivers.

Surprisingly, AtmCorr showed to be a better source of the atmospheric water vapour content than MODIS, which differs from studies comparing them in the literature (Jiménez-Muñoz et al., 2010; Coll et al., 2012; Allan et al., 2016; Tavares et al., 2019), although none compared them in the estimation of river temperatures. So, in the retrieval of RWT from Landsat images, the single-channel algorithm seems to be more sensitive to the water vapour input. When using AtmCorr as the source of the water vapour content, the application of the single-channel algorithm showed better results in most dates (Figure 3.6), but had reduced performance when there was a high water vapour content (Figure 3.10), with an overestimation of temperatures, although the RTE also showed a significant (but not as pronounced) loss of performance in this case. This indicates that, in rivers where there is a lower amplitude of water vapour content, the single-channel algorithm might be more reliable in estimating the water temperature, and should be explored in studies of estimating RWT using Landsat imagery.

Although the processes of estimating lake surface and river water temperature are basically the same, there is higher uncertainty in the latter, resulting in higher errors. Important sources of error in retrieving RWT are the smaller number of pixels, the presence of mixed pixels and other materials on the water surface, such as rocks (Handcock et al., 2012), and the reflection of radiation from adjacent sources, such as vegetation (Anderson and Wilson, 1984; Torgersen et al., 2001). As these effects can hardly be removed from the radiance measured by the sensor, it is best to estimate RWT in a point where these have as lowest influence as possible. Additionally, both estimates of LSWT and RWT depend on an accurate account for the emissivity and atmospheric correction (Jiménez-Muñoz and Sobrino, 2006; Li et al., 2013),

Table 3.5: *p*-value of the Tukey's test between the residuals of each model.

Method	Fou1h-LS	Fou1h-MD	Fou2h-LS	Fou2h-MD	Sino-LS	Sino-MD	a2s-LS	a2s-MD
Fourier1h-LS	NA	0.268	0.992	0.581	<0.01	<0.01	<0.01	<0.01
Fourier1h-MD	0.268	NA	0.791	0.999	<0.01	<0.01	<0.01	<0.01
Fourier2h-LS	0.992	0.791	NA	0.968	<0.01	<0.01	<0.01	<0.01
Fourier2h-MD	0.581	0.999	0.968	NA	<0.01	<0.01	<0.01	<0.01
Sinusoidal-LS	<0.01	<0.01	<0.01	<0.01	NA	<0.01	<0.01	<0.01
Sinusoidal-MD	<0.01	<0.01	<0.01	<0.01	<0.01	NA	<0.01	<0.01
a2s-LS	<0.01	<0.01	<0.01	<0.01	<0.01	<0.01	NA	0.856
a2s-MD	<0.01	<0.01	<0.01	<0.01	<0.01	<0.01	0.856	NA

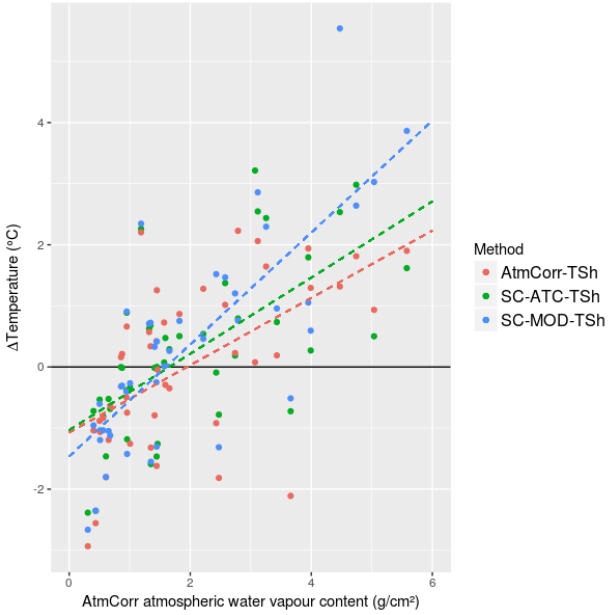

Figure 3.10: Comparison of the residuals found for the estimations of RWT with the atmospheric water vapour content estimated by AtmCorr. The dashed lines represent the linear regression between ΔT and *w* for each method (all three statistically significant).

and are affected by the cool-skin effect (Prats et al., 2018), which is a result of evaporation of water, not affecting the measurements of the water kinetic temperature (*i.e.* thermometer measurements), but reducing the surface radiant temperatures (measured by remote sensors) in 0.1–0.6°C (Robinson et al., 1984), as seen in Figure 3.10.

4.2. Performance of the SADFAT in estimating RWT

The SADFAT underperformed in estimating RWT, and the developed selection criteria proved to be crucial in the incorporation of the MODIS-derived RWT in the data series used for the calibration of the models, greatly reducing all errors. However, the error was still high when compared to the accuracy of the RWT retrieval from Landsat images, which points to limitations not only in the downscaling algorithm, but also in the selection criteria. In fact, our criteria showed a few limitations, such as the aforementioned high number of overestimated RWT incorporated in the data series (Figure 3.8) and a few accurate MODIS-derived RWT that did not attend the criteria, which were most of the time a result of missing data in the mixed or pure soil pixels. Additionally, the linear regression criterion does not take into account variables other than temperature that can be very important for the heating of the surface, such as insolation (Edinger et al., 1968). In sunny days, the surface temperature – especially bare soil, which has a lower emissivity value (Zhang, 1999) – can heat very fast, showing temperatures higher than the air temperatures, which was seen in a few

dates in the Landsat images. These dates might not have been represented in the linear regression, thus misrepresenting the "expected" RWT in such days, even though SADFAT could accurately downscale the LST on those dates.

Furthermore, a few stricter thresholds (*i.e.* the difference of temperature between the linear regression and the MODIS-derived RWT) were also tested, but the results were similar: with a threshold of 2°C, the number of RWT data incorporated in the data series decreased to 70, and bias and RMSE to -0.54°C and 2.15°C, respectively; with a threshold of 1.5°C, this number decreased to 56, and bias and RMSE to -0.098°C and 2.00°C, respectively. Moreover, the choice of the pixels for the selection criteria seems to be important. Although the mixed water-soil pixel was selected for having the highest "concentration" of water inside the MODIS pixel, the amount of soil cover in this pixel was considerably higher (Figure 3.4), and so the difference between the pure soil and the mixed pixel temperatures was minimal most of the time, except in days when there was a sharp variation in air temperatures. For example, in day 10-11-2013 the daily mean air temperature showed a decrease of 4°C, and the difference between these pixels was only 0.44°C. Choosing pixels with a greater temperature difference (which were not found in our scene) could result in a more robust linear regression, thus improving the incorporation of accurate MODIS-derived RWT.

In terms of the limitations of SADFAT, besides the errors that can be a result of both MOD11 and MOD09 products, the errors in the retrieved RWT were higher when there was a sharp (~3°C or more) change in the daily mean air temperature, which cause an underestimation of the RWT in most cases (and causing the observed negative temperatures most of the time). This was expected, as a result of the different thermal inertia of water and other soil cover, as mentioned in Section 2.4.1. The span of days between the two consecutive Landsat images (input of the algorithm) did not show relevance in the process, and the limit of 48 days seems appropriate. For instance, the accuracy of the downscale was better in the images between 19-7-2013 and 5-9-2013 (span of 48 days), when the was a small variation in the air temperatures, than between 1-4-2014 and 17-4-2014 (span of 16 days), when air temperatures varied more.

Additionally, the difference in the RWT between the consecutive Landsat images also seemed to be important. When there was a high difference in the temperatures, the MODIS-derived RWT tended to be overestimated, such as between 17-4-2014 and 4-6-2014, when the difference between the Landsat-derived RWT was 12.02°C, and in most cases the resulting downscaled temperature was 6–10°C hotter than the measured temperatures. On the other hand, between 4-6-2014 and 6-7-2014, the MODIS-derived RWT showed the best accuracy observed for the downscaled images, when the difference between the Landsat-derived RWT was only 1.25°C, and the air temperatures varied less than it is usually observed in this region.

Although being a promising tool to augment the RWT data derived from remote sensing imagery, this complex technique of data fusion is still unable to accurately downscale MODIS surface temperature images to the Landsat resolution at pixel level, when aiming to retrieve temperature of a heterogeneous pixel. Limitations such as the linear relationship between the MODIS and the Landsat pixel temperatures are still to be overcome. Besides, most algorithms to downscale LST are based on a relationship between temperature and NDVI, and with the exception of regression-based downscaling algorithms (Mukherjee et al., 2014), there is a lack of studies comparing different data fusion techniques focusing on the temperature.

4.3. Performance of the models

The *air2stream* model performed better than the stochastic models, especially when comparing them when calibrated using only the Landsat-derived RWT. It is due to the higher complexity of the model (physically-based), but also for using an addition variable (river flow) as input data and a longer data set for calibration. In this sense, testing the impact of the number of years of data selected as calibration period, the model suffers minimal performance loss when using only 2 or 3 year for calibration (Table 3.6), which highlights its consistency.

Both resulting series (LS and MD) of *air2stream* were very similar, which is surprising considering the good performance of the model with little input data. The similar performance of *air2stream* when also using the MODIS-derived RWT (although a bit more erratic when using less years of data for calibration) is likely a result of the reduced accuracy of these data, what shows that the inclusion of a higher number of accurate data per year in the calibration process can improve the results even further. So, considering its complexity and high-data demand, the SADFAT showed to be insufficient to improve the performance of the *air2stream* model in our approach.

Despite the good performance showed by the model, the selected resulting series (Figure 3.11) is still considerably more erratic when compared to the series calibrated using measured temperature data, with a RMSE of 1.28°C, or found in the study by Piccolroaz et al. (2016), using different rivers, finding RMSE of 0.84°C when using *air2stream*

Table 3.6: Metrics calculated for the performance of the *air2stream* model, calibrated using *in situ* measured data (IS), and Landsat (LS) and Landsat with MODIS (MD) images, with different number of years of data for calibration.

Method	**Bias (°C)**	**RMSE (°C)**	**NSE**	r^2
a2s-LS – 4 years	0.209	1.91	0.952	0.964
a2s-LS – 3 years	0.163	1.92	0.951	0.960
a2s-LS – 2 years	0.245	1.95	0.949	0.959
a2s-MD – 4 years	0.350	1.88	0.953	0.958
a2s-MD – 3 years	0.049	2.08	0.949	0.951
a2s-MD – 2 years	0.012	1.97	0.943	0.955
a2s-IS	-0.05	1.28	0.978	0.979

and 1.15°C when using the stochastic model. The inclusion of more data (per year, since the number of years of data did not show significant betterment of performance of the model) for its calibration, using data from different sensors such as Landsat 8 TIRS, can be essential in improving the results for studies aiming at using this tool for assessment of possible impacts of the climate change on rivers. Not only there was a larger variability in the results provided by the model (Figure 3.12), but the model also tends to underestimate low temperatures and overestimate high temperatures, which is a problem for such studies. This is a result of the bias in the estimations of the temperatures in the retrieval of RWT from the Landsat images (Figure 3.5), and so it is a limitation of this approach. There is difficulty in estimating high temperatures with good accuracy due to the relation between temperature and water vapour content, and in high water vapour contents the RWT were overestimated by all three methods applied here (Figure 3.10).

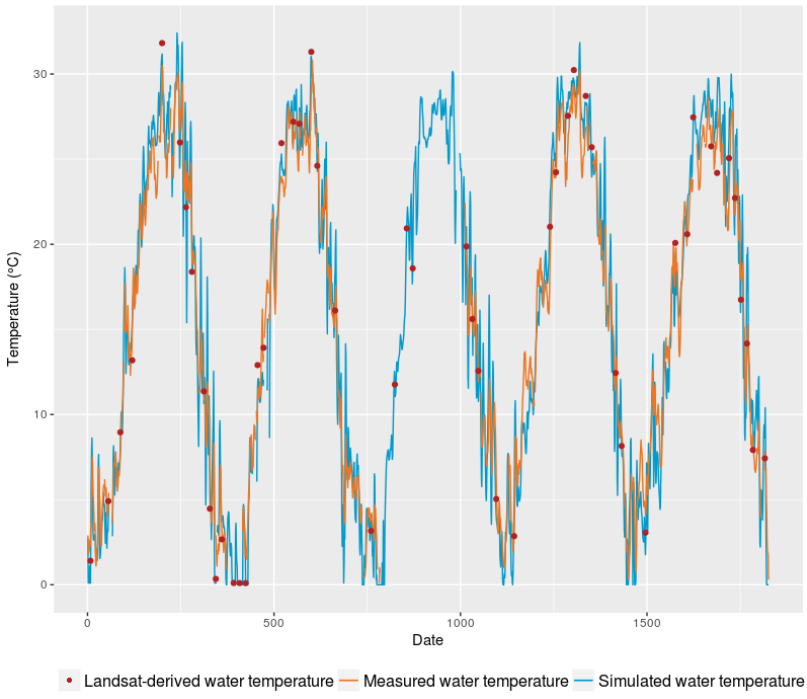

Figure 3.11: Comparison of the best performing RWT data series modelled by *air2stream* with the *in situ* measured data and the Landsat-derived RWT during the study period.

However, despite its observed limitations, this approach seems promising in generating consistent, continuous RWT for rivers with no measured data, with the temperature being estimated using Landsat 7 ETM+ imagery, which has a good spatial resolution (60 m, that can be enhanced to 30 m using thermal sharpening) and a long time series of images (starting in 1999), while the river flow can be modelled using a rainfall-runoff model, for example. In our test, with a

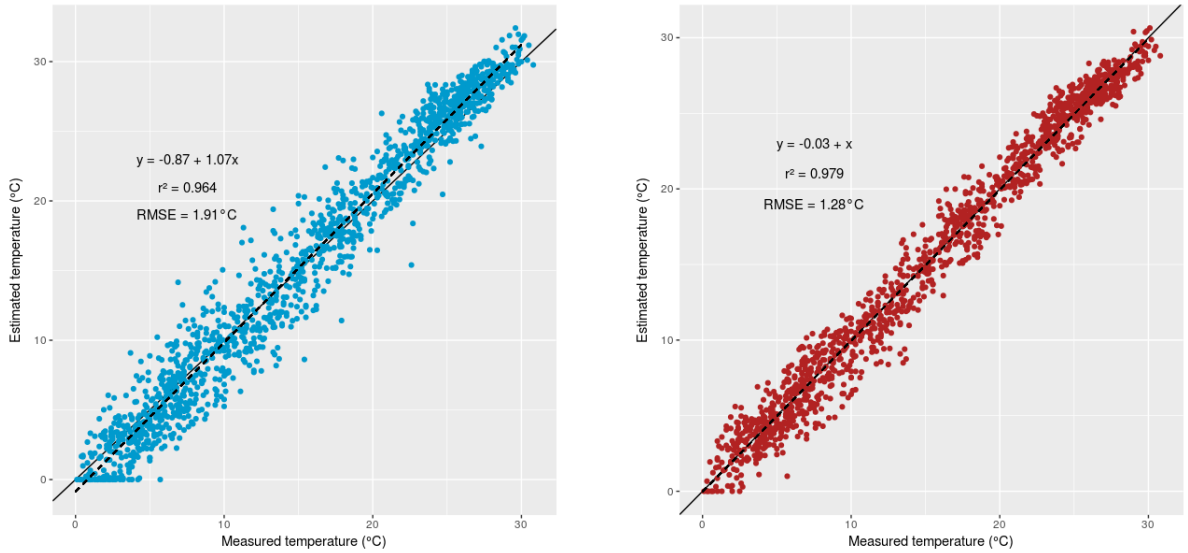

(a) Landsat-derived RWT data

(b) measured RWT data

Figure 3.12: Comparison of the measured RWT data with the RWT data series modelled by *air2stream*, when calibrated with **(a)** the Landsat-derived RWT and **(b)** the measured data.

RMSE of 1.91°C and 80% of the data being in a window of ±2.5°C from the actual temperature (the 10% and 90% percentiles of the temperature difference were -2.29°C and 2.50°C, respectively) (Figure 3.9), the temperature of White river was successfully modelled, and this approach has the potential to analyse trends in river temperatures, to be used in modelling tributary temperatures, as input of ecological models, and with improvements in the limitations of this approach, it can also be used in studies of impacts of climate change in the temperature of rivers.

5. Conclusions

In this study, we tested an approach of calibrating river temperature models using river water temperature derived from remote sensing imagery in the White river, in Indiana, USA. In the first part, we tested three different methods of estimating RWT from Landsat 7 ETM+ images (Barsi et al., 2003b; Jiménez-Muñoz and Sobrino, 2003), combined with a technique of thermal sharpening (Jing and Cheng, 2010). These methods showed bias and RMSE of 0.152–0.463°C and 1.44–1.84°C, respectively, and the thermal sharpening improved the accuracy of the results, with bias and RMSE of 0.014–0.340°C and 1.32–1.71°C, respectively (Table 3.2). The best results were found for AtmCorr, which compared well with the few available studies found in the literature. An underestimation and overestimation of the temperatures was observed in days with very low and very high atmospheric water vapour content, respectively.

Secondly, we tested the application of a data fusion model, SADFAT (Weng et al., 2014), to downscale MODIS product MOD11 LST to the Landsat spatial resolution and retrieve daily RWT data. Due to the limitations of this model, mainly the downscale of single pixels, which was not tested yet, and the difference between the thermal inertia of water and soil/vegetation, soil covers that are mixed in the MODIS pixels, we developed a selection criteria, based on the air temperature data series and the temperature in mixed water/soil and in the pure soil pixel, for the incoporation of the accurate RWT data only. The data fusion model showed a poor performance, with RMSE of 5.41°C, over and underestimating RWT by more than 5°C in several dates (Table 3.3). The selection criteria greatly improved the accuracy of the MODIS-derived RWT data series, reducing RMSE to 2.25°C, although there were a few overestimated RWT incorporated in the data series (Figure 3.8), and the rejection of some accurate MODIS-derived RWT. By merging this resulting series with the Landsat-derived RWT, the combined RMSE was 2°C, considerably higher than the original series. This highlight the limitations of this algorithm, and the lack of data fusion models focusing on downscaling water temperatures.

Thirdly, we tested the calibration of three versions of a stochastic model (Caissie et al., 1998) and a hybrid model (Toffolon and Piccolroaz, 2015) with these two RWT data series. The *air2stream* model outperformed the stochastic models, with RMSE of 1.91°C, when calibrated with Landsat data, and 1.88°C when calibrated with Landsat and MODIS data combined (Table 3.4). Considering its complexity, long computational time and high demand of input data (and the related preprocessing of this data), the inclusion of the downscaled MODIS data had very little impact on the performance of *air2stream*. The model was also very consistent in generating the temperature data series, with little loss of performance when reducing the number of years of data for calibration (Table 3.6). The limitations of this approach were a high variability of the resulting RWT data series, and the underestimation of low temperatures and overestimation of high temperatures (Figure 3.12), which hinders the application of this approach in studies of future impacts of the climate change. But considering the low number of input data of its calibration, the model showed a great performance, generating a consistent, continuous RWT data series, and can be applied in many studies in rivers with no measured *in situ* water temperature data, such as analysing past and present trends in river temperatures, and in modelling tributary temperatures for ecological models.

We recommend tests of the accuracy of the Landsat-derived water temperatures in other rivers, as there is limited studies in this subject, further tests of the performance of the *air2stream* model calibrated with RWT derived from remote sensing, with the inclusion of data derived from other sensors, such as Landsat 8 TIRS and encourage the development of thermal sharpening techniques and data fusion models focusing on water resources, taking advantage of the recent launching of the Sentinel-3 program, in a way to improve the temporal resolution and the accuracy of retrievals of river water temperatures from remote sensing imagery, efforts that are necessary for the development of a open global database of surface temperatures.

Acknowledgements

We would like to thank CNPq and CAPES for the funding, the United States Geological Service for making the Landsat images and river data freely available, via Earth Explorer and the National Real-Time Water Quality platforms, NASA for making the MODIS images freely available via Earth Data platform, and for curating AtmCorr, Marco Toffolon and Sebastiano Piccolroaz for making the *air2stream* model freely available, Peng Fu for kindly handing the SADFAT script written in MATLAB, Julia Barsi from NASA for curating and helping with automating AtmCorr data download, and the Global Lake Ecological Observatory Network (GLEON) for providing resources and a venue for the discussion on lakes.

References

Agam, N., Kustas, W. P., Anderson, M. C., Li, F., and Neale, C. M. (2007). A vegetation index based technique for spatial sharpening of thermal imagery. Remote Sensing of Environment, 107(4):545–558.

Allan, J. D. and Castillo, M. M. (2007). Stream ecology: structure and function of running waters. Springer Science & Business Media.

Allan, M. G., Hamilton, D. P., Trolle, D., Muraoka, K., and McBride, C. (2016). Spatial heterogeneity in geothermally-influenced lakes derived from atmospherically corrected Landsat thermal imagery and three-dimensional hydrodynamic modelling. International Journal of Applied Earth Observation and Geoinformation, 50:106–116.

Anderson, J. and Wilson, S. (1984). The physical basis of current infrared remote-sensing techniques and the interpretation of data from aerial surveys. International Journal of Remote Sensing, 5(1):1–18.

Barsi, J. A., Barker, J. L., and Schott, J. R. (2003a). An atmospheric correction parameter calculator for a single thermal band earth-sensing instrument. In Proceedings of the 2003 IEEE Geoscience and Remote Sensing Symposium (IGARSS'03), volume 5, pages 3014–3016.

Barsi, J. A., Schott, J., Palluconi, F. D., Helder, D. L., Hook, S. J., Markham, B. L., Chander, G., and O'Donnell, E. M. (2003b). Landsat TM and ETM+ thermal band calibration. Canadian Journal of Remote Sensing, 29(2):141–153.

Barsi, J. A., Schott, J., Palluconi, F. D., and Hook, S. J. (2005). Validation of a web-based atmospheric correction tool for single thermal band instruments. In Earth Observing Systems X, volume 5882, page 58820E. International Society for Optics and Photonics.

Bivand, R., Keitt, T., and Rowlingson, B. (2018). rgdal: Bindings for the 'Geospatial' Data Abstraction Library. R package version 1.2-15.

Bivand, R. and Lewin-Koh, N. (2017). maptools: Tools for Reading and Handling Spatial Objects. R package version 0.9-2.

Bivand, R. and Rundel, C. (2017). rgeos: Interface to Geometry Engine - Open Source ('GEOS'). R package version 0.3-26.

Cai, H., Piccolroaz, S., Huang, J., Liu, Z., Liu, F., and Toffolon, M. (2018). Quantifying the impact of the Three Gorges Dam on the thermal dynamics of the Yangtze River. Environmental Research Letters, 13(5):054016.

Caissie, D. (2006). The thermal regime of rivers: a review. Freshwater Biology, 51(8):1389–1406.

Caissie, D., El-Jabi, N., and Satish, M. G. (2001). Modelling of maximum daily water temperatures in a small stream using air temperature. Journal of Hydrology, 251(1–2):14–28.

Caissie, D., El-Jabi, N., and St-Hilaire, A. (1998). Stochastic modelling of water temperatures in a small stream using air to water relations. Canadian Journal of Civil Engineering, 25(2):250–260.

Caissie, D., Satish, M. G., and El-Jabi, N. (2005). Predicting river water temperatures using the equilibrium temperature concept with application on Miramichi River catchments (New Brunswick, Canada). Hydrological Processes, 19(11):2137–2159.

Chander, G., Markham, B. L., and Helder, D. L. (2009). Summary of current radiometric calibration coefficients for Landsat MSS, TM, ETM+, and EO-1 ALI sensors. Remote Sensing of Environment, 113:893–903.

Cherkauer, K. A., Burges, S. J., Handcock, R. N., Kay, J. E., Kampf, S. K., and Gillespie, A. R. (2005). Assessing satellite-based and aircraft-based thermal infrared remote sensing for monitoring Pacific Northwest river temperature. Journal of the American Water Resources Association, 41(5):1149–1159.

Cluis, D. A. (1972). Relationship between stream water temperature and ambient air temperature – a simple autoregressive model for mean daily stream water temperature fluctuations. Nordic Hydrology, 3:65–71.

Coll, C., Caselles, V., Valor, E., and Niclòs, R. (2012). Comparison between different sources of atmospheric profiles for land surface temperature retrieval from single channel thermal infrared data. Remote Sensing of Environment, 117:199–210.

Crisp, D. T. and Howson, G. (1982). Effect of air temperature upon mean water temperature in streams in the north Pennines and English Lake District. Freshwater Biology, 12(4):359–367.

Cristea, N. C. and Burges, S. J. (2009). Use of thermal infrared imagery to complement monitoring and modeling of spatial stream temperatures. Journal of Hydrologic Engineering, 14(10):1080–1090.

Cristóbal, J., Jiménez-Muñoz, J. C., Sobrino, J. A., Ninyerola, M., and Pons, X. (2009). Improvements in land surface temperature retrieval from the Landsat series thermal band using water vapor and air temperature. Journal of Geophysical Research, 114:D08103.

Crosman, E. T. and Horel, J. D. (2009). MODIS-derived surface temperature of the Great Salt Lake. Remote Sensing of Environment, 113(1):73–81.

Cunha, A. H. F., Tavares, M. H., Moura, B. M. N. D., González Avila, I., Nascimento, G. S., Cavalcanti, J. R., Souza, A. P. M., Ruhoff, A. L., Fragoso Jr., C. R., and Motta-Marques, D. (2019). Avaliação de abordagem para downscale de temperatura de brilho de imagens MODIS e sensibilidade da janela de movimento: aplicação em sistema estuarino lagunar tropical. In Proceedings of the XIX Brazilian Symposium of Remote Sensing, Santos, Brazil.

Despini, F. and Teggi, S. (2013). Analysis of temperature maps of waterbodies obtained from ASTER TIR images. International Journal of Remote Sensing, 34(9–10):3636–3653.

Dugdale, S. J., Hannah, D. M., and Malcolm, I. A. (2017). River temperature modelling: A review of process-based approaches and future directions. Earth-Science Reviews, 175:97–113.

Dugdale, S. J., Malcolm, I. A., Kantola, K., and Hannah, D. M. (2018). Stream temperature under contrasting riparian forest cover: Understanding thermal dynamics and heat exchange processes. Science of the Total Environment, 610–611:1375–1389.

Díaz-Delgado, R., Ameztoy, I., Cristóbal, J., and Bustamante, J. (2010). Long time series of Landsat images to reconstruct river surface temperature and turbidity regimes of Guadalquivir Estuary. In Proceedings of the 2010 IEEE Geoscience and Remote Sensing Symposium (IGARSS'10), pages 233–236.

Edinger, J. E., Duttweiler, D. W., and Geyer, J. C. (1968). The response of water temperatures to meteorological condition. Water Resources Research, 4(5):1137–1143.

Fenocchi, A., Rogora, M., Sibilla, S., and Dresti, C. (2017). Relevance of inflows on the thermodynamic structure and on the modeling of a deep subalpine lake (Lake Maggiore, Northern Italy/Southern Switzerland). Limnologica, 63:42–56.

Fricke, K. and Baschek, B. (2013). Water surface temperature profiles for the Rhine river derived from Landsat ETM+ data. In Proceedings of SPIE 8887, Remote Sensing for Agriculture, Ecosystems, and Hydrology XV, page 88870E.

Fricke, K. and Baschek, B. (2015). Temperature monitoring along the Rhine river based on airborne thermal infrared remote sensing: estimation of in situ water temperatures and inflow detection compared to artificial satellite data. Journal of Applied Remote Sensing, 9(1):095067.

Fu, P. and Weng, Q. (2016). A time series analysis of urbanization induced land use and land cover change and its impact on land surface temperature with Landsat imagery. Remote Sensing of Environment, 175:205–214.

Gao, F., Masek, J., Schwaller, M., and Hall, F. (2006). On the blending of the Landsat and MODIS surface reflectance: predicting daily Landsat surface reflectance. IEEE Transactions on Geoscience, 44(8):2207–2218.

Gu, R., Montgomery, S., and Austin, R. A. (1998). Quantifying the effects of stream discharge on summer river temperature. Hydrological Sciences Journal, 43(6):885–904.

Handcock, R., Gillespie, A., Cherkauer, K., Kay, J., Burges, S., and Kampf, S. (2006). Accuracy and uncertainty of thermal-infrared remote sensing of stream temperatures at multiple spatial scales. Remote Sensing of Environment, 100(4):427–440.

Handcock, R. N., Torgersen, C. E., Cherkauer, K. A., Gillespie, A. R., Tockner, K., Faux, R. N., and Tan, J. (2012). Thermal infrared remote sensing of water temperature in riverine landscapes. Fluvial Remote Sensing for Science and Management, 12:85–113.

Hijmans, R. J. (2017). raster: Geographic Data Analysis and Modeling. R package version 2.6-7.

Hilker, T., Wulder, M. A., Coops, N. C., Linke, J., McDermid, G., Masek, J. G., Gao, F., and White, J. C. (2009). A new data fusion model for high spatial- and temporal-resolution mapping of forest disturbance based on Landsat and MODIS. Remote Sensing of Environment, 113(8):1613–1627.

Jackson, F. L., Fryer, R. J., Hannah, D. M., Millar, C. P., and Malcolm, I. A. (2018). A spatio-temporal statistical model of maximum daily river temperatures to inform the management of Scotland's Atlantic salmon rivers under climate change. Science of the Total Environment, 612:1543–1558.

Jiménez-Muñoz, J. and Sobrino, J. (2006). Error sources on the land surface temperature retrieved from thermal infrared single channel remote sensing data. International Journal of Remote Sensing, 27(05):999–1014.

Jiménez-Muñoz, J. C., Cristobal, J., Sobrino, J. A., Soria, G., Ninyerola, M., Pons, X., and Pons, X. (2009). Revision of the single-channel algorithm for land surface temperature retrieval from Landsat thermal-infrared data. IEEE Transactions on Geoscience and Remote Sensing, 47(1):339–349.

Jiménez-Muñoz, J. C. and Sobrino, J. A. (2003). A generalized single-channel method for retrieving land surface temperature from remote sensing data. Journal of Geophysical Research, 108:D22.

Jiménez-Muñoz, J. C., Sobrino, J. A., Mattar, C., and Franch, B. (2010). Atmospheric correction of optical imagery from MODIS and Reanalysis atmospheric products. Remote Sensing of Environment, 114(10):2195–2210.

Jing, L. and Cheng, Q. (2010). A technique based on non-linear transform and multivariate analysis to merge thermal infrared data and higher-resolution multispectral data. International Journal of Remote Sensing, 31(24):6459–6471.

Kay, J. E., Kampf, S. K., Handcock, R. N., Cherkauer, K. A., Gillespie, A. R., and Burges, S. J. (2005). Accuracy of lake and stream temperatures estimated from thermal infrared images. JAWRA Journal of the American Water Resources Association, 41(5):1161–1175.

Kothandaraman, V. (1971). Analysis of water temperature variations in large rivers. Journal of the Sanitary Engineering Division, 97:19–31.

Kottek, M., Grieser, J., Beck, C., Rudolf, B., and Rubel, F. (2006). World map of the Köppen-Geiger climate classification updated. Meteorologische Zeitschrift, 15(3):259–263.

Lamaro, A. A., Mariñelarena, A., Torrusio, S. E., and Sala, S. E. (2013). Water surface temperature estimation from Landsat 7 ETM+ thermal infrared data using the generalized single-channel method: Case study of Embalse del Río Tercero (Córdoba, Argentina). Advances in Space Research, 51(3):492–500.

Li, Z.-L., Tang, B.-H., Wu, H., Ren, H., Yan, G., Wan, Z., Trigo, I. F., and Sobrino, J. A. (2013). Satellite-derived land surface temperature: Current status and perspectives. Remote Sensing of Environment, 131:14–37.

Lillo-Saavedra, M., García-Pedrero, A., Merino, G., and Gonzalo-Martín, C. (2018). TS^{2}uRF: A new method for sharpening thermal infrared satellite imagery. Remote Sensing, 10(2):249.

Ling, F., Foody, G. M., Du, H., Ban, X., Li, X., Zhang, Y., and Du, Y. (2017). Monitoring thermal pollution in rivers downstream of dams with Landsat ETM+ thermal infrared images. Remote Sensing, 9(11):1175.

Marruedo Arricibita, A. I., Dugdale, S. J., Krause, S., Hannah, D. M., and Lewandowski, J. (2018). Thermal infrared imaging for the detection of relatively warm lacustrine groundwater discharge at the surface of freshwater bodies. Journal of Hydrology, 562:281–289.

Masuda, K., Takashima, T., and Takayama, Y. (1988). Emissivity of pure and sea waters for the model sea surface in the infrared window regions. Remote Sensing of Environment, 24(2):313–329.

Mohseni, O., Erickson, T. R., and Stefan, H. G. (1999). Sensitivity of stream temperatures in the United States to air temperatures projected under a global warming scenario. Water Resources Research, 35(12):3723–3733.

Mohseni, O. and Stefan, H. G. (1999). Stream temperature/air temperature relationship: a physical interpretation. Journal of Hydrology, 218(3–4):128–141.

Mukherjee, S., Joshi, P., and Garg, R. (2014). A comparison of different regression models for downscaling Landsat and MODIS land surface temperature images over heterogeneous landscape. Advances in Space Research, 54(4):655–669.

Okwen, R., Pu, R., and Cunningham, J. (2011). Remote sensing of temperature variations around major power plants as point sources of heat. International Journal of Remote Sensing, 32(13):3791–3805.

Orr, H. G., Johnson, M. F., Wilby, R. L., Hatton-Ellis, T., and Broadmeadow, S. (2015). What else do managers need to know about warming rivers? A United Kingdom perspective. Wiley Interdisciplinary Reviews: Water, 2(2):55–64.

Pahlevan, N., Gerace, A. D., and Schott, J. R. (2011). Using thermal remote sensing as a tool for calibrating a hydrodynamic model in inland waters. In Proceedings of SPIE 8030, Ocean Sensing and Monitoring III, 80300I.

Pebesma, E. J. and Bivand, R. S. (2005). Classes and methods for spatial data in R. R News, 5(2):9–13.

Piccolroaz, S., Calamita, E., Majone, B., Gallice, A., Siviglia, A., and Toffolon, M. (2016). Prediction of river water temperature: a comparison between a new family of hybrid models and statistical approaches. Hydrological Processes, 30(21):3901–3917.

Piccolroaz, S., Healey, N., Lenters, J., Schladow, S., Hook, S., Sahoo, G., and Toffolon, M. (2018). On the predictability of lake surface temperature using air temperature in a changing climate: A case study for Lake Tahoe (USA). Limnology and Oceanography, 63(1):243–261.

Piccolroaz, S., Toffolon, M., and Majone, B. (2013). A simple lumped model to convert air temperature into surface water temperature in lakes. Hydrology and Earth System Sciences, 17:3323–3338.

Ping, B., Meng, Y., and Su, F. (2017). An enhanced spatial and temporal adaptive reflectance fusion model based on optimal window. In Proceedings of the 2017 IEEE Geoscience and Remote Sensing Symposium (IGARSS'17), pages 3377–3380.

Piotrowski, A. P. and Napiorkowski, J. J. (2018). Performance of the air2stream model that relates air and stream water temperatures depends on the calibration method. Journal of Hydrology, 561:395–412.

Prats, J., Reynaud, N., Rebière, D., Peroux, T., Tormos, T., and Danis, P.-A. (2018). LakeSST: Lake Skin Surface Temperature in French inland water bodies for 1999–2016 from Landsat archives. Earth System Science Data, 10(2):727–743.

R Core Team (2018). R: A Language and Environment for Statistical Computing. R Foundation for Statistical Computing, Vienna, Austria.

Robinson, I., Wells, N., and Charnock, H. (1984). The sea surface thermal boundary layer and its relevance to the measurement of sea surface temperature by airborne and spaceborne radiometers. International Journal of Remote Sensing, 5(1):19–45.

Rodriguez-Galiano, V., Pardo-Igúzquiza, E., Sanchez-Castillo, M., Chica-Olmo, M., and Chica-Rivas, M. (2012). Downscaling Landsat 7 ETM+ thermal imagery using land surface temperature and NDVI images. International Journal of Applied Earth Observation and Geoinformation, 18:515–527.

Ruesch, A. S., Torgersen, C. E., Lawler, J. J., Olden, J. D., Peterson, E. E., Volk, C. J., and Lawrence, D. J. (2012). Projected climate-induced habitat loss for salmonids in the John Day River Network, Oregon, USA. Conservation Biology, 26(5):873–882.

Sahoo, G. B., Schladow, S. G., and Reuter, J. E. (2009). Forecasting stream water temperature using regression analysis, artificial neural network, and chaotic non-linear dynamic models. Journal of Hydrology, 378(3–4):325–342.

Schott, J. R. (2007). Remote sensing: the image chain approach. Oxford University Press; 2nd edition.

Schwarz, N., Lautenbach, S., and Seppelt, R. (2011). Exploring indicators for quantifying surface urban heat islands of European cities with MODIS land surface temperatures. Remote Sensing of Environment, 115(12):3175–3186.

Simon, R., Tormos, T., and Danis, P.-A. (2014). Retrieving water surface temperature from archive LANDSAT thermal infrared data: Application of the mono-channel atmospheric correction algorithm over two freshwater reservoirs. International Journal of Applied Earth Observation and Geoinformation, 30:247–250.

Sinokrot, B. A. and Stefan, H. G. (1993). Stream temperature dynamics: measurements and modeling. Water Resources Research, 29(7):2299–2312.

Sinokrot, B. A., Stefan, H. G., McCormick, J. H., and Eaton, J. G. (1995). Modeling of climate change effects on stream temperatures and fish

habitats below dams and near groundwater inputs. Climatic Change, 30(2):181–200.
Sobrino, J. A., Jiménez-Muñoz, J. C., Soria, G., Romaguera, M., Guanter, L., Moreno, J., Plaza, A., and Martinez, P. (2008). Land surface emissivity retrieval from different VNIR and TIR sensors. IEEE Transactions on Geoscience and Remote Sensing, 46(2):316–327.
Sobrino, J. A. and Raissouni, N. (2000). Toward remote sensing methods for land cover dynamic monitoring: Application to Morocco. International Journal of Remote Sensing, 21(2):353–366.
Stefan, H. G. and Preud'homme, E. B. (1993). Stream temperature estimation from air temperature. Journal of the American Water Resources Association, 29(1):27–45.
Tavares, M. H., Cunha, A. H. F., Motta-Marques, D., Ruhoff, A. L., Cavalcanti, J. R., Fragoso Jr, C. R., Martín Bravo, J., Munar, A. M., Fan, F. M., and Rodrigues, L. H. R. (2019). Comparison of methods to estimate lake-surface-water temperature using Landsat 7 ETM+ and MODIS imagery: case study of a large shallow subtropical lake in Southern Brazil. Water, 11(1):168.
Teggi, S. (2012). A technique for spatial sharpening of thermal imagery of coastal waters and of watercourses. International Journal of Remote Sensing, 33(10):3063–3089.
Toffolon, M. and Piccolroaz, S. (2015). A hybrid model for river water temperature as a function of air temperature and discharge. Environmental Research Letters, 10:114011.
Torgersen, C. E., Faux, R. N., McIntosh, B. A., Poage, N. J., and Norton, D. J. (2001). Airborne thermal remote sensing for water temperature assessment in rivers and streams. Remote Sensing of Environment, 76(3):386–398.
United States Geological Survey (2010). Landsat update: new thermal band resampling: 30-meter pixels. Volume 4, Issue 1. `https://landsat.usgs.gov/sites/default/files/documents/2010_Landsat_Updates.pdf`.
van Vliet, M. T. H., Franssen, W. H. P., Yearsley, J. R., Ludwig, F., Haddeland, I., Lettenmaier, D. P., and Kabat, P. (2013). Global river discharge and water temperature under climate change. Global Environmental Change, 23(2):450–464.
Vancutsem, C., Ceccato, P., Dinku, T., and Connor, S. J. (2010). Evaluation of MODIS land surface temperature data to estimate air temperature in different ecosystems over Africa. Remote Sensing of Environment, 114(2):449–465.
Vatland, S. J., Gresswell, R. E., and Poole, G. C. (2015). Quantifying stream thermal regimes at multiple scales: Combining thermal infrared imagery and stationary stream temperature data in a novel modeling framework. Water Resources Research, 51:31–46.
Vinnå, L. R., Wüest, A., Zappa, M., Fink, G., and Bouffard, D. (2017). Tributaries affect the thermal response of lakes to climate change. Hydrology and Earth System Sciences, 22(1):31.
Vlassova, L., Perez-Cabello, F., Nieto, H., Martín, P., Riaño, D., and de la Riva, J. (2014). Assessment of methods for land surface temperature retrieval from Landsat-5 TM images applicable to multiscale tree-grass ecosystem modeling. Remote Sensing, 6(5):4345–4368.
Wawrzyniak, V., Piégay, H., Allemand, P., Vaudor, L., and Grandjean, P. (2013). Prediction of water temperature heterogeneity of braided rivers using very high resolution thermal infrared (TIR) images. International Journal of Remote Sensing, 34(13):4812–4831.
Wawrzyniak, V., Piégay, H., and Poirel, A. (2012). Longitudinal and temporal thermal patterns of the French Rhône River using Landsat ETM+ thermal infrared images. Aquatic sciences, 74(3):405–414.
Webb, B. W., Hannah, D. M., Moore, R. D., Brown, L. E., and Nobilis, F. (2008). Recent advances in stream and river temperature research. Hydrological Processes, 22:902–918.
Weng, Q., Fu, P., and Gao, F. (2014). Generating daily land surface temperature at Landsat resolution by fusing Landsat and MODIS data. Remote Sensing of Environment, 145:55–67.
Woltemade, C. and Hawkins, T. (2016). Stream temperature impacts because of changes in air temperature, land cover and stream discharge: Navarro River watershed, California, USA. River Research and Applications, 32(10):2020–2031.
Wu, P., Shen, H., Zhang, L., and Göttsche, F.-M. (2015). Integrated fusion of multi-scale polar-orbiting and geostationary satellite observations for the mapping of high spatial and temporal resolution land surface temperature. Remote Sensing of Environment, 156:169–181.
Xu, H. (2006). Modification of normalised difference water index (NDWI) to enhance open water features in remotely sensed imagery. International Journal of Remote Sensing, 27(14):3025–3033.
Zhan, W., Chen, Y., Zhou, J., Wang, J., Liu, W., Voogt, J., Zhu, X., Quan, J., and Li, J. (2013). Disaggregation of remotely sensed land surface temperature: Literature survey, taxonomy, issues, and caveats. Remote Sensing of Environment, 131:119–139.
Zhang, Y. (1999). MODIS UCSB Emissivity Library. `https://icess.eri.ucsb.edu/modis/EMIS/html/em.html`. Acessed on November 22nd 2017.
Zhu, X., Chen, J., Gao, F., Chen, X., and Masek, J. G. (2010). An enhanced spatial and temporal adaptive reflectance fusion model for complex heterogeneous regions. Remote Sensing of Environment, 114:2610–2623.

Capítulo 4

Conclusão

Esta dissertação teve como objetivo a validação de métodos de estimativa da temperatura superficial da água de lagos e rios por sensoriamento remoto e a avaliação da performance de modelos de temperatura da água de rios calibrados com estes dados.

Como conclusões, responde-se às questões científicas propostas neste trabalho:

Qual é a acurácia, a precisão e os principais fatores influenciando nos erros das estimativas da temperatura superficial da água de lagos usando diferentes produtos de sensoriamento remoto?

Neste trabalho foi verificado que há diferenças no erro das estimativas da TSA entre lagos e rios. Para lagos, a acurácia do Landsat 7 ETM+ e do MODIS (produto continental) foram similares, com REQM próximo a 1°C, enquanto que em rios este valor fica próximo a 1,5°C para o Landsat. No caso dos lagos, os principais fatores são os efeitos de superfície, e na Lagoa Mangueira, por ser um lago raso, o efeito de pele fria, resultando numa subestimatação média da temperatura pela maioria dos estimadores. Para rios, o principal fator é a influência do entorno na radiância estimada pelo sensor. Mesmo retirando pixels de mistura solo-água, ainda há a reflexão da radiância emitida pelo solo e pela vegetação pela superfície do rio, o que resultou na superestimação média da temperatura pelos estimadores. Notou-se, também, a perda de performance dos sensores, em qualquer superfície, quando há alto valor de vapor d'água na atmosfera, sendo uma limitação dos métodos de correção atmosférica.

Para imagens Landsat, quais as diferenças entre os métodos utilizados para as estimativas da temperatura da água de lagos e rios?

Há bastante diferença entre os métodos que podem ser utilizados para o sensor Landsat 7 ETM+ na estimativa da temperatura de lagos, e que a aplicação da equação de transferência radiativa (RTE) se mostra a melhor opção. Também foi verificado que esta equação é bastante

sensível aos parâmetros de entrada, mas que os parâmetros de correção obtidos pelo AtmCorr são consistentes. Essa aplicação também mostrou os melhores resultados quando estimando a TSA do rio White, apesar da diferença entre a RTE e o algoritmo de canal-único foi bastante pequena.

Quais são os principais parâmetros que podem ser trabalhados para melhorar as estimativas da temperatura da água por sensoriamento remoto?

Os efeitos atmosféricos e a emissividade são os dois principais parâmetros que devem ser corrigidos para uma estimativa acurada da TSA, então valores mais acurados destes parâmetros produzem melhores resultados. Algoritmos para correção dos efeitos de superfície, que são amplamente aplicados em estudos de SST mas ainda pouco explorados em águas continentais, se mostram uma das ferramentas mais promissoras de melhorar estas estimativas. Além disso, na analise de sensibilidade, foi verificado que variações no valor da emissividade podem compensar parcialmente pelo efeito de pele fria, o que pode ser testado em estudos futuros. Por último, a técnica de *thermal sharpening* se mostrou uma ótima ferramenta para aumentar a resolução da banda termal do Landsat e em remover parcialmente os efeitos do entorno, e a aplicação destas técnicas é recomenda em qualquer estudo de sensoriamento remoto da TSA de rios, apesar de notadamente haver uma ausência destes algoritmos com foco em corpos hídricos.

Qual a acurácia e a precisão da técnica de downscaling SADFAT *na estimativa da temperatura da água de rios?*

A técnica mostrou um desempenho bastante aquém do observado na literatura para outros tipos de cobertura do solo, com REQM superior a 5°C. Os critérios de seleção desenvolvidos se mostraram fundamentais para a inclusão apenas dos dados mais acurados à série derivada do Landsat, apesar de ainda necessitar melhorias, o que também evidencia a ausência de técnicas como esta com foco em recursos hídricos.

É possível calibrar modelos de temperatura da água de rios utilizando apenas dados de temperatura da água derivados de sensoriamento remoto para se gerar séries consistentes de temperatura?

É possível se gerar séries contínuas e consistentes da temperatura de rios utilizando o modelo de temperatura da água *air2stream* calibrado com dados derivados de sensoriamento remoto, e sua aplicação está diretamente atrelada à acurácia da estimativa da TSA pelo sensor utilizado. A inclusão de mais dados não alterou significativamente a performance do modelo, apesar do erro dos dados derivados do MODIS serem consideravelmente superiores aos do Landsat. Portanto, em virtude deste baixo desempenho, o uso das imagens MODIS junto com as Landsat mostrou pouca resposta pelo modelo *air2stream*, apesar de indicar que mais dados podem melhorar a performance do modelo. Utilizando apenas os dados do Landsat na sua calibração, o modelo mostrou um boa performance, e esta técnica tem grande potencial para ser aplicada em estudos como tendências das séries temporais da temperatura de rios e na modelagem de rios tributários para aplicação em modelos ecológicos de lagos.

Referências

Allan, J. D. e Castillo, M. M. (2007). *Stream ecology: structure and function of running waters*. Springer Science & Business Media.

Allan, M. G., Hamilton, D. P., Trolle, D., Muraoka, K., e McBride, C. (2016). Spatial heterogeneity in geothermally-influenced lakes derived from atmospherically corrected Landsat thermal imagery and three-dimensional hydrodynamic modelling. *International Journal of Applied Earth Observation and Geoinformation*, 50:106–116.

Barnes, W. L., Pagano, T. S., e Salomonson, V. V. (1998). Prelaunch characteristics of the Moderate Resolution Imaging Spectroradiometer (MODIS) on EOS-AM1. *IEEE Transactions on Geoscience and Remote Sensing*, 36(4):1088–1100.

Barsi, J. A., Barker, J. L., e Schott, J. R. (2003a). An atmospheric correction parameter calculator for a single thermal band earth-sensing instrument. Em *Proceedings of the 2003 IEEE Geoscience and Remote Sensing Symposium (IGARSS'03)*, volume 5, pgs. 3014–3016.

Barsi, J. A., Schott, J., Palluconi, F. D., Helder, D. L., Hook, S. J., Markham, B. L., Chander, G., e O'Donnell, E. M. (2003b). Landsat TM and ETM+ thermal band calibration. *Canadian Journal of Remote Sensing*, 29(2):141–153.

Barsi, J. A., Schott, J., Palluconi, F. D., e Hook, S. J. (2005). Validation of a web-based atmospheric correction tool for single thermal band instruments. Em *Earth Observing Systems X*, volume 5882, pg. 58820E. International Society for Optics and Photonics.

Barton, I. J. (1995). Satellite-derived sea surface temperatures: Current status. *Journal of Geophysical Research: Oceans*, 100(C5):8777–8790.

Bohnenberger, J. E., Rodrigues, L. R., Motta-Marques, D. M., e Crossetti, L. O. (2018). Environmental dissimilarity over time in a large subtropical shallow lake is differently represented by phytoplankton functional approaches. *Marine and Freshwater Research*, 69(1):95–104.

Box, G. e Jenkins, G. M. (1976). *Time series analysis, forecasting and control*. Enders Robinson, Holden-Day Inc., San Francisco, California.

Boyd, M. e Kasper, B. (2003). *Analytical methods for dynamic open channel heat and mass transfer: Methodology for heat source model Version 7.0.* Portland, OR, Oregon Department of Environmental Quality, 193 p.

Cai, H., Piccolroaz, S., Huang, J., Liu, Z., Liu, F., e Toffolon, M. (2018). Quantifying the impact of the Three Gorges Dam on the thermal dynamics of the Yangtze River. *Environmental Research Letters*, 13(5):054016.

Caissie, D. (2006). The thermal regime of rivers: a review. *Freshwater Biology*, 51(8):1389–1406.

Caissie, D., El-Jabi, N., e Satish, M. G. (2001). Modelling of maximum daily water temperatures in a small stream using air temperature. *Journal of Hydrology*, 251(1–2):14–28.

Caissie, D., El-Jabi, N., e St-Hilaire, A. (1998). Stochastic modelling of water temperatures in a small stream using air to water relations. *Canadian Journal of Civil Engineering*, 25(2):250–260.

Caissie, D., Satish, M. G., e El-Jabi, N. (2005). Predicting river water temperatures using the equilibrium temperature concept with application on Miramichi River catchments (New Brunswick, Canada). *Hydrological Processes*, 19(11):2137–2159.

Cavalcanti, J. R., da Motta-Marques, D. M. L., e Fragoso Jr, C. R. (2016). Process-based modeling of shallow lake metabolism: Spatio-temporal variability and relative importance of individual processes. *Ecological Modelling*, 323:28–40.

Chavula, G., Brezonik, P., Thenkabail, P., Johnson, T., e Bauer, M. (2009). Estimating the surface temperature of lake malawi using AVHRR and MODIS satellite imagery. *Physics and Chemistry of the Earth, Parts A/B/C*, 34(13-16):749–754.

Cherkauer, K. A., Burges, S. J., Handcock, R. N., Kay, J. E., Kampf, S. K., e Gillespie, A. R. (2005). Assessing satellite-based and aircraft-based thermal infrared remote sensing for monitoring Pacific Northwest river temperature. *Journal of the American Water Resources Association*, 41(5):1149–1159.

Cluis, D. A. (1972). Relationship between stream water temperature and ambient air temperature – a simple autoregressive model for mean daily stream water temperature fluctuations. *Nordic Hydrology*, 3:65–71.

Coll, C., Caselles, V., Valor, E., e Niclòs, R. (2012). Comparison between different sources of atmospheric profiles for land surface temperature retrieval from single channel thermal infrared data. *Remote Sensing of Environment*, 117:199–210.

Crisp, D. T. e Howson, G. (1982). Effect of air temperature upon mean water temperature in streams in the north Pennines and English Lake District. *Freshwater Biology*, 12(4):359–367.

Cristea, N. C. e Burges, S. J. (2009). Use of thermal infrared imagery to complement monitoring and modeling of spatial stream temperatures. *Journal of Hydrologic Engineering*, 14(10):1080–1090.

Cristóbal, J., Jiménez-Muñoz, J. C., Sobrino, J. A., Ninyerola, M., e Pons, X. (2009). Improvements in land surface temperature retrieval from the Landsat series thermal band using water vapor and air temperature. *Journal of Geophysical Research*, 114:D08103.

Crosman, E. T. e Horel, J. D. (2009). MODIS-derived surface temperature of the Great Salt Lake. *Remote Sensing of Environment*, 113(1):73–81.

Despini, F. e Teggi, S. (2013). Analysis of temperature maps of waterbodies obtained from ASTER TIR images. *International Journal of Remote Sensing*, 34(9–10):3636–3653.

Dugdale, S. J. (2016). A practitioner's guide to thermal infrared remote sensing of rivers and streams: recent advances, precautions and considerations. *Wiley Interdisciplinary Reviews: Water*, 3(2):251–268.

Dugdale, S. J., Hannah, D. M., e Malcolm, I. A. (2017). River temperature modelling: A review of process-based approaches and future directions. *Earth-Science Reviews*, 175:97–113.

Dugdale, S. J., Malcolm, I. A., Kantola, K., e Hannah, D. M. (2018). Stream temperature under contrasting riparian forest cover: Understanding thermal dynamics and heat exchange processes. *Science of the Total Environment*, 610–611:1375–1389.

Edinger, J. E., Duttweiler, D. W., e Geyer, J. C. (1968). The response of water temperatures to meteorological condition. *Water Resources Research*, 4(5):1137–1143.

Emelyanova, I. V., McVicar, T. R., Van Niel, T. G., Li, L. T., e van Dijk, A. I. (2013). Assessing the accuracy of blending Landsat–MODIS surface reflectances in two landscapes with contrasting spatial and temporal dynamics: A framework for algorithm selection. *Remote Sensing of Environment*, 133:193–209.

Fairall, C., Bradley, E. F., Godfrey, J., Wick, G., Edson, J. B., e Young, G. (1996). Cool-skin and warm-layer effects on sea surface temperature. *Journal of Geophysical Research: Oceans*, 101(C1):1295–1308.

Fenocchi, A., Rogora, M., Sibilla, S., e Dresti, C. (2017). Relevance of inflows on the thermodynamic structure and on the modeling of a deep subalpine lake (Lake Maggiore, Northern Italy/Southern Switzerland). *Limnologica*, 63:42–56.

Fragoso Jr, C. R., Marques, D. M. M., Ferreira, T. F., Janse, J. H., e van Nes, E. H. (2011). Potential effects of climate change and eutrophication on a large subtropical shallow lake. *Environmental Modelling & Software*, 26(11):1337–1348.

Fragoso Jr, C. R., van Nes, E. H., Janse, J. H., e Motta-Marques, D. M. L. (2009). IPH-TRIM3D-PCLake: A three-dimensional complex dynamic model for subtropical aquatic ecosystems. *Environmental Modelling & Software*, 24(11):1347–1348.

Fricke, K. e Baschek, B. (2013). Water surface temperature profiles for the Rhine river derived from Landsat ETM+ data. Em *Proceedings of SPIE 8887, Remote Sensing for Agriculture, Ecosystems, and Hydrology XV*, pg. 88870E.

Fricke, K. e Baschek, B. (2015). Temperature monitoring along the Rhine river based on airborne thermal infrared remote sensing: estimation of in situ water temperatures and inflow detection compared to artificial satellite data. *Journal of Applied Remote Sensing*, 9(1):095067.

Friedman, D. (1969). Infrared characteristics of ocean water (1.5–15 μ). *Applied Optics*, 8(10):2073–2078.

Gao, F., Masek, J., Schwaller, M., e Hall, F. (2006). On the blending of the Landsat and MODIS surface reflectance: predicting daily Landsat surface reflectance. *IEEE Transactions on Geoscience*, 44(8):2207–2218.

Garner, G., Malcolm, I. A., Sadler, J. P., e Hannah, D. M. (2017). The role of riparian vegetation density, channel orientation and water velocity in determining river temperature dynamics. *Journal of Hydrology*, 553:471–485.

Gray, D. K., Hampton, S. E., O'Reilly, C. M., Sharma, S., e Cohen, R. S. (2018). How do data collection and processing methods impact the accuracy of long-term trend estimation in lake surface-water temperatures? *Limnology and Oceanography: Methods*, 16(8):504–515.

Gu, R., Montgomery, S., e Austin, R. A. (1998). Quantifying the effects of stream discharge on summer river temperature. *Hydrological Sciences Journal*, 43(6):885–904.

Handcock, R., Gillespie, A., Cherkauer, K., Kay, J., Burges, S., e Kampf, S. (2006). Accuracy and uncertainty of thermal-infrared remote sensing of stream temperatures at multiple spatial scales. *Remote Sensing of Environment*, 100(4):427–440.

Handcock, R. N., Torgersen, C. E., Cherkauer, K. A., Gillespie, A. R., Tockner, K., Faux, R. N., e Tan, J. (2012). Thermal infrared remote sensing of water temperature in riverine landscapes. *Fluvial Remote Sensing for Science and Management*, 12:85–113.

Hilker, T., Wulder, M. A., Coops, N. C., Linke, J., McDermid, G., Masek, J. G., Gao, F., e White, J. C. (2009). A new data fusion model for high spatial- and temporal-resolution mapping of forest disturbance based on Landsat and MODIS. *Remote Sensing of Environment*, 113(8):1613–1627.

Hulley, G. C., Hook, S. J., e Schneider, P. (2011). Optimized split-window coefficients for deriving surface temperatures from inland water bodies. *Remote Sensing of Environment*, 115(12):3758–3769.

Jensen, J. R. (2009). *Remote sensing of the environment: An earth resource perspective*. Pearson Education, 2ª edição.

Jiménez-Muñoz, J. e Sobrino, J. (2006). Error sources on the land surface temperature retrieved from thermal infrared single channel remote sensing data. *International Journal of Remote Sensing*, 27(05):999–1014.

Jiménez-Muñoz, J. C., Cristobal, J., Sobrino, J. A., Soria, G., Ninyerola, M., Pons, X., e Pons, X. (2009). Revision of the single-channel algorithm for land surface temperature retrieval from Landsat thermal-infrared data. *IEEE Transactions on Geoscience and Remote Sensing*, 47(1):339–349.

Jiménez-Muñoz, J. C. e Sobrino, J. A. (2003). A generalized single-channel method for retrieving land surface temperature from remote sensing data. *Journal of Geophysical Research*, 108:D22.

Jiménez-Muñoz, J. C., Sobrino, J. A., Mattar, C., e Franch, B. (2010). Atmospheric correction of optical imagery from MODIS and Reanalysis atmospheric products. *Remote Sensing of Environment*, 114(10):2195–2210.

Kay, J. E., Kampf, S. K., Handcock, R. N., Cherkauer, K. A., Gillespie, A. R., e Burges, S. J. (2005). Accuracy of lake and stream temperatures estimated from thermal infrared images. *JAWRA Journal of the American Water Resources Association*, 41(5):1161–1175.

Kilpatrick, K., Podestá, G., Walsh, S., Williams, E., Halliwell, V., Szczodrak, M., Brown, O., Minnett, P., e Evans, R. (2015). A decade of sea surface temperature from MODIS. *Remote Sensing of Environment*, 165:27–41.

Kothandaraman, V. (1971). Analysis of water temperature variations in large rivers. *Journal of the Sanitary Engineering Division*, 97:19–31.

Lamaro, A. A., Mariñelarena, A., Torrusio, S. E., e Sala, S. E. (2013). Water surface temperature estimation from Landsat 7 ETM+ thermal infrared data using the generalized single-channel method: Case study of Embalse del Río Tercero (Córdoba, Argentina). *Advances in Space Research*, 51(3):492–500.

Li, Y., Zhang, Q., Zhang, L., Tan, Z., e Yao, J. (2017). Investigation of water temperature variations and sensitivities in a large floodplain lake system (Poyang Lake, China) using a hydrodynamic model. *Remote Sensing*, 9(12):1231.

Li, Z.-L., Tang, B.-H., Wu, H., Ren, H., Yan, G., Wan, Z., Trigo, I. F., e Sobrino, J. A. (2013). Satellite-derived land surface temperature: Current status and perspectives. *Remote Sensing of Environment*, 131:14–37.

Liu, G., Ou, W., Zhang, Y., Wu, T., Zhu, G., Shi, K., e Qin, B. (2015). Validating and mapping surface water temperatures in Lake Taihu: Results from MODIS land surface temperature products. *IEEE Journal of Selected Topics in Applied Earth Observations and Remote Sensing*, 8(3):1230–1244.

Mao, K., Qin, Z., Shi, J., e Gong, P. (2005). A practical split-window algorithm for retrieving land-surface temperature from MODIS data. *International Journal of Remote Sensing*, 26(15):3181–3204.

Marruedo Arricibita, A. I., Dugdale, S. J., Krause, S., Hannah, D. M., e Lewandowski, J. (2018). Thermal infrared imaging for the detection of relatively warm lacustrine groundwater discharge at the surface of freshwater bodies. *Journal of Hydrology*, 562:281–289.

Masuda, K., Takashima, T., e Takayama, Y. (1988). Emissivity of pure and sea waters for the model sea surface in the infrared window regions. *Remote Sensing of Environment*, 24(2):313–329.

Matulla, C., Tordai, J., Schlögl, M., Ganekind, M., Matulla, H., Ressl, H., e Chimani, B. (2018). Establishment of a long-term lake-surface temperature dataset within the European Alps extending back to 1880. *Climate Dynamics*, pgs. 1–17.

Mohseni, O., Stefan, H., e Erickson, T. R. (1998). A nonlinear regression model for weekly stream temperatures. *Water Resources Research*, 34(10):2685–2692.

Mohseni, O. e Stefan, H. G. (1999). Stream temperature/air temperature relationship: a physical interpretation. *Journal of Hydrology*, 218(3–4):128–141.

Mosley, M. P. (1982). New Zealand river temperature regimes. *Water and Soil Miscellaneous Publications No. 36., Wellington, New Zealand*, pg. 87 pp.

Mukherjee, S., Joshi, P., e Garg, R. (2014). A comparison of different regression models for downscaling Landsat and MODIS land surface temperature images over heterogeneous landscape. *Advances in Space Research*, 54(4):655–669.

Munar, A. M. (2017). *Pareamento Bacia-Lagoa usando modelagem hidrológica-hidrodinâmica e sensoriamento remoto*. PhD Thesis, Postgraduate Program in Water Resources and Environmental Sanitation, Federal University of Rio Grande do Sul, 139 p.

Munar, A. M., Cavalcanti, J. R., Bravo, J. M., Fan, F. M., Motta-Marques, D. M. L., e Fragoso Jr, C. R. (2018). Coupling large-scale hydrological and hydrodynamic modeling: Toward a better comprehension of watershed-shallow lake processes. *Journal of Hydrology*, 564:424–441.

Oesch, D. C., Jaquet, J.-M., Hauser, A., e Wunderle, S. (2005). Lake surface water temperature retrieval using advanced very high resolution radiometer and Moderate Resolution Imaging Spectroradiometer data: Validation and feasibility study. *Journal of Geophysical Research: Oceans*, 110(C12).

Okwen, R., Pu, R., e Cunningham, J. (2011). Remote sensing of temperature variations around major power plants as point sources of heat. *International Journal of Remote Sensing*, 32(13):3791–3805.

O'Reilly, C. M., Sharma, S., Gray, D. K., Hampton, S. E., Read, J. S., Rowley, R. J., Schneider, P., Lenters, J. D., McIntyre, P. B., Kraemer, B. M., et al. (2015). Rapid and highly variable warming of lake surface waters around the globe. *Geophysical Research Letters*, 42(24):10–773.

Orr, H. G., Johnson, M. F., Wilby, R. L., Hatton-Ellis, T., e Broadmeadow, S. (2015). What else do managers need to know about warming rivers? A United Kingdom perspective. *Wiley Interdisciplinary Reviews: Water*, 2(2):55–64.

Ottlé, C. e Stoll, M. (1993). Effect of atmospheric absorption and surface emissivity on the determination of land surface temperature from infrared satellite data. *International Journal of Remote Sensing*, 14(10):2025–2037.

Pahlevan, N., Gerace, A. D., e Schott, J. R. (2011). Using thermal remote sensing as a tool for calibrating a hydrodynamic model in inland waters. Em *Proceedings of SPIE 8030, Ocean Sensing and Monitoring III, 80300I.*

Paiva, R. C. D., Buarque, D. C., Collischonn, W., Bonnet, M.-P., Frappart, F., Calmant, S., e Mendes, C. A. B. (2013). Large-scale hydrologic and hydrodynamic modeling of the Amazon River basin. *Water Resources Research*, 49(3):1226–1243.

Pareeth, S., Salmaso, N., Adrian, R., e Neteler, M. (2016). Homogenised daily lake surface water temperature data generated from multiple satellite sensors: A long-term case study of a large sub-alpine lake. *Scientific reports*, 6:31251.

Perry, E. M. e Moran, M. S. (1994). An evaluation of atmospheric corrections of radiometric surface temperatures for a semiarid rangeland watershed. *Water resources research*, 30(5):1261–1269.

Piccolroaz, S., Calamita, E., Majone, B., Gallice, A., Siviglia, A., e Toffolon, M. (2016). Prediction of river water temperature: a comparison between a new family of hybrid models and statistical approaches. *Hydrological Processes*, 30(21):3901–3917.

Piccolroaz, S., Healey, N., Lenters, J., Schladow, S., Hook, S., Sahoo, G., e Toffolon, M. (2018). On the predictability of lake surface temperature using air temperature in a changing climate: A case study for Lake Tahoe (USA). *Limnology and Oceanography*, 63(1):243–261.

Piccolroaz, S., Toffolon, M., e Majone, B. (2013). A simple lumped model to convert air temperature into surface water temperature in lakes. *Hydrology and Earth System Sciences*, 17:3323–3338.

Piotrowski, A. P. e Napiorkowski, J. J. (2018). Performance of the air2stream model that relates air and stream water temperatures depends on the calibration method. *Journal of Hydrology*, 561:395–412.

Poole, G. C. e Berman, C. H. (2001). An ecological perspective on in-stream temperature: Natural heat dynamics and mechanisms of human-caused thermal degradation. *Environmental Management*, 27(6):787–802.

Prats, J., Reynaud, N., Rebière, D., Peroux, T., Tormos, T., e Danis, P.-A. (2018). LakeSST: Lake Skin Surface Temperature in French inland water bodies for 1999–2016 from Landsat archives. *Earth System Science Data*, 10(2):727–743.

Price, J. C. (1984). Land surface temperature measurements from the split window channels of the NOAA 7 Advanced Very High Resolution Radiometer. *Journal of Geophysical Research: Atmospheres*, 89(D5):7231–7237.

Purkis, S. J. e Klemas, V. V. (2011). *Remote sensing and global environmental change*. John Wiley & Sons.

Qin, Z., Karnieli, A., e Berliner, P. (2001). A mono-window algorithm for retrieving land surface temperature from Landsat TM data and its application to the Israel-Egypt border region. *International Journal of Remote Sensing*, 22(18):3719–3746.

Reinart, A. e Reinhold, M. (2008). Mapping surface temperature in large lakes with MODIS data. *Remote Sensing of Environment*, 112:603–611.

Reynolds, R. W., Smith, T. M., Liu, C., Chelton, D. B., Casey, K. S., e Schlax, M. G. (2007). Daily high-resolution-blended analyses for sea surface temperature. *Journal of Climate*, 20(22):5473–5496.

Robinson, I., Wells, N., e Charnock, H. (1984). The sea surface thermal boundary layer and its relevance to the measurement of sea surface temperature by airborne and spaceborne radiometers. *International Journal of Remote Sensing*, 5(1):19–45.

Schluessel, P., Emery, W. J., Grassl, H., e Mammen, T. (1990). On the bulk-skin temperature difference and its impact on satellite remote sensing of sea surface temperature. *Journal of Geophysical Research: Oceans*, 95(C8):13341–13356.

Schneider, K. e Mauser, W. (1996). Processing and accuracy of Landsat Thematic Mapper data for lake surface temperature measurement. *International Journal of Remote Sensing*, 17(11):2027–2041.

Schneider, P. e Hook, S. J. (2010). Space observations of inland water bodies show rapid surface warming since 1985. *Geophysical Research Letters*, 37(22).

Schott, J. R. (2007). *Remote sensing: the image chain approach*. Oxford University Press; 2nd edition.

Schott, J. R., Barsi, J. A., Nordgren, B. L., Raqueno, N. G., e De Alwis, D. (2001). Calibration of Landsat thermal data and application to water resource studies. *Remote Sensing of Environment*, 78(1-2):108–117.

Sharma, S., Blagrave, K., Magnuson, J. J., O'Reilly, C. M., Oliver, S., Batt, R. D., Magee, M. R., Straile, D., Weyhenmeyer, G. A., Winslow, L., et al. (2019). Widespread loss of lake ice around the Northern Hemisphere in a warming world. *Nature Climate Change*, pg. 1.

Sima, S., Ahmadalipour, A., e Tajrishy, M. (2013). Mapping surface temperature in a hyper-saline lake and investigating the effect of temperature distribution on the lake evaporation. *Remote Sensing of Environment*, 136:374–385.

Simon, R., Tormos, T., e Danis, P.-A. (2014). Retrieving water surface temperature from archive LANDSAT thermal infrared data: Application of the mono-channel atmospheric correction algorithm over two freshwater reservoirs. *International Journal of Applied Earth Observation and Geoinformation*, 30:247–250.

Sinokrot, B. A. e Stefan, H. G. (1993). Stream temperature dynamics: measurements and modeling. *Water Resources Research*, 29(7):2299–2312.

Snyder, W. C., Wan, Z., Zhang, Y., e Feng, Y.-Z. (1998). Classification-based emissivity for land surface temperature measurement from space. *International Journal of Remote Sensing*, 19(14):2753–2774.

Sobrino, J. A., Jiménez-Muñoz, J. C., e Paolini, L. (2004). Land surface temperature retrieval from Landsat TM 5. *Remote Sensing of Environment*, 90(4):434–440.

Sobrino, J. A., Jiménez-Muñoz, J. C., Soria, G., Romaguera, M., Guanter, L., Moreno, J., Plaza, A., e Martinez, P. (2008). Land surface emissivity retrieval from different VNIR and TIR sensors. *IEEE Transactions on Geoscience and Remote Sensing*, 46(2):316–327.

Stefan, H. G. e Preud'homme, E. B. (1993). Stream temperature estimation from air temperature. *Journal of the American Water Resources Association*, 29(1):27–45.

Sullivan, K. e Adams, T. N. (1991). *The physics of stream heating: 2) An analysis of temperature patterns in stream environments based on physical principles and field data.* Weyerhaeuser Company Technical Report 044-5002/89/2.

Swain, R. e Sahoo, B. (2017). Mapping of heavy metal pollution in river water at daily time-scale using spatio-temporal fusion of MODIS-Aqua and Landsat satellite imageries. *Journal of Environmental Management*, 192:1–14.

Toffolon, M. e Piccolroaz, S. (2015). A hybrid model for river water temperature as a function of air temperature and discharge. *Environmental Research Letters*, 10:114011.

Torgersen, C. E., Faux, R. N., McIntosh, B. A., Poage, N. J., e Norton, D. J. (2001). Airborne thermal remote sensing for water temperature assessment in rivers and streams. *Remote Sensing of Environment*, 76(3):386–398.

van Vliet, M. T. H., Franssen, W. H. P., Yearsley, J. R., Ludwig, F., Haddeland, I., Lettenmaier, D. P., e Kabat, P. (2013). Global river discharge and water temperature under climate change. *Global Environmental Change*, 23(2):450–464.

Vatland, S. J., Gresswell, R. E., e Poole, G. C. (2015). Quantifying stream thermal regimes at multiple scales: Combining thermal infrared imagery and stationary stream temperature data in a novel modeling framework. *Water Resources Research*, 51:31–46.

Vinnå, L. R., Wüest, A., Zappa, M., Fink, G., e Bouffard, D. (2017). Tributaries affect the thermal response of lakes to climate change. *Hydrology and Earth System Sciences*, 22(1):31.

Wald, L. (2002). *Data fusion: definitions and architectures: fusion of images of different spatial resolutions.* Presses de l'Ecole, Ecole des Mines de Paris, Paris, France, 200 p.

Walton, C., Pichel, W., Sapper, J., e May, D. (1998). The development and operational application of nonlinear algorithms for the measurement of sea surface temperatures with the NOAA polar-orbiting environmental satellites. *Journal of Geophysical Research: Oceans*, 103(C12):27999–28012.

Wan, Z. e Dozier, J. (1996). A generalized split-window algorithm for retrieving land-surface temperature from space. *IEEE Transactions on Geoscience and Remote Sensing*, 34(4):892–905.

Ward, J. V. (1985). Thermal characteristics of running waters. Em *Perspectives in Southern Hemisphere Limnology*, pgs. 31–46. Developments in Hydrobiology 28.

Wawrzyniak, V., Piégay, H., Allemand, P., Vaudor, L., e Grandjean, P. (2013). Prediction of water temperature heterogeneity of braided rivers using very high resolution thermal infrared (TIR) images. *International Journal of Remote Sensing*, 34(13):4812–4831.

Wawrzyniak, V., Piégay, H., e Poirel, A. (2012). Longitudinal and temporal thermal patterns of the French Rhône River using Landsat ETM+ thermal infrared images. *Aquatic sciences*, 74(3):405–414.

Webb, B. W., Hannah, D. M., Moore, R. D., Brown, L. E., e Nobilis, F. (2008). Recent advances in stream and river temperature research. *Hydrological Processes*, 22:902–918.

Weng, Q., Fu, P., e Gao, F. (2014). Generating daily land surface temperature at Landsat resolution by fusing Landsat and MODIS data. *Remote Sensing of Environment*, 145:55–67.

Wenyao, L., Field, R., Gantt, R., e Klemas, V. (1987). Measurement of the surface emissivity of turbid waters. *Chinese Journal of Oceanology and Limnology*, 5(4):363–369.

Wloczyk, C., Richter, R., Borg, E., e Neubert, W. (2006). Sea and lake surface temperature retrieval from landsat thermal data in Northern Germany. *International Journal of Remote Sensing*, 27(12):2489–2502.

Woodward, G., Bonada, N., Brown, L. E., Death, R. G., Durance, I., Gray, C., Hladyz, S., Ledger, M. E., Milner, A. M., Ormerod, S. J., et al. (2016). The effects of climatic fluctuations and extreme events on running water ecosystems. *Philosophical Transactions of the Royal Society B: Biological Sciences*.

Woolway, R. I. e Merchant, C. J. (2018). Intralake heterogeneity of thermal responses to climate change: A study of large Northern Hemisphere lakes. *Journal of Geophysical Research: Atmospheres*, 123(6):3087–3098.

Yang, K., Yu, Z., Luo, Y., Yang, Y., Zhao, L., e Zhou, X. (2018). Spatial and temporal variations in the relationship between lake water surface temperatures and water quality–a case study of Dianchi Lake. *Science of the Total Environment*, 624:859–871.

Zhang, Q., Ye, X.-c., Werner, A. D., Li, Y.-l., Yao, J., Li, X.-h., e Xu, C.-y. (2014). An investigation of enhanced recessions in Poyang Lake: comparison of Yangtze River and local catchment impacts. *Journal of Hydrology*, 517:425–434.

Zhang, Y. (1999). MODIS UCSB Emissivity Library. https://icess.eri.ucsb.edu/modis/EMIS/html/em.html. Acessed on November 22nd 2017.

Zhu, X., Chen, J., Gao, F., Chen, X., e Masek, J. G. (2010). An enhanced spatial and temporal adaptive reflectance fusion model for complex heterogeneous regions. *Remote Sensing of Environment*, 114:2610–2623.

Zurita-Milla, R., Clevers, J. G. P. W., e Schaepman, M. E. (2008). Unmixing-based Landsat TM and MERIS FR data fusion. *IEEE Geoscience and Remote Sensing Letters*, 5(3):453–457.